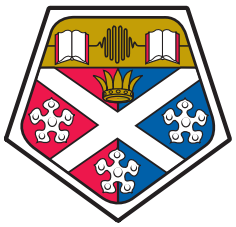

University of Strathclyde
Science

Raman amplification of ultra-short laser pulses in plasma

by Xue Yang

Department of Physics
University of Strathclyde

Supervisor: Prof. D. A. Jaroszynski

Thesis submitted in fulfilment for the degree of Doctor of Philosophy

October 2013

Abstract

This thesis presents the experimental investigation of Raman amplification of ultrashort laser pulses by a counter propagating chirped pump pulse through resonant excitation of a plasma density wave. Since plasma is a gain medium able to withstand very high intensities, this scheme is proposed as the basis of a new generation of laser amplifiers capable of replacing Chirped Pulse Amplification (CPA) systems, which are limited by the damage threshold of solid state gain media.

In this experiment, both the pump and the probe beams are generated from a 30 TW Ti:Sapphire CPA laser system. The chirped pump pulse is 250 ps long and centered at 805 nm. The probe pulse, compressed to minimum 70 fs and then frequency downshifted before the interaction with the pump pulse in the plasma, contains maximum 1 mJ of energy on target. The plasma is generated by striking a high voltage discharge across a hydrogen gas filled capillary waveguide with the electron plasma density controlled around $1 \times 10^{18}\,\mathrm{cm}^{-3}$. In addition to a CCD camera and a spectrometer, a self-built Frequency-Resolved Optical Gating (FROG) system is employed as a real time detector to fully reconstruct the probe pulse amplitude and phase.

The experiment is performed in two stages, firstly with low pump energies, about 400 mJ, allowing the verification of chirped pulse Raman amplification mechanisms in the linear regime. In these conditions the energy gain grows exponentially with the pump energy and increases with backing pressure. The theoretical predictions showing that the probe pulse duration should be preserved when using a chirped pump pulse are confirmed. Maximum energy gain is 450%. The second stage is implemented with pump energies up to 950 mJ. Initially the Raman process develops in the linear regime. With the amplification of the probe pulse, the amplification mechanism can transit to a nonlinear process. The highest energy gain is 650%. Obvious bandwidth broadening mainly on the high frequency side and gain saturation with either increasing pump or probe energy are observed. Assisted by 1D aPIC simulations, the transition from the Raman linear regime to the nonlinear regime is analysed.

Acknowledgements

The last five years have been an amazing chapter of my life, for which I would like to thank my supervisor Prof. Dino Jaroszynski who gave me the opportunity to do my Ph.D at the University of Strathclyde and the chance to work on this challenging but interesting project. I learned a lot from him, not only about physics, but also about the efforts he made to let things happen and his dedicating and engaging attitude to work.

My sincerest thanks to my second supervisor Dr. Gregory Vieux for his valuable guidance and support through the whole project. It is from him that I gained most of my knowledge and experimental skills in laser-plasma interaction. My deepest gratitude goes to Dr. Enrico Brunetti, for his support on part of the experiment. As my life consultant he helped me in every aspect of my life starting from the time I did my fourth year project at Strathcldye.

I am grateful to Dr. Bernard Ersfeld and Dr. John Farmer for their theoretical support in the field of Raman amplification, as well as Dr. Garav Raj and Prof. Min Sup Hur who helped with performing aPIC simulations. The help of Dr. Riju Issac and Dr. Gregor Welsh is also greatly appreciated for their maintenance of the laser system and their advice throughout this experiment. Many thanks to Dr. Mark Wiggins who micro-machined the capillary which is the essential component of the experiment. I would like to give my special thanks to Mr David Clark for all his design and precise manufacturing of experimental components. My thanks extends to every member of our group. In particular, all the PhD students in our group for their company.

I would like to acknowledge the financial supports from the University of Strathclyde and ORSAS.

Finally, I would like to thank my family for their support.

Role of the author

The experiments presented in this thesis were performed by the author with the help of Dr. Gregory Vieux. The white light generator and the FROG were set up and tested by the author with the help of Dr. Enrico Brunetti. The capillary used in the experiment was constructed by Dr. Mark Wiggins, and the capillary housing was from Mr. David Clark. The data processing programs were done with the help of Dr. Enrico Brunetti. 1-D analytical theory of chirping effects on Raman amplification of laser pulses in plasma was developed by Dr. Bernhard Ersfeld. Data processing and analysis were done by the author with the supervision of Dr. Gregory Vieux. The numerical simulations presented in the thesis were performed by Dr. Gregory Vieux and Dr. Gaurav Raj. The aPIC codes used to simulate the experiment were originally from Prof. Min Sup Hur.

Contents

List of Figures

List of Tables

Chapter 1

Introduction

1.1 The development of the laser

Lasers (Light Amplification by Stimulated Emission of Radiation) are sources of very intense, highly coherent electromagnetic radiation with narrow spectrum bandwidth and high directionality. These advantages make lasers ideal tools for a wide range of applications such as nonlinear optics, communications, data storage, high-precision metrology, high-resolution spectroscopy, manipulation of atoms and molecules as well as industrial and medical applications. There is no doubt that lasers are one of the greatest inventions of the last century.

The theoretical foundations of lasers was established in 1917 by Albert Einstein, who proposed that photons could stimulate the emission of identical photons from excited atoms [1]. Rudolf Ladenburg reported indirect evidence of stimulated emission in 1928 [2]. However, physicists of the time considered it of little practical importance, because according to the Boltzmann population distribution, for a system at thermal equilibrium higher energy states must be less populated than lower levels. Since the reverse processes of absorption and stimulated emission proceed at rates proportional to the population number of atoms in the lower and upper states, population inversion must be achieved in order to get net stimulated emission during photons passing

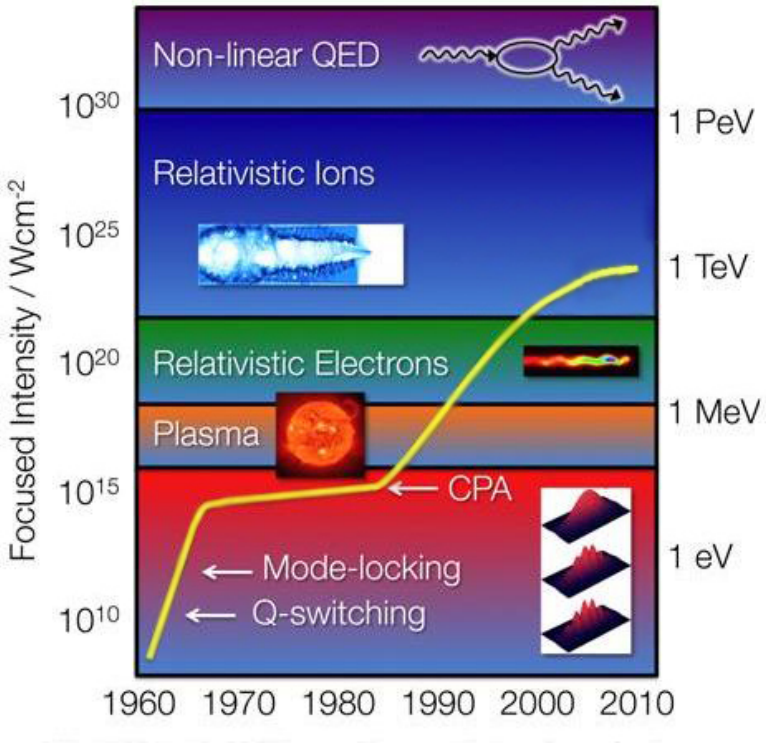

Figure 1.1: Route map of maximum focused laser intensity and the associated physical regimes that become accessible. Image is from `http://www.engin.umich.edu/research/cuos/ResearchGroups/HFS/what_is_hfs.html`.

through the medium. Therefore, to develop a proper laser, two questions needed to be answered: how to excite a population inversion and what to use as an active medium.

The first working laser was realised in 1960 by Theodore Maiman [3] who chose ruby as the gain medium and used optical pumping to raise the chromium atoms in ruby to the excited laser level. The development of the first functioning laser inspired other researchers and several new types of lasers were demonstrated in the early 1960s, such as the helium-neon gas laser, the neodymium-doped solid state laser and the gallium arsenide diode laser, etc.

In the following years several new technologies which are of great importance to the quick growth of the laser peak power were developed. As shown in Fig. 1.1, the invention of Q-switching [4] and mode-locking [5, 6, 7] enabled the increase of the power density by concentrating the energy into ever shorter pulses.

Q-switching allows the production of pulsed laser beams by putting a variable attenuator in an optical resonator in order to increase the laser peak intensity. The attenuator can act actively by using shutters, rotating mirrors, acousto-optic modulators, electro-optic modulators or passively by means of saturable absorbers. It works by stopping lasing until enough energy is accumulated in the gain medium and can reduce the pulse duration to nanoseconds with energies typically higher than the saturation energy of the gain medium.

Mode-locking is a technique that made it possible for lasers to operate at extremely short duration, on the order of femtoseconds. It consists of the application of a periodic amplitude modulation to the excited resonator modes to induce a fixed phase relationship between them. This leads to constructive interference between these modes and therefore to very short and intense laser pulses. Mode-locking can be realised by adding external signals from acousto-optic or electro-optic modulators (active mode-locking) or by using saturable absorbing elements (passive mode-locking). The passive mode-locking can either be achieved by using semiconductor saturable absorber mirrors (SESAM) or an artificial saturable absorber, such as Kerr lens mode locking

(KLM). For KLM there are two mechanisms, (a) hard aperture KLM, in which the Kerr lens effect in gain medium reduces optical loss on aperture and (b) soft aperture KLM, in which the Kerr lens leads to better overlap of laser with pump lasers. Moreover, combining SESAM and KLM, mode-locking can occur spontaneously (i.e. self-mode-locking) [7]. In self-mode-locking, the resonator is aligned only for the intense part of the beam that experience Kerr lensing effect in the gain medium, while the low intensity beam will propagate in a detuned resonator and get attenuated. The mode-locking technique has enabled the generation of the shortest pulses with durations down to $\approx$ 5 fs in Ti:sapphire lasers.

The invention of these two techniques pushed the laser peak powers to GW range and allowed the investigation of some basic nonlinear optical effects such as nonlinear ionisation processes, harmonics generation, nonlinear Raman and Brillouin scattering, 4-wave mixing, self-focusing etc.

Compared with Q-switching, mode-locking produces much higher pulse repetition rates, much lower pulse energies and much shorter pulse durations. These characteristics determine how the two techniques are applied in the different stages of a laser chain. Q-switching is mainly employed in main amplifiers to increase the pulse energy while mode-locking is used in short pulse oscillators to produce low energy seed pulses for further amplification.

From the late 1960s and for almost 20 years, the laser peak power was limited to GW-level, due to the risk of damaging the gain media and optical elements. A breakthrough came in the mid-1980s with the invention of Chirped Pulse Amplification (CPA), a technique that promoted the development of ultra-intense femtosecond lasers and pushed the peak power up to the PW-level [8].

The CPA technique generates short duration, high intensity laser pulses by stretching, amplification and recompression of short duration, low intensity laser pulses. Between stretching and recompression, the laser pulse, with a time dependent instantaneous frequency, is known as a chirped laser pulse. The schematic diagram of CPA

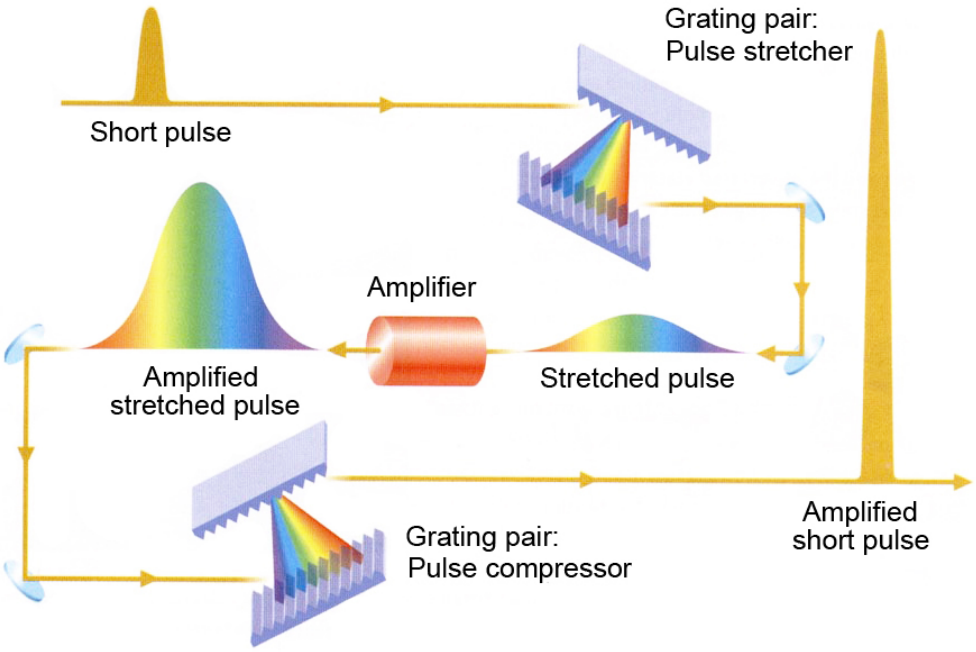

Figure 1.2: Schematic of chirped pulse amplification laser system. Image is from `http://www.engin.umich.edu/research/cuos/ResearchGroups/HFS/ExperimentalfacilitiesChirped_Pulse_Amp.html`.

laser systems is shown in Fig. 1.2.

Femtosecond pulses from an oscillator are stretched to several hundreds of picoseconds to reduce the intensity in the main amplification chain to prevent damage to the optical components. After amplification, pulses are recompressed obtaining short durations and high power levels. The stretching and recompression are realised with a dispersive system like a pair of gratings or prisms. The first dispersive element provides a frequency-dependent angular dispersion of an incident beam in order to create different optical path lengths for different wavelengths. The second element compensates this angular dispersion so that different wavelength components of the pulse recombine with a phase shift.

Ti:sapphire lasers are the most widely used solid-state lasers nowadays, replacing ultrafast dye lasers thanks to the properties of their amplifying medium. Ti:sapphire crystals have a broad gain bandwidth from 660 nm to 1180 nm and are therefore able to sustain short pulse durations. The pump absorption frequency of Ti:sapphire crystals peaks at 490 nm and with a range from 400 nm to 630 nm. Therefore, frequency

doubled Nd:YAG, Nd:YLF or Nd:YVO_4 lasers at 532 nm are usually used to pump Ti:sapphire crystals.

By coupling Ti:sapphire oscillators and amplifiers with the CPA technique, multi TW tabletop laser systems are widely available in university scale laboratories and have become the fundamental tool for the study of ultrafast physics. The experiment described in this thesis has been carried out with such a laser system at the Terahertz to Optical Pulse Source (TOPS) laboratory at the University of Strathclyde [9].

Furthermore, laser peak powers up to the PW-level were firstly achieved in 1996. Currently several laser facilities around the world have PW lasers, such as Vulcan laser at RAL, Titan laser at LLNL, Texas Petawatt at the University of Texas, HERCULES at the University of Michigan, etc.

The development of TW and PW lasers has paved the way to numerous new applications like laser wakefield acceleration [10], high harmonic generation [11], compact X-ray lasers [12], compact terahertz sources [13, 14], fast inertial fusion [15], etc.

1.2 History of plasma based Raman amplifier

High-power ultra-short pulse lasers have become valuable tools for scientists, and interesting physics is bound to emerge with the increase of the laser intensity. However, at the current stage of development, as shown in Fig. 1.1, the growth is slowing down. The main obstacle in the way towards achieving higher intensities is the need for large and expensive optical components. In particular, the size of the gratings for recompression has almost reached the manufacture limit with areas about 1 m^2. To overcome this limitation, one needs to be able to amplify the laser pulses without prior stretching.

Based on this requirement, the concept of a plasma based Raman amplifier was firstly proposed by G. Shvets in 1998 [16]. This concept, as shown in Fig. 1.3, includes: (a) transfer of energy from a long pump pulse to a counter-propagating probe pulse through resonant excitation of a plasma wave, (b) plasmas as a gain medium can

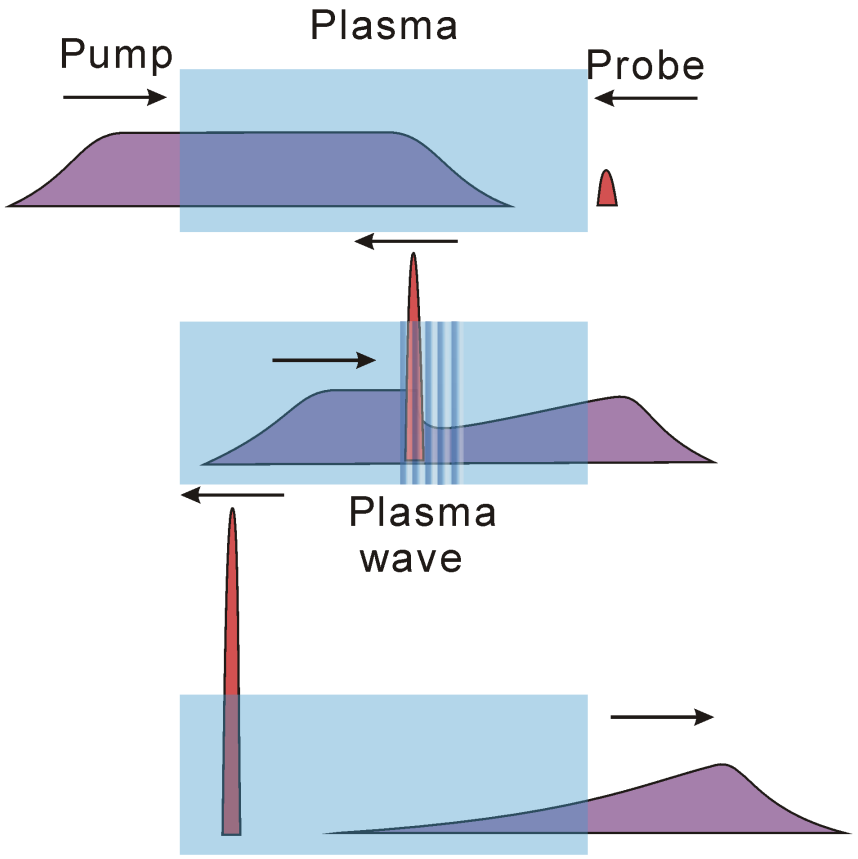

Figure 1.3: Schematics of Raman amplification of laser pulses in plasma.

withstand extremely high power densities and can offer high efficiencies over short distances. Raman amplification in plasma could lead to significant reductions in both size and cost of high power laser systems.

Laser amplification based on Raman backscattering was originally developed in gases and liquids. In 1966 Maier, Kaier and Giordmaine reported the observation of an intense light burst by shooting a ruby laser beam into a cell filled with CS_2 [17]. In this experiment, the amplified pulse duration was of the order of ps from a ns input pulse and the intensity increased by a factor of 10. Further investigations related to features of Raman and Brillouin scattering were reported experimentally [18] and theoretically [19, 20, 21] during the following years. A backward Raman laser system for practical applications was firstly designed by Glass in 1967 [22]. These studies are reviewed in detail by Kachen in his thesis in 1975 [23].

With increasing laser intensities, the breakdown of the gaseous gain medium became unavoidable. Capable of bearing high power densities, plasma was firstly proposed as a laser amplifier gain medium by Milroy [24] in 1979.

Amplification of a long pulse (ps) growing from thermal noise in plasma was firstly investigated both theoretically [25, 26, 27] and experimentally [28, 29] in the linear regime of Raman backscattering (RBS). In the following years, the geometry of a three-wave interaction between a long pump pulse, a short (fs) counter-propagating electromagnetic wave and a plasma wave was suggested [26].

Due to the gain bandwidth limitations in the linear regime, more interest was drawn to the advantages of plasma nonlinearities, namely the Compton scattering regime and the pump depletion regime [16, 30], in which it is possible not only to amplify but also to compress the laser pulses. The effects of an optical chirped pump pulse on the Raman amplification scheme was analyzed by B. Ersfeld [31], indicating that with a chirped pump pulse some similarities with features commonly associated with the nonlinear stages of Raman amplification are observed.

Experimentally, several groups have been actively investigating these schemes with

plasma from micro-capillaries [32, 33] and gas jets [34, 35, 36]. These experiments have all been performed at high plasma densities and low probe energies. Although high gain values have been achieved, the reported energy transfer efficiency is low due to the small input signal.

At the University of Strathclyde, gas-filled capillaries were designed and manufactured in the TOPS laboratory with the objective of guiding pump and probe pulses through a preformed discharge plasma channel to extend the interaction length of the two beams in plasma. Experimental investigations of the pump pulse chirp effects on the amplification process have been carried out systematically obtaining results consistent with the theoretical predictions [37]. On the basis of utilising low plasma densities, long interaction lengths and high probe intensities, the experiment described in this thesis aims to achieve the transition from the linear regime of Raman amplification to the Compton regime, in which energy transfer efficiency is high, and most importantly, pulse compression can be achieved simultaneously with broadband amplification.

1.3 Thesis outline

This thesis presents experimental work aiming to explore the possibility of a plasma based Raman and Compton amplification for ultra-short laser pulses. The thesis is divided into 6 chapters and organised as follows:

In Chapter 2, the basic theory of plasma physics and laser-plasma interactions is reviewed including wave propagation in plasma, optical heating of plasma and an introduction to parametric instabilities. Laser guiding mechanisms, in particular the theory of guiding in gas-filled capillary discharge waveguides, is also presented.

Chapter 3 concentrates on the theory of Raman amplification of laser pulses in plasma, in both linear and nonlinear regimes, together with a discussion on possible limitations of this scheme.

Chapter 4 provides a description of the experimental setup and diagnostics, in par-

ticular the Frequency-Resolved Optical Gating (FROG) system which is used to diagnose the pulse length and phase change. Actual experimental implementation is discussed in details including the production of two laser beams, the generation and control of the plasma channel and the guiding of the two laser beams.

The experimental results with systematic analysis are reported in Chapter 5. Energy and spectrum gain measurements as a function of various parameters are studied. Interesting features associated with high energy gain measurements are observed and investigated with assistance of numerical simulations.

A summary and outlook is given in Chapter 6.

Chapter 2

Theoretical background

This chapter introduces the concepts and theories behind the experiment of stimulated Raman backscattering (SRBS) in plasma. It starts with the mathematical description of plasma in Section 2.1, followed by an introduction of laser-electron interaction and propagation of waves in plasma, in Sections 2.2 and 2.3, respectively. Finally, important laser-plasma interaction phenomena, including plasma heating, guiding, filamentation and related parametric instabilities are discussed in Sections 2.4 to 2.7.

2.1 Basic concepts and description of plasma

Plasma, known as the fourth state of matter, is an ionised gas which consists of two components: electrons and ions. On one hand, a space charge separation between electrons and ions gives rise to electric fields while a flow of charged particles gives rise to magnetic fields. On the other hand, these fields dominate the motion of particles. Therefore, in plasmas, the motion of charged particles and the evolution of electromagnetic fields are tightly coupled together, which gives plasmas unique properties.

Space charges are screened in the interior of a plasma by the way the charged particles arrange themselves. This arrangement assures effective shielding of any electrostatic fields within a characteristic distance known as the Debye length (assuming $T_e \gg T_i$) [38]

$$\lambda_D = \sqrt{\varepsilon_0 k_B T_e/(q^2 n_e)}, \tag{2.1}$$

where $T_e = m_e v^2/k_B$ is the electron plasma temperature in Kelvin, with m_e the electron mass, v the electron thermal velocity and k_B the Boltzmann constant. ε_0, q and n_e are the vacuum permittivity, the electron charge and electron number density, respectively. This means that when a charge Q is inserted into a plasma, the electric field and the potential produced by this charge will be modified by the re-arrangement of particles around the charge. The Coulomb potential of the charge is then reduced by an exponential factor due to the cloud of charges surrounding it. Therefore, if the considered plasma scale is larger than λ_D, it can generally be described as an electrically neutral medium, otherwise, it can be charged.

Plasma is also a good conductor. It responds to electric and magnetic fields collectively. For example, when a small charge separation is induced in an initially uniform plasma, an electric field created by the charge separation will force the electrons to return to their initial positions and restore the charge neutrality. However, electrons will not stop but overshoot the equilibrium position due to inertia and a new electric field in the opposite direction will pull them back. This electron movement repeats periodically and will result in a collective oscillation with an angular frequency

$$\omega_{pe} = \sqrt{\frac{n_e q^2}{m_e \varepsilon_0}}, \tag{2.2}$$

known as the electron plasma frequency, which only depends on the electron density n_e. Similarly, the ion oscillation frequency is:

$$\omega_{pi} = \sqrt{\frac{Z^2 n_i q^2}{m_i \varepsilon_0}}, \tag{2.3}$$

where n_i and m_i are the ion density and mass respectively. In a quasi-neutral plasma $n_i = n_e/Z$, where Z is the charge state. The characteristic response time for electron plasma waves is $\tau_{pe} = \omega_{pe}^{-1}$ while for ion acoustic waves is $\tau_{pi} = \omega_{pi}^{-1}$. Since

$\omega_{pi} \ll \omega_{pe}$, then $\tau_{pi} \gg \tau_{pe}$. The different timescales involved in the plasma collective motions are results of the difference in mass between the electrons and ions. When electron plasma waves are considered, the heavy ions are usually regarded as a static homogeneous background. The electron plasma wave is the fastest collective phenomenon in a plasma and plays a key role in our experimental study. When acoustic waves are considered, the fast electron oscillations create an effective radiation pressure which induces ion motion on slow timescales.

2.1.1 Plasma generation

Ionisation occurs when electrons gain sufficient energy to escape the Coulomb potential of the ions. Here, we will first focus on laser-induced ionisation followed by a discussion on ionisation by electrical discharge.

When a laser beam of sufficiently high intensity impinges on a medium, the atoms of the medium will be ionised. This ionisation process, generating electrons and ions directly by the optical field and not by electron collisions, is called Optical Field Ionisation (OFI) which can be further divided into three regimes depending on the intensity and frequency of the laser field: multiphoton ionisation, tunnel ionisation and over-the-barrier ionisation. The multiphoton ionisation is the first process to occur while the tunnel ionisation starts at higher intensities. These two regimes are delineated by the Keldysh parameter [39]:

$$\gamma_{kel} = \frac{\omega}{qE}\sqrt{2I_p m_e}, \tag{2.4}$$

where ω and E are the angular frequency and electric field amplitude of the laser beam. I_p is the ionisation potential of a single atom. When $\gamma_{kel} > 1$, an electron will successively absorb a number of photons and rise to higher energy states, enabling it to leave the atom. This is the so-called multiphoton ionisation, as shown in Fig. 2.1 (a). On the other hand, when $\gamma_{kel} < 1$ the electric field of the laser pulse is high enough

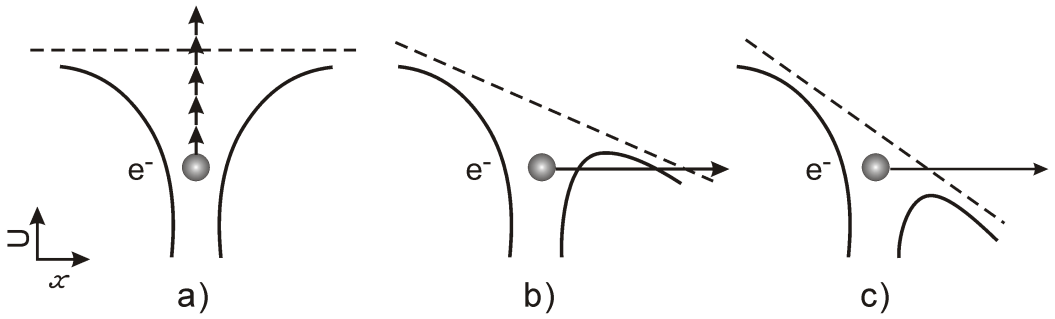

Figure 2.1: Schematic description of: (a) multiphoton (b) tunnel and (c) over-the-barrier ionisation.

and becomes comparable to the Coulomb binding potential and hence the field has the ability to distort the atomic potential, creating a potential barrier as shown in Fig. 2.1 (b). Under these circumstances, there is a possibility that the electron is able to tunnel through the potential barrier and escape from the atom. The tunnelling process is a pure quantum mechanical concept with no classical counterpart.

At even higher intensities, the potential barrier is further suppressed to the extent that the ground state electrons are no longer bound and hence escape over the barrier. This phenomenon is known as over the barrier ionisation (OTBI) and is schematically shown in Fig. 2.1 (c). The intensity required for over the barrier ionisation for an atomic level with ionisation potential $I_p[\mathrm{eV}]$ can be derived as [40]

$$I_{OTBI}\ [\mathrm{Wcm}^{-2}] = \frac{\pi^2 c \varepsilon_0^3 I_p^4}{2Z^2 q^6} \approx 4 \times 10^9 I_p^4 Z^2. \tag{2.5}$$

An alternative way of achieving gas ionisation is to apply a DC electric field across the gas. Different types of discharges and plasmas can be obtained depending on the applied voltage and the discharge current. Since a gas-filled capillary discharge waveguide (Section 5.1) is employed in this experiment, the plasma is generated by a high voltage discharge across the capillary. A current pulse passes through a capillary, free electrons strike atoms and transfer sufficient energy to bound electrons for them to escape the Coulomb potential of the ions. This is known as impact ionisation. In the case of a high electric field, avalanche breakdown will occur and form plasma.

2.1.2 Plasma description

We start by writing down the Maxwell's equations governing the electric field $\vec{E}$ and magnetic field $\vec{B}$:

$$\nabla \cdot \vec{E} = \frac{\rho}{\varepsilon_0}, \tag{2.6}$$

$$\nabla \cdot \vec{B} = 0, \tag{2.7}$$

$$\nabla \times \vec{E} = -\frac{\partial \vec{B}}{\partial t}, \tag{2.8}$$

$$\nabla \times \vec{B} = \mu_0 \vec{J} + \mu_0 \varepsilon_0 \frac{\partial \vec{E}}{\partial t}, \tag{2.9}$$

where $\rho = qn$ and $\vec{J} = qn\vec{v}$ are the charge and current density, and μ_0 is the vacuum permeability. The electromagnetic fields can be expressed by introducing scalar and vector potentials ϕ and $\vec{A}$:

$$\vec{E} = -\nabla\phi - \partial\vec{A}/\partial t, \quad \vec{B} = \nabla \times \vec{A},$$

so that the homogenous Eqs. (2.7) and (2.8) are satisfied.

Choosing the Coulomb gauge ($\nabla \cdot \vec{A} = 0$), Maxwell's equations can be expressed as:

$$\nabla^2\phi = -\rho/\varepsilon_0, \qquad \text{(Poisson's equation)} \tag{2.10}$$

$$(\frac{\partial^2}{\partial t^2} - c^2\nabla^2)\vec{A} + \nabla\frac{\partial\phi}{\partial t} = \frac{\vec{J}}{\varepsilon_0}. \tag{2.11}$$

Localised time-varying charge and current densities can act as sources of electromagnetic waves in a vacuum. Taking the curl of Maxwell's equation (2.8) (Faraday's Law), a wave equation for the electric (similar for magnetic) field with source terms can be readily derived.

$$\frac{\partial^2\vec{E}}{\partial t^2} + c^2\nabla \times (\nabla \times \vec{E}) = -\frac{1}{\varepsilon_0}\frac{\partial\vec{J}}{\partial t}. \tag{2.12}$$

The addition of sources to the wave equations makes the partial differential equations inhomogeneous. Note that the dependence of the current density on the field must be known to find solutions.

Maxwell's equations not only describe the evolution of the electromagnetic fields but also the interaction of the plasma particles.

For plasma characterisation, fluid or kinetic models are usually applied to describe the motion and distribution of electrons and ions depending on the state of the plasma. The fluid model is based on the assumption that with sufficient collisions a plasma can stay in a state of thermodynamic equilibrium, i.e. the phase velocity of an electron plasma wave is much larger than the thermal velocity. It treats the electrons and ions separately as charged fluids with Maxwell-Boltzmann velocity distributions [1]. These two-fluids penetrate each other and interact by thermal pressure and electromagnetic forces. The fluid model is suitable to describe collective effects as in Sections 2.2, 2.3 and Chapter 3.

The two-fluid description is based on the electron and ion phase space distribution functions $f_{e,i}(\vec{r},\vec{v},t)$, which characterise the particle density at a given position $\vec{r}$ and velocity $\vec{v}$ as a function of time [41]. The indices e and i for the electrons and ions will now be dropped for simplicity. The spatial density of particles $n(\vec{r},t)$ can be obtained from the distribution function as

$$n(\vec{r},t) = \int_{-\infty}^{\infty} f(\vec{r},\vec{v},t)d^3v. \tag{2.13}$$

The density $n(\vec{r},t)$ is the zeroth order moment of $f(\vec{r},\vec{v},t)$. The average velocity is given by the first order moment of the distribution function:

$$\vec{u}(\vec{r},t) = \frac{1}{n}\int \vec{v} f(\vec{r},\vec{v},t)d^3v. \tag{2.14}$$

[1] The Maxwell-Boltzmann velocity distribution is a description of the velocity probability density of electrons, when the plasma system is in equilibrium. The distribution density of the velocity is $f(\vec{v}) = \left(\frac{m_e}{2\pi k_B T}\right)^{3/2} e^{-m_e v^2/2k_B T}$.

The second order moment describing the momentum flux in the laboratory frame, is called the pressure tensor, and denoted by

$$\hat{P} = m \int (\vec{v} - \vec{u})(\vec{v} - \vec{u}) f(\vec{r}, \vec{v}, t) d^3 v, \tag{2.15}$$

if ionisation and recombination need not be considered.

Particles are neither created nor destroyed. From this fact, the phase space distribution function is constant along a trajectory, which can be expressed mathematically by the collisionless Boltzmann equation:

$$\frac{df}{dt} \equiv \frac{\partial f}{\partial t} + \frac{d\vec{r}}{dt} \cdot \frac{\partial f}{\partial \vec{r}} + \frac{d\vec{v}}{dt} \cdot \frac{\partial f}{\partial \vec{v}} = \frac{\partial f}{\partial t} + \vec{v} \cdot \nabla f + \frac{\vec{F}}{m} \cdot \frac{\partial f}{\partial \vec{v}} = 0. \tag{2.16}$$

This is an equation for noncolliding particles in electric and magnetic fields. It describes the motion of each element of the distribution through phase space according to the rates of change of position and velocity. The force $\vec{F}$ applied on the particles is the Lorentz force:

$$\vec{F} = q(\vec{E} + \vec{v} \times \vec{B}). \tag{2.17}$$

By substituting Eq. (2.17) into the Boltzmann equation, we obtain the Vlasov equation:

$$\frac{\partial f}{\partial t} + \vec{v} \cdot \nabla f + \frac{q}{m}(\vec{E} + \vec{v} \times \vec{B}) \cdot \frac{\partial f}{\partial \vec{v}} = 0. \tag{2.18}$$

To account for collisions, the Vlasov equation must be completed with a collision term $\partial f / \partial t \,|_{col}$ on the right hand side (r. h. s.). This term describes changes in the distribution due to the accumulated effects of collisions, which are short range interactions between individual particles and will lead to instantaneous changes in the particle velocities. The fields $\vec{E}$ and $\vec{B}$ on the r. h. s. of Eq. (2.17) can be determined by solving Maxwell's equations. That is, the plasma is completely described by the Vlasov and Maxwell's equations.

Furthermore, the equations describing the measurable macroscopic variables of a collective plasma can be derived by taking the different moments of the Vlasov equations. Inserting Eqs. (2.13) and (2.14) to the zeroth order moment of the Vlasov equation (i.e. integrating the Vlasov equation over the entire velocity space) yields the continuity equation for the particle density, which expresses the change in density with time

$$\frac{\partial n}{\partial t} + \nabla \cdot (n\vec{v}) = 0. \tag{2.19}$$

The first order moment of the Vlasov equation is the force equation or fluid equation of motion Eq.(2.20), describing the average force on one species due to collisions with particles of other species.

$$\frac{dv}{dt} = \left[\frac{\partial \vec{v}}{\partial t} + (\vec{v} \cdot \nabla)\vec{v}\right] = \frac{q}{m}(\vec{E} + \vec{v} \times \vec{B}) - \frac{1}{m}\nabla \cdot \hat{P} \tag{2.20}$$

The derivative of each moment of the Vlasov equation requires a moment of the next order. To obtain a closed set of equations, it is necessary to express these in terms of the lower order moments. For example, this can be realised by an approximation of the heat flow included in the second order moment of the Vlasov equation.

When $\omega/k \gg v_{th}$, the particle movement, as well as the heat flow, are negligible during the characteristic time of the wave ($\sim 1/\omega$). In this fast process, there is no exchange of heat. Therefore, the adiabatic equation of state $p/n^{\gamma} = const$ holds, where $\gamma = (N+2)/N$, with N the number of degrees of freedom. This assumption is well suited to our case where an under-dense, cold plasma is considered.

For the slow processes, i.e. $\omega/k \ll v_{th}$, there is enough time for the plasma to thermalise, causing a consistent temperature and validating the isothermal equation of state $P/n = k_B T = const$, where P, n, k_B and T are the pressure in Pascals, number density, Boltzmann constant and temperature in kelvin.

Applying Eqs. (2.19), (2.20) and the equation of state for the species composing the plasma, i.e. electrons and ions, constitute the two-fluid model. Together with Maxwell's equations, which describe the evolution of electromagnetic fields, including the laser radiation and those from the charges and currents in the plasma, it provides a complete description of the collective effects in the plasma.

However, with the advent of ultrahigh intensity femtosecond lasers, plasmas can be excited out of the state of thermodynamic equilibrium. Single particle effects arise among electrons and ions. There are two common approaches for the kinetic theory to handle these non-equilibrium plasmas. One is by tracking the distributions functions $f(\vec{r},\vec{v},t)$ at each point of the complete phase space of all species. The other is known as the particle-in-cell (PIC) technique which includes kinetic information by following the trajectories of a large number of individual particles. PIC simulations are performed for the experiment described in this thesis and the results will be discussed in Chapter 6.

2.2 Laser-electron interaction

After the introduction of the basic concepts and the description of plasma, laser-electron interaction will be considered in the framework of the fluid description of plasmas. With an electromagnetic wave propagating in a plasma, the single electron response and the collective effect will be discussed in this section.

2.2.1 Electron quiver motion

In an ideal case, when a plane wave propagates in plasma, the electrons will oscillate at the laser frequency in response to the electric field of the laser. This motion is called the quiver motion. The driving force from the light wave is the Lorenz force therefore the equation of motion for a single electron in an electromagnetic wave is:

$$\frac{d\vec{p}}{dt} = q(\vec{E} + \vec{v} \times \vec{B}), \tag{2.21}$$

where $\vec{p} = m_e\vec{v}$ is the momentum of the electron. On the r. h. s., $\vec{E} = -\partial\vec{A}/\partial t$ and $\vec{B} = \nabla \times \vec{A}$ denote the electric and magnetic fields of the light wave ($\phi = 0$). Neglecting the relativistic effects for the laser intensities used in the experiment described in this thesis, the oscillatory velocity is:

$$\vec{v_{os}} = \frac{q\vec{A}}{m_e} = \vec{a}c, \tag{2.22}$$

where $\vec{a}$ is the normalised vector potential, which offers a criterion to distinguish between different regimes of laser plasma interaction. When $|\vec{a}| < 1$, as the case for this experiment, the relativistic effects can be neglected. In terms of laser pulse intensity I_0, for linearly polarised laser pulse, the expression for the amplitude of the normalised vector potential is given by: $|\vec{a}| \approx 8.5 \times 10^{-10}\ \lambda\ [\mu\text{m}]\ I_0^{1/2}\ [\text{Wcm}^{-2}]$. In this thesis only intensities in the range of $10^{13} \sim 10^{15}$ Wcm^{-2} will be considered, and thus relativistic effects will be neglected. When $|\vec{a}| \geqslant 1$, the plasma electron motion is relativistic and nonlinear, therefore Eq. (2.22) does not apply in this case.

2.2.2 Ponderomotive force

In the previous section, a plane wave was assumed. However, spatial inhomogeneities will give rise to another non-linear effect that plays a key role in the laser plasma interaction. In the non-relativistic case ($|\vec{a}| < 1$), consider a single electron oscillating in an electromagnetic field $\vec{E} = \vec{E_0}(\vec{r})\cos\omega t$. Neglecting the $\vec{v} \times \vec{B}$ term, the first order of the equation of motion Eq. (2.21) can be written as Eq. (2.23) at the initial position $\vec{r_0}$ [42]:

$$m\frac{d\vec{v_1}}{dt} = qE(\vec{r_0}). \tag{2.23}$$

The first order of $\vec{v}$ and $\vec{r}$ can be evaluated as:

$$\vec{v_1} = \vec{v_{os}} \sin \omega t \; ; \quad \delta \vec{r_1} = \frac{\vec{v_{os}}}{\omega} \cos \omega t, \tag{2.24}$$

where $\vec{v_{os}} = q\vec{E_0}/m\omega$ has been described in Eq.(2.22). Applying Taylor expansion to the electric field, we get:

$$\vec{E(r)} \cong \vec{E}(\vec{r_0}) + (\partial \vec{r_1} \cdot \nabla)\vec{E}|_{r=r_0} + ... \tag{2.25}$$

The second order part of the equation of motion can be deduced as expressed in Eq. (2.26) using Eq. (2.25):

$$m\frac{d\vec{v_2}}{dt} = q[(\partial \vec{r_1} \cdot \nabla)\vec{E} + \vec{v_1} \times \vec{B_1}], \tag{2.26}$$

where $\vec{B_1}$ can be obtained from Maxwell Faraday equation (2.8)

$$\vec{B_1} = -\frac{1}{\omega} \nabla \times \vec{E}|_{r=r_0} \sin \omega t. \tag{2.27}$$

Substituting Eqs. (2.24) and (2.27) back into Eq. (2.26) and averaging over a laser cycle (such that $\left\langle \cos^2(\omega t) \right\rangle = \left\langle \sin^2(\omega t) \right\rangle = \frac{1}{2}$) gives the ponderomotive force on an electron

$$m\left\langle \frac{d\vec{v_2}}{dt} \right\rangle_{av:2\pi/\omega} = -\frac{1}{4}\frac{q^2}{m\omega^2} \nabla \vec{E_0^2} \equiv \vec{F}_{pond}. \tag{2.28}$$

The ponderomotive force is proportional to the electric field intensity gradient. It expels the electrons to the region where the electromagnetic field is less intense. One of the most important effects of the ponderomotive force is the introduction of a charge separation between electrons and ions, which will eventually give rise to collective plasma oscillations. Protons and ions are considerably heavier therefore are treated as stationary when considering the ponderomotive force for short laser pulses (fs-ps).

2.3 Propagation of waves in plasma

Plasma can sustain many types of waves, such as transverse electromagnetic waves and longitudinal electrostatic waves. Ignoring magnetised plasmas, an introduction to wave propagation will be presented with the two-fluid description. The propagation of electromagnetic wave in plasma will be considered first, followed by the description of the longitudinal electron and ion plasma waves.

2.3.1 Electromagnetic wave

When a laser beam enters a plasma, electrons quiver in the electromagnetic field. They oscillate and radiate at the laser frequency with phase shifted relative to the laser radiation field. The dispersion relation of an electromagnetic wave of frequency ω and wave number k is given by

$$\omega^2(k) = \omega_{pe}^2 + c^2k^2. \tag{2.29}$$

From this equation, it is easy to see that an electromagnetic wave with frequency $\omega < \omega_{pe}$ cannot propagate in the plasma but is reflected from the boundary of the plasma. This phenomenon can be explained by the characteristic time of plasma electrons to shield out the field of the light wave, ω_{pe}^{-1}. The electron plasma density at which the plasma frequency equals the frequency of the incident light is called the critical density $n_c = \omega^2 m_e \varepsilon_0 / e^2$. At the laser wavelength of 800 nm, the critical density is 1.7×10^{21} cm^{-3}.

When light propagates in plasma, the refractive index can be derived from Eq. (2.29)

$$\eta = \frac{c}{v_{ph}} = \frac{ck}{\omega} = \sqrt{1 - \frac{\omega_{pe}^2}{\omega^2}}. \tag{2.30}$$

The refractive index is smaller than 1 therefore the phase velocity $v_{ph} = c/\eta$ is greater than the speed of light, while the group velocity is $v_g = c\eta$.

2.3.2 Electron plasma wave

Electron plasma waves are also called Langmuir waves. They are longitudinal waves formed by the electron density oscillations. The electric field is generated by charge displacement and the energy oscillates between the kinetic energy of the electrons and the potential energy of the electrostatic field. They are the most common and the fastest collective phenomena in a plasma. The electron plasma wave dispersion relation is

$$\omega_e^2 = \omega_{pe}^2 + 3{k_e}^2 v_{th}^2. \tag{2.31}$$

This equation is also known as Bohm-Gross dispersion relation [43]. The dominant term in this equation is ω_{pe}^2 while the $3{k_e}^2 v_{th}^2$ is a thermal correction, where v_{th} is the electron thermal velocity and k_e is the wave number of the longitudinal wave. For our experiment, the electron plasma wave frequency depends mainly on the electron density and weakly on the wave vector and temperature.

2.3.3 Ion acoustic wave

The ion acoustic wave is driven by both the ion pressure and the electron pressure. Electrons and ions oscillate together. Its frequency ω_i is low compared with the electron plasma wave since the ion mass is much larger than the electron mass. The dispersion relation of ion acoustic waves is

$$\omega_i = v_s k_i, \tag{2.32}$$

where $v_s = \sqrt{(Zk_BT_e + \gamma_i k_B T_i)/m_i}$ is the sound velocity, T_i the ion temperature and γ_i the adiabatic coefficient of the ions.

We can see from the dispersion relation that this wave propagates in a plasma in a similar way to an ordinary sound wave in a neutral gas. There are two differences: first, unlike sound waves, ion acoustic waves can also propagate in a collisionless medium, because the charged ions interact over long distances via the electrostatic

field; second, a plasma also contains electrons which contribute to the wave dispersion equation which can be seen from the first term (Zk_BT_e) in the equation for the sound velocity.

2.4 Plasma heating

When an electromagnetic wave propagates in a plasma, a number of phenomena are responsible for plasma heating. The most important mechanisms related to the situation considered in this thesis are inverse bremsstrahlung heating and Landau damping.

2.4.1 Inverse bremsstrahlung

Bremsstrahlung is radiation originating from particle deceleration due to collisions between charged particles. In plasma, bremsstrahlung mainly arises from electron-ion collisions. Since the ions are much heavier than the electrons, the bremsstrahlung radiation comes mostly from electron deceleration. The electrons are in free states before and after the emission of bremsstrahlung radiation, therefore the process is also referred as free-free radiation.

When a laser beam propagates in a plasma, the electrons can also absorb energy from the laser beam. From a classical viewpoint, the electron oscillates in the electric field of the laser beam. During a collision with an ion, the electron is knocked out of phase with the electric field, and oscillatory energy of the electron is converted to random thermal energy. This process is called inverse bremsstrahlung or sometimes free-free absorption. As a result of the inverse bremsstrahlung, laser energy is transferred to electrons in the form of thermal velocity. Therefore, the inverse Bremsstrahlung process is believed to play an important role in the heating of plasma electrons by laser radiation. The attenuation of laser intensity due to inverse bremsstrahlung occurs at the rate $\nu_o = \frac{1}{2}(n_e/n_c)\nu_{ei}$ where $\nu_{ei} \sim Zn_eT_e^{-3/2}$ is the electron-ion collision rate [44]. The absorption rate decreases very quickly with increasing temperature. For cold

plasma, the collision rate is higher thus the laser attenuation is more severe. With a 1×10^{18} cm^{-3}, 5 eV and 4 cm plasma, corresponding to the plasma used in the experiment described in this thesis, a maximum of 25% attenuation is expected.

2.4.2 Landau damping

Landau damping is named after Lev Landau who first realised this phenomenon in 1946 [45, 46]. Compared with inverse bremsstrahlung heating, Landau damping is a mechanism that can transfer energy between plasma wave and electrons collissionlessly. At high plasma temperature, strong Landau damping occurs and electron plasma waves can be strongly damped.

To have a simple physical explanation for this effect we start with the motion of a charged particle situated in a one-dimensional electric field $E_0 e^{[i(kx-\omega t)]}$ can be described as

$$\frac{\mathrm{d}^2 x}{\mathrm{d}t^2} = \frac{q}{m} E_0 e^{i(kx-\omega t)}. \tag{2.33}$$

If the particle starts with velocity u_0 at position x_0, then we may substitute $x = x_0 + u_0 t$ in the electric field term which presents the position of the particle on its unperturbed trajectory

$$\frac{\mathrm{d}u}{\mathrm{d}t} = \frac{q}{m} E_0 e^{i(kx_0+ku_0t-\omega t)}, \tag{2.34}$$

which gives

$$u - u_0 = \frac{q}{m} E_0 \left[\frac{e^{i(kx_0+ku_0t-\omega t)} - e^{ikx_0}}{i(ku_0 - \omega)} \right]. \tag{2.35}$$

When $ku_0 - \omega \to 0$, Eq. (2.35) reduces to

$$u - u_0 = \frac{q}{m} E_0 t e^{ikx_0}. \tag{2.36}$$

showing that particles with u_0 close to ω/k, have velocity perturbations changes in time. These so-called resonant particles gain energy from, or lose energy to, the wave, and are responsible for the damping.

The physics of Landau damping is that if an electron moves much slower or faster than the phase velocity of the plasma wave, the net wave-electron energy exchange is null, however, when the electron moves with approximately the same speed as the wave, i.e. the electron is in phase with the wave, it is exposed to a nearly constant electrostatic field, therefore the energy exchange is not zero anymore. As shown in Fig. 2.2, when an electron is slightly slower than the phase velocity of the wave, it will get accelerated and gain energy from the wave. A slightly faster electron will be caught in the electrostatic field and, at the same time, give energy to the wave. When the particle velocity is Maxwellian distribution function, the number of particles with velocities slightly less than the wave phase velocity is larger than the number of particles with velocities slightly greater. Hence the overall result is the plasma wave will lose energy to particles. This processes of the plasma wave and electrons exchange energy without collision is called Landau damping.

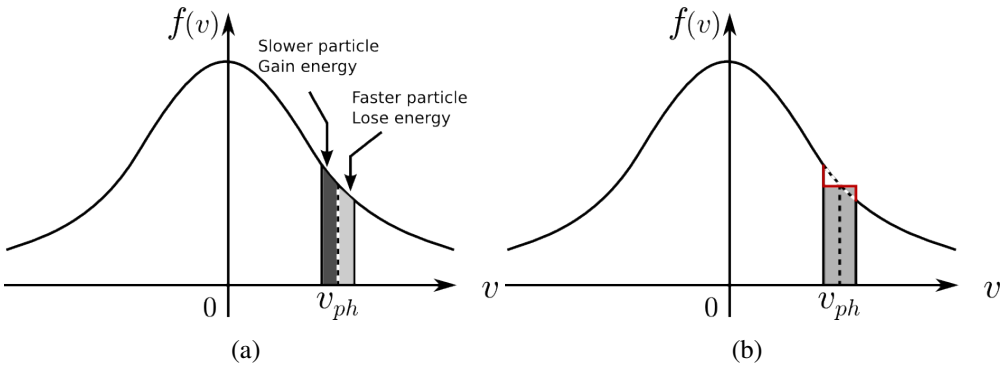

Figure 2.2: Schematic of Landau damping. (a) Due to Maxwellian distribution function of the particle velocity, there are more particles gaining energy from the wave than losing to the wave. (b) Deformation of the electron velocity in the region $v \approx v_{ph}$ after the energy exchange.

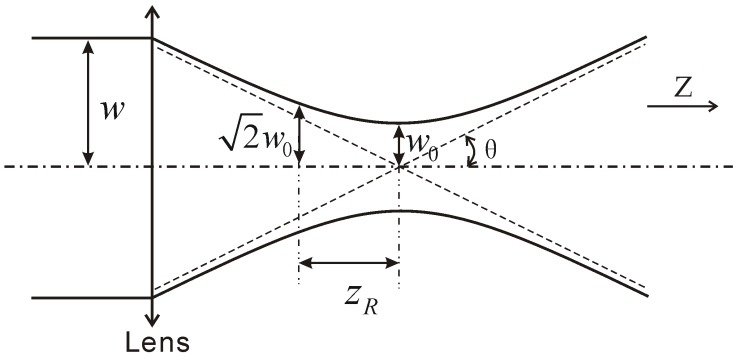

Figure 2.3: Focusing of a laser beam.

2.5 Guiding of laser beams

High laser intensities are required in a wide range of applications. They can be obtained simply by focusing a laser beam to a small spot. The focusing of a perfect Gaussian radial profile laser beam is illustrated in Fig. 2.3. The minimum beam radius along the propagation direction is called the beam waist w_0 and the laser intensity at w_0 is I_0.

$$w_0 = \frac{\lambda f}{\pi w}, \tag{2.37}$$

where w is the original radius of a laser beam, λ the laser wavelength and f the focal length of the focusing element. Here the beam radius is defined as the distance from the beam axis to where the optical intensity drops to $1/e^2 (\approx 13.5\%)$ of the value on the beam axis.

With further propagation (assumed in z direction) the laser spot size $w(z)$ increases and the laser $I(z)$ intensity drops as:

$$w(z) = w_0 \sqrt{1 + \left(\frac{z}{z_R}\right)^2}, \tag{2.38}$$

$$I(z) = \frac{I_0}{1 + \left(\frac{z}{z_R}\right)^2}, \tag{2.39}$$

where $z_R = \pi {w_0}^2/\lambda$ is the Rayleigh length which is defined as the distance from the

beam waist along the propagation direction to where the beam radius is increased to $\sqrt{2}w_0$ and the laser intensity drops to $\frac{1}{2}I_0$. When z is much larger than the Rayleigh length, the beam divergence half-angle is defined as:

$$\theta \cong \tan\theta = \frac{\lambda}{\pi w_0}. \tag{2.40}$$

When high laser intensities need to be sustained over distances longer than the Rayleigh length, different techniques can be employed to extend the laser high intensity region.

2.5.1 Introduction of different guiding mechanisms

1. Step refractive index guiding

The waveguide consists of two kinds of materials combined as a core surrounded by a cladding, as shown in Fig. 2.4 (a). When the refractive index of the core is larger than the cladding ($\eta_{core} > \eta_{clad}$), it can be seen from Fresnel equations when the incidence angle θ satisfies $\theta < \theta_{max}$ ($n\sin\theta_{max} = \sqrt{n_{core}^2 - n_{clad}^2}$, n is the refractive index of the medium where the ray is incident from), then a incident ray will experience total internal reflection (TIR).

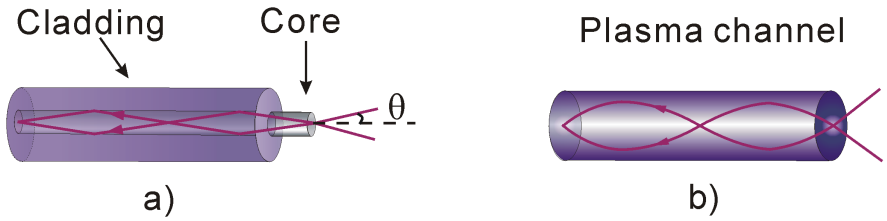

Figure 2.4: Two guiding mechanisms: (a) Step refractive index guiding (b) Gradient refractive index guiding.

However, the guiding of high intensity laser beams by structures with $\eta_{core} > \eta_{clad}$ is limited by the damage threshold of the core material. When the laser intensity is greater than 10^{14} Wcm^{-2}, the characteristic of the core material will be changed by the laser pulse. To avoid any damage, vacuum or a gas can be chosen as the core ma-

terial. Consequently, with any solid cladding, $\eta_{core} > \eta_{clad}$ will not be satisfied so that the propagation losses are unavoidable. However, with grazing incidence and due to the fact that close to the focus the beam divergence is small, the losses can be sustained at an acceptable range. This type of waveguide is called grazing incidence waveguide [47]. Since the intensity at the wall is approximately 10^{-4} of that on axis, in principle, it should be possible to guide pulses with a peak intensity up to 10^{18} Wcm^{-2}. In practice, fluctuations may reduce the damaging threshold by one to two orders of magnitude. A monomode guiding of a 120 fs laser pulse at an intensity up to 10^{16} Wcm^{-2} in hollow dielectric capillary tubes as long as 10 cm was achieved experimentally [48].

2. Gradient refractive index guiding

Waveguides with smoothly changing refractive index in the radial direction can also be used to counteract beam diffraction, as shown in Fig. 2.4 (b). The refractive index decreases with the distance from the axis and leads to the wavefront of the laser beam bending towards the axis of the beam. When applying this mechanism to guide high intensity laser beams, plasma is always chosen as the guiding medium to avoid destroying solid materials.

It has been found that a refractive index profile suitable for guiding can be created in plasma in many ways, e.g. using igniter-heater technique, or ablating capillaries with a discharge, relying on the ponderomotive force from the laser pulse, or utilising the electron mass change when relativistic intensities are used.

- Igniter-heater

The igniter-heater technique is based on delivering two consecutive laser pulses into a gas jet or gas cell. The igniter pulse ($\leq$ 100 fs, $\sim 5 \times 10^{14}$ Wcm^{-2}) is used to generate the plasma by optical field ionisation of the gas and then a long heater pulse ($\sim$ 100 ps) to further ionise and heat the plasma. The shock wave driven by inverse bremsstrahlung heating propagates away from the axis and hydrodynamic expansion results in an electron density with a minimum value on axis, which corresponds to a

maximum value of the refractive index.

- Ponderomotive guiding

When the power of the laser pulse is sufficiently high, ponderomotive guiding can occur. As explained in Section 2.2.2, the ponderomotive force pushes plasma particles away from regions of high field intensity. Particle motion causes a change in the plasma density with a higher value away from the laser beam. Such a density profile leads to a refractive index change that acts as a convex lens which focuses the beam to a smaller diameter.

- Relativistic guiding

When the laser intensity is of the order of 10^{18} Wcm^{-2}, the electron quiver motion becomes relativistic and the Lorentz factor $\gamma = \left(1 - v^2/c^2\right)^{-1/2}$ affecting the electron mass cannot be neglected. Assuming the laser pulse propagating in the plasma has a Gaussian radial profile, the Lorentz factor and the electron mass are maximum on axis and decrease as the laser intensity decreases. This results in a lower on axis plasma frequency. Thus, the radial profile of the refractive index peaks on axis and the gradient of the refractive index guides the laser beam. This guiding mechanism is known as relativistic guiding [49, 50] and has been obtained experimentally in several laboratories [51, 52]. The critical power for a laser pulse with ideal Gaussian radial profile to achieve the relativistic self-focusing in a uniform plasma is given by [53]

$$P_{crit}[\mathrm{GW}] \approx 17.4 \left(\frac{\omega_0}{\omega_p}\right)^2. \tag{2.41}$$

There are three points worth noting: (1) the power required for relativistic self-focusing is lower for higher plasma densities; (2) ponderomotive guiding does not occur for pulses shorter than the plasma wavelength [53, 54]; (3) ponderomotive and relativistic guiding usually occur together. The ponderomotive force can increase the self-focusing effect and reduce the power required to cancel diffraction to $P_{crit}[\mathrm{GW}] \approx 16.2\,(\omega_0/\omega_p)^2$ [55, 56].

- Capillary

Another method of forming the plasma channel is the discharge ablated capillary waveguide. This method employs a high voltage discharge to ablate the capillary wall and ionise this material to form the plasma. Since the temperature profile across the capillary has its peak on axis, and the plasma pressure is uniform, this results in a plasma density minimum on axis which will overcome the laser beam divergence [50]. This technique was initially investigated by Zigler et. al. [57, 58, 59]

One drawback of this technique is that carbon impurities will give rise to distortion, and further ionisation will result in defocusing and blue-shift of the laser spectrum. Furthermore, the lifetime of the device is usually limited to less than 1000 shots due to ablation of the capillary wall. To overcome these drawbacks, an alternative way of forming the plasma in capillary has been developed by using a discharge to ionise pre-filled gas in the capillary. The guiding principle will be described in detail in the following section since it is the method used in the experiment described in this thesis.

2.5.2 Guiding of laser beams in gas-filled discharge capillary

Inspired by Zigler's work, Spence and Hooker developed the gas-filled capillary discharge waveguide [60]. Among all the guiding techniques, this method offers a number of advantages: high transmission efficiency, plasma density tunability and long device lifetime. However, it also comes with some disadvantages, which will be discussed in the experimental chapter.

The guiding process of the gas-filled capillary can be divided into three steps. First, the application of a high voltage along the capillary, pre-forming plasma by ionisation of H_2. Second, the formation of a radial density profile. At the time when the ionisation is almost complete, the current from the HV power supply is still rising. The thermal conduction becomes significant and the radial temperature distribution becomes inhomogeneous. Based on the ideal gas law

$$P = nk_BT, \tag{2.42}$$

assuming the pressure P inside the capillary is constant, the plasma density is inversely proportional to the temperature. Since the plasma close to the wall is colder, the electron density increases with the radial distance from the axis. Finally, a quasi-steady-state equilibrium is achieved and the plasma temperature is maximum on axis corresponding to an axial minimum in the electron density profile. According to Eq. (2.2) and (2.30), the refractive index depends on the plasma density. Thus, it has a maximum value on axis. The transverse profile of the refractive index and the electron density are shown in Fig. 2.5.

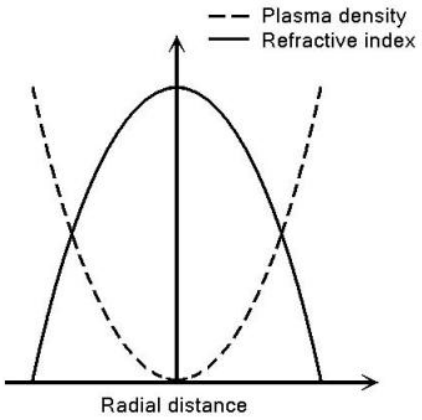

Figure 2.5: Ideal plasma density and refractive index distribution in a gas-filled capillary.

Efficient guiding of a Gaussian laser pulse in an ideal plasma channel requires a parabolic plasma density profile, as described by

$$n(r) = n(0) + \Delta n_{ch} \left(\frac{r}{r_{ch}} \right)^2, \tag{2.43}$$

where $n(0)$ and $n(r)$ are the electron density on axis and at radius r of the plasma channel, r_{ch} is the radius of the channel wall and Δn_{ch} corresponds to the density increase from the axis to the wall of the channel which is to be determined experimentally. Considering a Gaussian laser pulse focused at the entrance of the plasma channel, the evolution of the spot size $w(z)$ can be derived from the differential equation [50]:

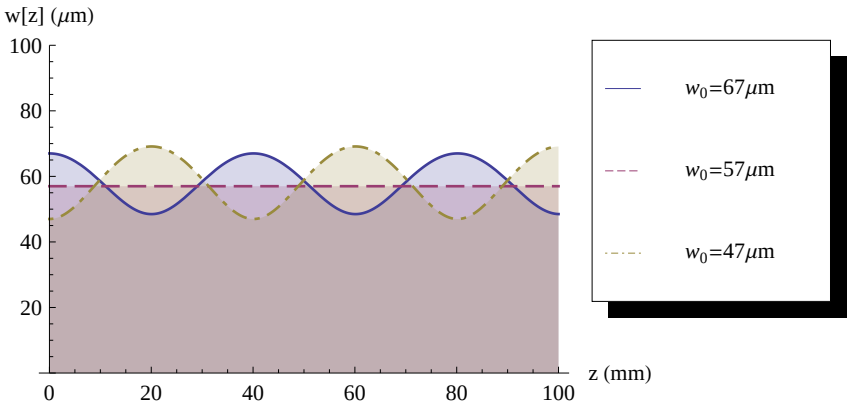

Figure 2.6: Propagation of laser beams in a plasma channel with $w_0 = w_M$, $w_0 < w_M$ and $w_0 > w_M$.

$$\frac{d^2w(z)}{dz^2} = \frac{4}{k^2 w(z)^3}\left(1 - \frac{w(z)^4}{w_M^4}\right). \tag{2.44}$$

Assuming $dw/dz = 0$ at $z = 0$, $w(z)$ can be calculated from

$$w(z)^2 = \frac{w_0^2}{2} + \frac{w_M^4}{2w_0^2} + \left(\frac{w_0^2}{2} - \frac{w_M^4}{2w_0^2}\right)\cos\left(\frac{2\pi z}{Z_{osc}}\right), \tag{2.45}$$

where w_0 is the waist of the laser beam at $z = 0$, and w_M is the matched beam waist, as expressed in Eq. (2.46), in which $r_e = e^2/(mc^2)$ is the classical electron radius.

$$w_M = \left(\frac{r_{ch}^2}{\pi r_e \Delta n_{ch}}\right)^{1/4} \tag{2.46}$$

When $w_0 = w_M$ the laser pulse propagates in the plasma channel with a constant spot size. However, when the beam waist is not matched, i.e. $w_0 \neq w_M$, the spot size will oscillate between two values with a period of oscillation given by

$$Z_{osc} = \frac{\pi^2 w_M^2}{\lambda}. \tag{2.47}$$

For a capillary with radius of 150 μm and plasma density of 1×10^{18} cm^{-3}, w_M is calculated to be 55 μm and Z_{osc} is 40 mm. Fig. 2.6 shows the propagation of laser beams with $w_0 = w_M$, $w_0 < w_M$ and $w_0 > w_M$.

2.6 Filamentation

When an intense laser pulse is propagating in a dielectric medium, a combination of two counteracting nonlinear optical effects (one focusing and one defocusing) can lead to the formation of a dynamic structure during propagation. When the two contributions are of equal strength, the radius of the structure is relatively constant. As a result, a focused laser pulse maintains a tight focus over a distance much longer than the diffraction length without the help of any external guiding mechanism. This phenomenon is known as filamentation.

There are many optical effects contributing to the formation of filament. For solid media or gasses, primarily it is the result of an intricate competition between self-focusing by optical Kerr effect (OKE) and defocusing by ionisation of the medium and diffraction. It is generally characterised by the following three steps:

1. For the range of laser intensities considered here, the dominant nonlinearity is the optical Kerr effect. The refractive index of the medium depends on the laser intensity which is described by

$$\eta(I) = \eta_0 + \eta_2 I + \cdots, \tag{2.48}$$

where η_0 is the linear refractive index of the medium and η_2 is the nonlinear refractive index ($\eta_2 > 0$ for a neutral gas). A Gaussian profile laser beam with higher intensity in the center induces a refractive index curve with maximum on axis. The laser pulse self-focuses when the laser power exceeds the nonlinear focusing power $P_N = \lambda^2/2\pi\eta_0\eta_2$ [61, 62].

2. As the pulse self-focuses, the peak intensity increases above the ionisation threshold of the medium. Under-dense plasma is created via multiphoton ionisation or tunnel ionisation. The presence of the plasma decreases the local refractive index

$$\eta_r(r) = \eta_0 + \eta_2 I(r) - \omega_p^2(r)/2\omega^2, \tag{2.49}$$

where the last term on the r. h. s. is proportional to the local plasma density, $\omega_p^2(r) \sim n(r)$. The effect of the plasma is similar to a diverging lens, causing beam defocusing, which assures no saturation of the process [50, 63, 64]. With decreasing intensity, the ionisation process is reduced.

3. If the two processes are properly balanced, the laser beam can self-guide and propagate over many vacuum Rayleigh lengths as a filament, as shown in Fig. 2.7, until it loses too much energy to produce ionisation. When the diffraction is not compensated, the filament breaks.

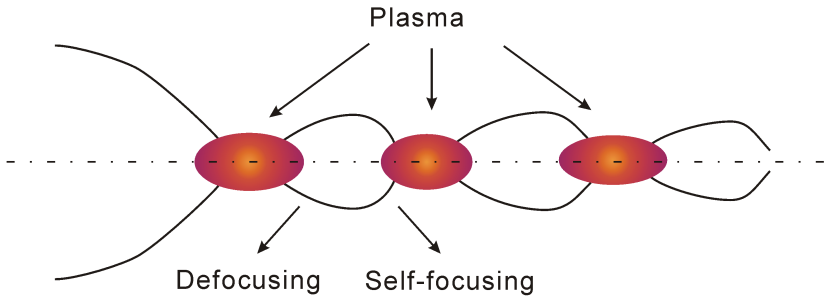

Figure 2.7: Evolution of filament by focusing-defocusing cycles.

Filamentation is accompanied by many effects, such as spectral broadening (white light generation) [65], pulse compression [66], intensity clamping [67], T-ray (Terahertz radiation) emission [68] and harmonic generation [69] etc. Some of them are beneficial to our experimental study whereas some are known to be harmful. In this experiment, spectral broadening caused by self-phase-modulation and ionisation, is utilised to generate a frequency shifted probe beam that satisfies Eq. (2.50). The experimental methods will be described in detail in Chapter 4.

Filamentation in plasma usually refers to an instability where spatial fluctuations in laser intensity grow due to self-focusing at the intensity maxima, leading to breakup of broad pulses.

2.7 Parametric instabilities in laser-plasma interactions

Parametric instabilities are a kind of energy transfer processes, in which a pump wave deposits energy to coupled daughter waves. In laser-plasma interactions, the pump wave and the daughter waves of parametric instabilities can be electromagnetic as well as plasma waves. The energy and momentum conservation relations must be satisfied:

$$\omega_1 = \omega_2 + \omega_3, \quad \vec{k_1} = \vec{k_2} + \vec{k_3}, \tag{2.50}$$

where ω_1 and $\vec{k_1}$ are the frequency and wave number of the incident pump wave, whereas $\omega_{2,3}$ and $\vec{k_{2,3}}$ represent the frequencies and wave numbers of the excited waves.

To trigger the instability the amplitude of the pump wave needs to exceed a threshold. In the amplification process the daughter waves first experience an exponential gain in the linear stage and the growth rate is proportional to the pump amplitude. There are four main parametric instabilities in laser-plasma interactions: the decay of an electromagnetic pump wave into (1) two electron plasma waves, (2) an electron and an ion plasma wave, (3) an electron plasma wave and a second electromagnetic wave, and (4) an ion plasma wave and a second electromagnetic wave. The first two types of instabilities can only occur for electron densities $n_e \sim n_{crit}/4$ and $n_e \approx n_{crit}$, respectively. Those plasma density values are much higher than what we use in our experiment. The third type is known as Raman scattering, the most relevant instability to this work, and the fourth type is Brillouin scattering. The last two instabilities will be discussed in detail.

In addition to the four mentioned instabilities, other types of parametric instabilities exist. For example, laser radiation can decay into a scattered wave and an electron-acoustic wave, which is called stimulated electron-acoustic decay instability [70]. Since the amplitude of the acoustic wave is three orders of magnitude smaller than that of the electron plasma wave, this is not an important mechanism.

2.7.1 Stimulated Raman scattering

Raman scattering, is named after Indian physicist Sir Chandrasekhara Venkata Raman, who first published observations of the effect in 1928 [71]. Austrian physicist Adolf Smekal theoretically described the effect in 1923. When photons are scattered from an atom or molecule, most photons are elastically scattered (Rayleigh scattering), such that the scattered photons have the same frequency as the incident photons. However, it is also possible for the incident photons to interact with the molecules in such a way that energy is either gained or lost so that the scattered photons are shifted in frequency to Stokes (down-shift) or anti-Stokes (up-shift) frequencies. However, the anti-Stokes scattering is usually weak. Such inelastic scattering is called Raman scattering which can happen in a Raman-active medium such as some type of gas, liquid, crystals or plasma. The energy difference between the absorbed and emitted photon corresponds to the energy difference between two resonant states of the material and is independent of the absolute energy of the photon.

Raman scattering can also happens in plasma. When to see this phenomenon with the classical wave interpretation, it can simply be characterised as the resonant decay of an incident electromagnetic pump wave into a frequency shifted scattered electromagnetic wave and an electron plasma wave and this process satisfies the energy and momentum conservation relation as expected [72]. Raman scattering can grow spontaneously from noise or can be stimulated by a probe wave at the Stokes frequency ($\omega - \omega_{pe}$), leading to its amplification. The latter case, known as stimulated Raman back scattering (SRBS), offers the potential of amplifying laser pulses to powers exceeding the damage threshold of current state-of-the-art solid state amplifiers. The amplification mechanism will be studied in Chapter 3.

The Raman instability has been investigated thoroughly in various situations and the growth rates are calculated depending on the direction of the scattered electromagnetic wave, i.e. Raman backscattering, Raman forward scattering and Raman side scattering. The relationship between the frequencies and wave numbers of the light

Scattering Type	Resonance Conditions	Growth Rate
Stimulated Raman forward scattering	$\omega_0 = \omega_1 + \omega_{pe}$ $k = \frac{\omega_{pe}}{c}$	$\gamma \approx \frac{1}{2\sqrt{2}} \frac{\omega_{pe}^2}{\omega_0} a_0$
Stimulated Raman backscattering	$\omega_0 = \omega_1 + \omega_{pe}$ $k = k_0 + \frac{\omega_0}{c}\sqrt{1 - \frac{2\omega_{pe}}{\omega_0}}$	$\gamma \approx \frac{1}{2}\sqrt{\omega_{pe}\omega_0} a_0$

Table 2.1: Resonance conditions and growth rate of forward and backward Raman scattering [26].

waves and plasma wave, and the growth rate for Raman scattering are listed in Table 2.1 [26]. Although the growth rate of the Raman side scattering is in between of the Raman backscattering and forward scattering, it is of little importance in the amplification process as the side scattered light leaves the pump source immediately, i.e. the duration of interaction is very short. As shown in Table 2.1, the growth rate for forward Raman scattering is much less than for backward Raman scattering. Taking the parameters used in the experiment described in this thesis for example (plasma density: 1×10^{18} cm^{-3}, pump beam energy: 500 mJ, pulse duration: 250 ps, focal spot size: 60 μm, wave length: 800 nm), the growth rate for forward Raman scattering is $\gamma \approx 1.4 \times 10^9$ s^{-1}, while for Raman backscattering is $\gamma \approx 5.2 \times 10^{11}$ s^{-1}. But the forward instability has much more time to develop as the scattered wave travels in the same direction as the incident wave. It can diminish the gain and therefore should be suppressed in the experiment.

2.7.2 Stimulated Brillouin scattering

Stimulated Brillouin scattering (SBS) is a resonant decay of a laser wave into a scattered electromagnetic wave and an ion acoustic wave. The ion acoustic waves have very low frequency, but a significant wave vector of the order of the laser's wave vector k_0, therefore a significant portion of the energy can be transferred to the scattered light which has almost the same wavelength as the laser light. (For backscattering: $\omega_{pi} \ll \omega_0$, therefore $\omega_1 \approx \omega_0, k_1 \approx -k_0, k_{pi} \approx 2k_0$) Due to the long time period of the

ion acoustic waves, typically in *ps* scale, SBS can become important with a long and intense pump pulse. For Brillouin scattering, the dispersion relations of the sound and electromagnetic waves in a plasma only allow backward scattering. The growth rate for the stimulated Brillouin backscattering is:

$$\gamma = \frac{1}{2\sqrt{2}} \sqrt{\frac{c}{v_s}} \omega_{pi} a_0, \tag{2.51}$$

where v_s is the sound velocity in the plasma. The electrostatic fields are much smaller for ion acoustic waves, therefore in SBS, the saturation occurs at higher wave amplitudes comparing with the SRS. For our experimental parameters, the growth rate of SBS is $\gamma \approx 1.4 \times 10^{11}$ s^{-1}.

Chapter 3

Raman amplification of laser pulses in plasma

A comprehensive review of Raman and Compton amplification of laser pulses in plasma is presented in this chapter. The amplification mechanism is explained first. Following this, different regimes are introduced, including the linear regime and the pump depletion regime of Raman amplification as well as the superradiant amplification (i.e. the Compton regime). The distinctions of Raman and superradiant amplification are then discussed. Finally, factors that could limit the laser energy gain in the Raman amplification process are described and discussed.

3.1 Basic theory of Raman amplification

3.1.1 Raman amplification mechanism

The physics of the Raman scattering can be described in two ways. From a macroscopic point of view, we consider a laser pulse propagating in a plasma with uniform density and constant temperature. An initial density modulation due to the thermal fluctuations backscatters the laser pulse. The scattered radiation interferes with the incident radiation and produces a beatwave. If the beatwave frequency is close to

the plasma frequency, the ponderomotive force associated with the beatwave excites a plasma wave which is equivalent to a phase grating leading to the Bragg reflection of the laser pulse. It reinforces the beatwave and thus the plasma wave. Finally, this feedback loop results in an exponential growth of the scattered radiation.

The amplification mechanism can also be explained from a microscopic picture. A single electron emits dipole radiation while it is oscillating in the plasma. When a laser pulse propagates in a homogeneous plasma, neglecting the magnetic field, electrons oscillate in the electric field of the laser pulse transversely with the velocity $\vec{v} = -q\vec{E}/m\omega$ and form a transverse current $\partial J = \partial n_e q\vec{v}$. The radiated dipole field from the electrons are incoherent for some directions and cancel out. However, if the plasma density is modulated in a way that Eq. (2.50) is approximately satisfied, in which the excited waves are electromagnetic wave and plasma wave, the emission from single electron dipoles superimposes constructively. Backscattering is preferably used for amplification since it has the highest growth rate, and the counter propagating pump wave can continually deliver energy to the probe.

3.1.2 Coupled equations for the Raman three-wave interaction

Knowing the amplification mechanism, the coupled equations describing the three-wave interaction of the Raman instability will be derived. We address the case of a weak scattered field and consider a transverse incident pump wave with vector potential A_0 scattered into A_1 by a small electron density perturbation δn.

The current density $\vec{J}$ can be separated into a transverse part and a longitudinal part. The transverse current $\vec{J_t} = n_e q\vec{v}_{os}$ is associated with the light wave, while the longitudinal current $\vec{J_l}$ is related to the Poisson's equation Eq. (2.10) via the space charge force, which is the reaction to the ponderomotive force, and satisfies the equation for charge conservation $\partial\rho/\partial t + \nabla\cdot\vec{J_l} = 0$ (a variation of Eq.(2.19)). Combining these two equations, we have:

$$\nabla \cdot \left(\frac{\nabla \partial \phi}{\partial t} + \frac{\vec{J_l}}{\varepsilon_0} \right) = 0. \tag{3.1}$$

Substituting Eq. (3.1) into Eq. (2.11), we obtain the relation between the transverse current $\vec{J_t}$ and the light wave vector potential $\vec{A}$:

$$\left(\frac{\partial^2}{\partial t^2} - c^2 \nabla^2 \right) \vec{A} = \frac{\vec{J_t}}{\varepsilon_0}. \tag{3.2}$$

Substituting the electron oscillatory velocity into the transverse current, $\vec{J_t} = -q^2 n_e \vec{A}/m$. Then, substituting $\vec{J_t}$ into Eq. (3.2) gives a Klein-Gordon type equation for the vector potential:

$$\left(\frac{\partial^2}{\partial t^2} - c^2 \nabla^2 + \omega_p^2 \frac{n_e}{n_0} \right) \vec{A} = 0. \tag{3.3}$$

The radiation wave amplitude is decomposed into pump and probe, the plasma density into an uniform background and a density fluctuation:

$$\vec{A} = \vec{A}_0 + \vec{A}_1, \quad n_e = n_0 + \delta n. \tag{3.4}$$

First consider the case where A_1 and δn are small perturbations, $|A_1| \ll |A_0|$ and $|\delta n| \ll n_0$. Substituting Eq. (3.4) into Eq. (3.3), we obtain the wave equations for the pump and the probe waves. The r.h.s of Eq. (3.5) is then second order in the perturbation and can be neglected.

$$\left(\frac{\partial^2}{\partial t^2} - c^2 \nabla^2 + \omega_p^2 \right) \vec{A}_0 = -\omega_p^2 \frac{\delta n}{n_0} \vec{A}_1 \approx 0, \tag{3.5}$$

$$\left(\frac{\partial^2}{\partial t^2} - c^2 \nabla^2 + \omega_p^2 \right) \vec{A}_1 = -\omega_p^2 \frac{\delta n}{n_0} \vec{A}_0. \tag{3.6}$$

Now we derive the equation to characterise the evolution of the density perturbations of the longitudinal plasma wave. First, we substitute $n_e = n_0 + \delta n$ into the continuity equation Eq.(2.19) and the second order term $\propto \delta n v_l$ is neglected. Then

taking the time derivative of it and combining it with the equation of motion Eq. (2.20) we have

$$\frac{\partial^2 \delta n}{\partial t^2} = -n_0 \frac{q}{m} \nabla \cdot (\vec{E} + \vec{v} \times \vec{B}). \tag{3.7}$$

The electron velocity can be split into longitudinal and transverse parts, i.e. $\vec{v} = \vec{v}_t + \vec{v}_l$. Using $\vec{A}$ and ϕ to express $\vec{B}$ and $\vec{E}$, the longitudinal component can be derived from Eq. (2.20).

$$\frac{d\vec{v}_l}{dt} = -\frac{q^2}{m^2}\vec{A} \cdot \nabla \vec{A} + \frac{q}{m}\vec{E}_t = -\frac{1}{2}\nabla \left(\frac{q^2 \vec{A}^2}{m^2} \right) + \frac{q}{m}\vec{E}_l \tag{3.8}$$

In Eq. (3.8), the first term on the r. h. s. $(1/2)\nabla(q^2\vec{A}^2/m^2)$ describes the ponderomotive force. Substituting $\vec{A} = \vec{A}_0 + \vec{A}_1$ into this term and neglecting the zero and the second order terms, it can be simplified as follows:

$$\frac{q^2}{2m^2}\nabla(\vec{A}_0 + \vec{A}_1)^2 \approx \frac{q^2}{m^2}\nabla(\vec{A}_0 \vec{A}_1).$$

Finally, combining Eq. (3.7) and (3.8), the following equation is derived, which describes the generation of an electron density fluctuation by variation of the intensity of the electromagnetic field.

$$\left(\frac{\partial^2}{\partial t^2} + \omega_p^2 \right) \frac{\delta n}{n_0} = \frac{q^2}{m^2} \nabla^2 (\vec{A}_0 \vec{A}_1) \tag{3.9}$$

So now we have the three-wave equations Eq. (3.5), (3.6) and (3.9) to describe the Raman scattering in plasma.

3.1.3 Slowly-varying envelope approximation

Reduction of the second order equations to first order envelope equations is a simplification to help find solutions, even if the probe amplitude is not small compared to that of the pump. Assuming the propagation is along the z direction, and applying the

slowly-varying envelope approximation, the vector potential of the laser pulses and the density modulations can be written as

$$\begin{aligned} \vec{A}_{0,1} &= \vec{u}\left(\frac{mc}{2q}\right) a_{0,1}(z,t)e^{i\varphi_{0,1}} + c.c., \\ \frac{\delta n}{n_0} &= \frac{ne^{-i\Delta\varphi}}{2} + c.c., \end{aligned} \tag{3.10}$$

where $\varphi_{0,1} = \omega_{0,1}t \pm k_{0,1}z$, $\Delta\varphi = \varphi_0 - \varphi_1 = \Delta\omega t + \Delta k z$ and $\Delta\omega = \omega_0 - \omega_1$, $\Delta k = k_0 + k_1$. Here $\vec{u}$ is a unit vector (for linear polarisation $\vec{u} = \vec{u}_x$ and for circular polarisation $\vec{u} = (\vec{u}_x + i\vec{u}_y)/\sqrt{2}$) and $c.c.$ denotes the complex conjugate of the preceding expression.

With the assumption that the variation of the envelopes with time and position is much slower than that of the corresponding phases, the second derivative of $\vec{A}_0$ with respect to time is

$$\frac{\partial^2 \vec{A}_0}{\partial t^2} \approx \vec{u}\left(\frac{mc}{2q}\right) e^{i\varphi}\left(2i\omega_0\frac{\partial a_0}{\partial t} - \omega_0^2 a_0\right) + c.c., \tag{3.11}$$

and with respect to position is

$$\nabla^2 \vec{A}_0 \approx \vec{u}\left(\frac{mc}{2q}\right) e^{i\varphi}\left(2ik_0\frac{\partial a_0}{\partial z} - k_0^2 a_0\right) + c.c., \tag{3.12}$$

Similar expressions apply for $\vec{A}_1$. The second time derivative of $\delta n/n_0$ is

$$\frac{\partial^2\left(\frac{\delta n}{n_0}\right)}{\partial t^2} \approx \frac{1}{2}e^{-i\Delta\varphi}\left(-2i\Delta\omega\frac{\partial n}{\partial t} - \Delta\omega^2 n\right) + c.c.. \tag{3.13}$$

After substituting these expressions into the coupled equations Eq. (3.3), choosing $\Delta\omega = \omega_p$ and applying the approximations $ck_0 \approx ck_1 \approx \omega_1 \approx \omega_0$, finally we have the reduced three-wave equations

$$\left(\frac{\partial}{\partial t} - c\frac{\partial}{\partial z}\right) a_0 = i\frac{\omega_p^2}{4\omega_0} n^* a_1, \tag{3.14}$$

$$\left(\frac{\partial}{\partial t}+c\frac{\partial}{\partial z}\right)a_1 = i\frac{\omega_p^2}{4\omega_0}na_0, \tag{3.15}$$

$$\frac{\partial n}{\partial t} = -i\frac{\omega_0^2}{\omega_p}a_0^* a_1, \tag{3.16}$$

where the asterisk denotes the complex conjugate.

3.2 Raman amplification in different regimes

3.2.1 Raman amplification in the linear regime

- Growth rate

To derive the growth rate of the RBS instability, we first write the wave amplitude $\vec{A} = \vec{A_L} + \delta\vec{A}$, where $\vec{A_L}$ is the pump pulse field amplitude and $\delta\vec{A}$ is the scattered field amplitude. Substitute it and $n_e = n_0 + \delta n$ into Eq. (3.6) and (3.9). Then, Fourier transform them to the frequency domain and choose $\vec{A_L} = \vec{A_0}\cos(\omega_0 t - \vec{k}_0 x)$ (where ω_0 and $\vec{k}_0$ satisfy the plasma dispersion relation $D_\perp(\vec{k}_0, \omega_0) = \omega_0^2 - c^2\vec{k}_0^2 - \omega_p^2 = 0$). Finally, the dispersion relation for the frequency of the density perturbation can be expressed as:

$$D_\parallel(\omega) = \omega^2 - \omega_{ek}^2 = \frac{(\vec{k}\omega_p v_{os})^2}{4}\left(\frac{1}{D_+}+\frac{1}{D_-}\right), \tag{3.17}$$

where ω_{ek} is the electron Bohm-Gross frequency [43], $\vec{k}$ is the wave vector of the ponderomotive force, thus of the plasma wave. v_{os} is the electron oscillatory velocity amplitude, and $D_\pm = D_\perp(k_\pm, \omega_\pm)$ correspond to waves with up and down shifted frequencies ($\omega_\pm = \omega_0 \pm \omega$, $\vec{k}_\pm = \vec{k}_0 \pm \vec{k}$). Considering the case when the Stokes wave can propagate, i.e. D_- is small and $1/D_+$can be neglected, Eq. (3.17) becomes

$$D_\parallel(\omega)D_\perp(k_-, \omega_-) = (\omega^2 - \omega_{ek}^2)(\omega_-^2 - c^2\vec{k}_-^2 - \omega_p^2) = \frac{(\vec{k}\omega_p v_{os})^2}{4}. \tag{3.18}$$

Now introducing a small imaginary component γ to ω as $\omega = \omega_p + i\gamma$, substituting this expression into Eq. (3.18) and solving the equation by separating the real and imaginary parts, the maximum linear growth rate at the plasma resonance can be obtained:

$$\gamma_0 = \frac{\vec{k}a_0 c}{4} \frac{\omega_p}{\sqrt{\omega_{ek}(\omega_0 - \omega_{ek})}}. \tag{3.19}$$

The growth rate is highest for Raman backscattering. The wave number k for backscattering is given by [26]:

$$k = k_0 + \frac{\omega_0}{c}\left(1 - \frac{2\omega_p}{\omega_0}\right)^{1/2} \approx 2k_0. \tag{3.20}$$

Typically in experiments, $\omega_0 \gg \omega_{ek}$ and $k_0 \approx \omega_0/c$. With linearly polarised laser pulses, the growth rate for Raman backscattering is

$$\gamma_0 \approx \frac{a_0}{2}\sqrt{\omega_0 \omega_p}. \tag{3.21}$$

Similarly, the growth rate for the Raman forward scattering for linear laser polarisation is

$$\gamma_0 \approx \frac{a_0 \omega_p^2}{2\sqrt{2}\omega_0}. \tag{3.22}$$

- The accepted resonance detuning for Raman amplification

In the previous section, the growth rate has been derived with the assumption that the laser beams are monochromatic. However, experiments are carried out using laser beams with a finite bandwidth. As a result, the Raman scattering process becomes more complicated than the monochromatic case. The gain bandwidth of Raman amplification, i.e. the spectral width over which we can expect growth is given by $2\gamma_0$. For detuning within the bandwidth $\pm\gamma_0$, the system exhibits an instability with exponential growth at the rate

$$\gamma(\Delta) = \sqrt{\gamma_0^2 - \frac{\Delta^2}{4}}. \tag{3.23}$$

- Raman amplification with a monochromatic pump pulse

When energy transfer from the pump to the probe is small and pump depletion is negligible i.e. $a_0 \simeq$ const, we are in the Raman linear regime. In this regime, the collective plasma oscillations govern the electron dynamics. If the resonance condition for RBS is satisfied, the probe pulse can be quickly amplified with an exponential growth $a_1 e^{\gamma_0 t}$, which is an approximation of the Bessel functions that solve Eqs. (3.15) and (3.16) for a constant a_0.

When using a monochromatic pump pulse, several disadvantages are associated with this regime. First, the resonance conditions have to be strictly satisfied due to the narrow gain bandwidth $\Delta\gamma = 2\gamma_0$. Second, because the plasma wave persists after the interaction has taken place, the long pump pulse can still be backscattered and add up at the back of the probe pulse. This leads to temporal stretching of the probe and, as a result, limits the utility of this scheme for the amplification of short laser pulses. Furthermore, although the gain can be significant, it can be diminished by several concurrent phenomena, such as spontaneous Raman backscattering and Raman forward scattering, which lead to pump depletion. However, as will be discussed in the following sections, different possibilities and regimes exist to amplify short laser pulses with Raman amplification in plasma.

- Raman amplification with a chirped pump pulse

Raman amplification of laser pulses in plasma has been studied by different research groups using different approaches. One common feature of all of these experiments is that the long pump pulse is temporally stretched by frequency chirping, sometimes directly from the CPA laser chain without compression and sometimes with partial compression. The impact of the pump frequency chirp on the Raman amplification in

the linear regime will be explored in this section.

The chirp-induced frequency detuning will limit the duration of interaction between the resonant frequencies of the pump and the probe pulses, as a result limiting the amplification efficiency. When the pump pulse has a linear frequency chirp such that a range of frequencies $\Delta\omega$ are contained in the pulse duration ΔT, the chirp rate is defined as $\alpha = \sqrt{\Delta\omega^2 - 1/\Delta T^2}/\Delta T$. If the pulse is far from Fourier-limited, $\alpha = \Delta\omega/\Delta T$. The phase of the pump pulse can be written as follows:

$$\varphi_0 = \omega_0(t + z/c) + \varphi_{ch}, \tag{3.24}$$

where $\varphi_{ch} = \alpha(t + z/c)^2/2$. The chirp determines the longitudinal position at which each frequency component of the probe will be amplified. In other words, it has the effects of distributing the gain in both frequency and position. To quantify the effect of frequency detuning, the interval for the plasma wave to grow is given by the time when the local detuning of the pump and probe wave remains within the resonance bandwidth. The amplification of the plasma wave amplitude is thus given by the integral of the growth rate Eq. (3.23) during this time: $\int dt\gamma(\Delta(t)) = \pi\gamma_0^2/2\alpha$. As a result, the RBS gain with a chirped pump pulse is presented in Eq. (3.25), which can be used to calculate the amplification of each probe spectral component.

$$G = e^{\pi\gamma_0^2/2\alpha}. \tag{3.25}$$

This result is of great importance, as for the case of a monochromatic pump the gain is exponentially dependent on the interaction duration (or propagation distance), while with a frequency chirped pump pulse, the gain is independent of the total interaction length.

Apart from limiting the gain, the pump frequency chirp also plays a role in the probe pulse evolution. The backscattered radiation superposes coherently just behind the probe, but dephases at longer distances. Analytical theory shows that the probe

pulse duration stretches at the beginning and then shrinks at a rate inversely proportional to the interaction time t until the original length, which contrasts with the continuing stretching of the probe profile expected for a monochromatic pump. Moreover, the scattered fields effectively carry out a Fourier transform of the probe "on the fly", which leads to self-similar growth and an overall amplitude increase proportional to t. The probe evolution shows the characteristics of superradiant scaling which are usually associated with the nonlinear Raman and Compton regimes. In addition, a chirped pump pulse can also suppress the unwanted spontaneous scattering by distributing the gain in both frequency and position [31, 73, 74].

Fig. 3.1 shows the longitudinal profile of the probe pulse at different times using a chirped pump pulse. In this plot, the probe pulse is moving to the negative z direction and $\zeta = z/c$. It can be seen that with time the probe profile gets modulated in the form of a multispiked wave train. The probe duration increases at the earlier stage of interaction and then compresses.

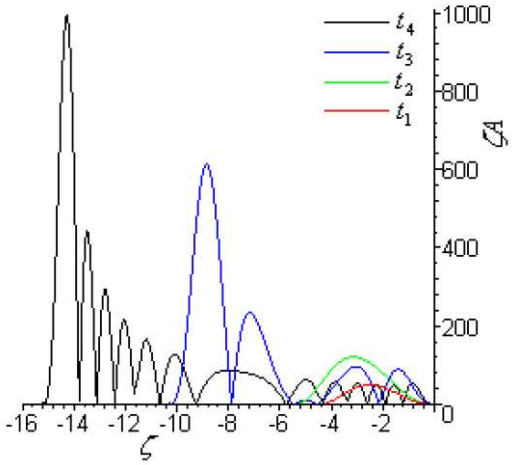

Figure 3.1: Profile of the probe pulse vector potential envelope at different times with chirped pump pulse.

Therefore, if we want to amplify a short probe pulse, we can either use a chirped pump pulse to match the resonant conditions for every probe frequency and get each frequency amplified by a different region of the pump, or make use of the nonlinear regimes where the probe pulse is amplified and compressed at the same time. The

latter case of nonlinear regimes will be discussed in the following sections.

3.2.2 Raman pump depletion regime

In the linear stage of Raman backscattering, the amplitude of the pump pulse is approximately constant. With sufficiently high amplitude of the probe pulse, i.e. $a_1 \sim (\omega_p/4\omega_0)^{3/2}$, substantial energy is transferred from the pump to the probe. The pump will be depleted by the front of the probe pulse, and therefore the growth at the rear is suppressed. Due to Burnham-Chiao ringing [75], energy can transfer both ways between the pump and probe and the probe evolves into a series of short pulses. Thus, the amplification process reaches the nonlinear stage, i.e. the Raman pump depletion regime [30].

Applying the three-wave equations Eq. (3.14), (3.15) and (3.16) to the description of Raman amplification of a short probe pulse in the nonlinear regime, we will find a self-similar solution of a sine-Gordon type of equation [76] for the envelopes of the scattered wave, the pump wave and the plasma density. Such a solution for the scattered wave firstly shows an amplitude increase from its initial value and then oscillates with a period of $1/\gamma_0^2$. Fig. 3.2 shows the evolution of the probe pulse's envelope at different times in the pump depletion regime.

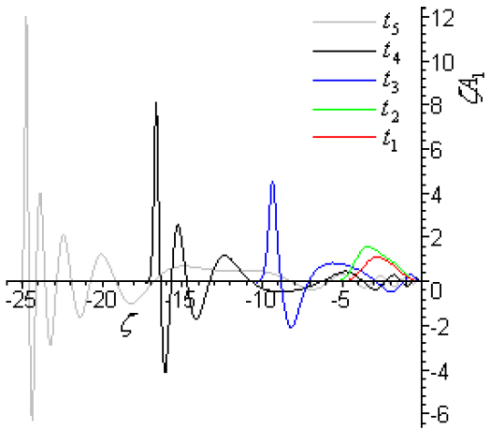

Figure 3.2: Evolution of the probe pulse vector potential envelope at different times in the pump depletion regime.

To understand the pump depletion regime, we need to look at the interaction process in detail. At the beginning of the amplification process, the probe pulse absorbs almost all the energy of the pump pulse it encounters. When the pump is depleted, the energy flow reverses and the probe pulse is backscattered into the pump and depleted as well. The zeros of the pump and probe pulses take turns. Each time one pulse is depleted the carrier wave shifts its phase by π and the energy transfer reverses. Consequentially the output probe becomes a pulse train which is the so called "π-pulse", with the first spike containing about 50% of its energy. The peak of the amplified probe pulse grows proportional to the interaction time and it approaches the pulse front with superluminal speed. The pulse duration of the first spike shrinks and is inversely proportional to the interaction time. This regime is expected to be accessed when the pump pulse has a rather low intensity $I_0 = 10^{12} \sim 10^{15}$ Wcm^{-2} and the plasma density is high enough $n_e/n_{crit} = 0.01 \sim 0.1$.

For the amplified probe pulse, a non-negligible fraction of the pump pulse energy is absorbed in the secondary peaks of the pulse train. To overcome this problem, theoretical results for a monochromatic pump pulse with normalised vector potential larger than the wave breaking limit ($a_{br} \approx 1/4(\omega_p/\omega)^{3/2}$) show that the plasma wave breaks close to the leading maximum of the amplified pulse. This will prevent the reverse scattering from the probe to the pump pulse, so that all the secondary π-pulses can be suppressed [30, 73].

The parameters we used in the experiment are far from the requirements to reach the pump depletion regime. Instead, with the Raman amplification in the linear stage, when the ponderomotive force associated with the beatwave exceeds the electrostatic force of the plasma wave and the Raman backscattering instability evolves into the nonlinear regime.

3.2.3 Compton regime - superradiant amplification

The Compton regime of laser amplification in plasma is the direct analogue of the free-electron laser. Unlike in the case of the Raman instability where the electrons oscillate at the plasma frequency, in the Compton regime, the ponderomotive force of the beat-wave acting on a plasma electron is larger than the electrostatic force and the bunching of the electrons is due to the dynamics of the single electrons rather than to the collective motion of a plasma wave. Consequently, the frequency matching condition for Raman scattering need not be satisfied precisely. Due to this advantage, the Compton regime has aroused great interest and has been investigated both theoretically [16] and experimentally [35].

The threshold condition for entering the Compton regime is derived from its definition that the ponderomotive force is larger than the electrostatic force (i.e. $F_{pond} \geq F_{stat}$). Assuming a single electron is trapped in a well of the ponderomotive force potential, after solving the equation of motion i.e. $m\partial^2 z/\partial t^2 = F_{pond}$ and changing to the co-moving frame, the bounce frequency is derived: $\omega_b = \sqrt{a_0 a_1}(\omega_0 + \omega_1) \approx 2\omega_0\sqrt{a_0 a_1}$ [77]. Therefore, the electron oscillates in the ponderomotive potential bucket if

$$4\omega_0^2 a_0 a_1 \geq \omega_p^2. \tag{3.26}$$

It is worth noting again that the threshold just indicates an estimate of the transition between the two regimes. Features of the Compton regime can appear both below or above the threshold.

- Plasma electron dynamics in the Compton regime

When entering the Compton regime with initial amplification in the linear regime, the plasma electron dynamics will change from the collective motion of the plasma wave to the electron oscillations in the ponderomotive potential. The evolution from

the stimulated Raman scattering into the Compton scattering has been experimentally observed through the wave breaking phenomenon, using spontaneous scattering from a single laser beam in a plasma [78]. Here we will briefly review the transition process and the electron oscillation in the ponderomotive potential.

First, the electrons are evenly distributed in the longitudinal direction before the arrival of the laser pulses. Then, a beatwave is generated by the interference of the two laser beams and, as a window, selects a slab of plasma electrons. When the ponderomotive potential of the beatwave builds up, electrons with less energy than the crest of the potential structure will get trapped and start oscillating in the potential well. On the other hand, electrons with more energy can surmount the crest and pass on to the adjacent well. Assuming the plasma density remains the same, the stronger the beatwave becomes, the more electrons will be trapped. When the motion of most electrons is dominated by the ponderomotive potential, the Raman interaction evolves into the Compton regime. In the meantime, the nonlinear wave-particle interaction (such as the electron trapping) will cause modification of the electron velocity distribution function and downshift the resonant frequency [25, 79].

Looking at the motion of trapped electrons in the time domain can enable us to see how the independent electrons get bunched by the oscillation in the ponderomotive potential. Once the electrons are trapped in the potential well, they will start a synchrotron oscillation with period $T_b = 2\pi/\omega_b$. At $T_b/4$, the electrons get bunched in space for the first time at one edge of the well. The bunching is a consequence of their small velocity near the return points, which allows the late electrons to catch up with the early ones. As the electron distribution becomes discrete, a density grating is formed. At the half oscillation cycle (i.e. $T_b/2$), the electron dispersion becomes roughly uniform again, which means the density grating degrades. At $3T_b/4$, the electrons bunch again at the opposite edge of the potential well and form another density grating with a π shift in phase. At the end of this cycle, electrons go back to their initial positions and evenly distribute again. In this process, similar to the Raman instability,

the electron density perturbations reflect the laser beam like an optical grating. Details of the evolution of the laser pulses will be discussed in the following section.

- Evolution of laser pulses in the Compton regime

In the Compton regime, laser pulses dominate the dynamics of the electrons and in turn react to the effects of electron motion. This self-consistent process is the reason why the Compton regime is ideal for laser amplification.

As discussed previously, at $T_b/4$ an electron density grating is formed, photons in the pump pulse are backscattered into the probe and the momentum difference is transferred into the plasma. The ratio of the energy gained by the probe pulse to the momentum transferred to the plasma is $\Delta U/\Delta P = -\omega_0/2k_0$ [16]. Hence, as the probe pulse gets amplified, in the meantime, an efficient and localised momentum transfer is achieved for the plasma.

After half an oscillation cycle of the trapped electrons from $T_b/4$ to $3T_b/4$, the density grating formed with a π phase shift will scatter the probe back into the pump. The direction of the energy flow is determined by the position of the electron density peak within the ponderomotive potential well, in other words, it is determined by the phase relation between the two laser waves at the position of the scattering electrons. To prevent the probe pulse attenuation, the ideal probe pulse duration is shorter than $T_b/2$, so that no energy can be transferred back to the pump pulse. Otherwise, the energy at the rear part of the probe will be diminished and as a result the pulse duration will be constricted to $T_b/2 = \pi/\omega_b$ ultimately while its front gets continuously amplified. In both cases, with the probe pulse getting more intense, the bounce frequency increases and therefore the pulse duration will become even shorter.

As a consequence of the pulse duration shrinking, its bandwidth has to increase. An intuitive way to understand the bandwidth broadening is to look at the velocity spread of the electrons when they are bunched at the edge of the potential well. When a photon is backscattered by an electron, its frequency is Doppler shifted due to the

electron velocity. As a feedback loop, with the increase of the laser pulse intensity, electrons with larger velocity spread will get trapped in the deeper potential well which can provide a broader laser bandwidth.

A simple qualitative estimate of the pulse evolution is given by

$$|a_1| \approx \frac{4\omega_p}{3\pi\omega_0} k_p z |a_0|, \tag{3.27}$$

from which we can see that the intensity of the spike grows proportionally to $(n_e z)^2$ i.e. the total number of plasma electrons encountered by the pulse. This equation shows the feature of superradiance according to the classic definition by Dicke [80]. Therefore the Compton regime is also called the superradiant regime.

- Analogy to free-electron lasers

The physics of free-electron lasers (FEL) [81, 82] has been investigated intensively, both experimentally and theoretically. Raman amplification of laser pulses in plasma shares a similar mechanism with the FEL, perticularly the laser amplification in Compton regime with the FEL in superidiant Compton regime [83] . Reviewing the principles of FEL can help us to better understand the theory of the laser amplification in plasma.

A FEL consists of a periodic magnetostatic structure called undulator or wiggler, which generates a spatially alternating magnetic field. A relativistic electron beam is sent through this structure and the Lorentz force makes the electrons oscillate and radiate. As the electrons move at a velocity close to the speed of light, the radiation is confined to the forward direction, as shown in Fig. 3.3. When the electrons are uniformly distributed, the radiation superimposes incoherently. The ponderomotive potential of the undulator field and the radiation field can give rise to bunching of the electrons, which increases their coherence and thus leads to an amplification of the radiation field. The bunching can be described by the bunching parameter which ranges

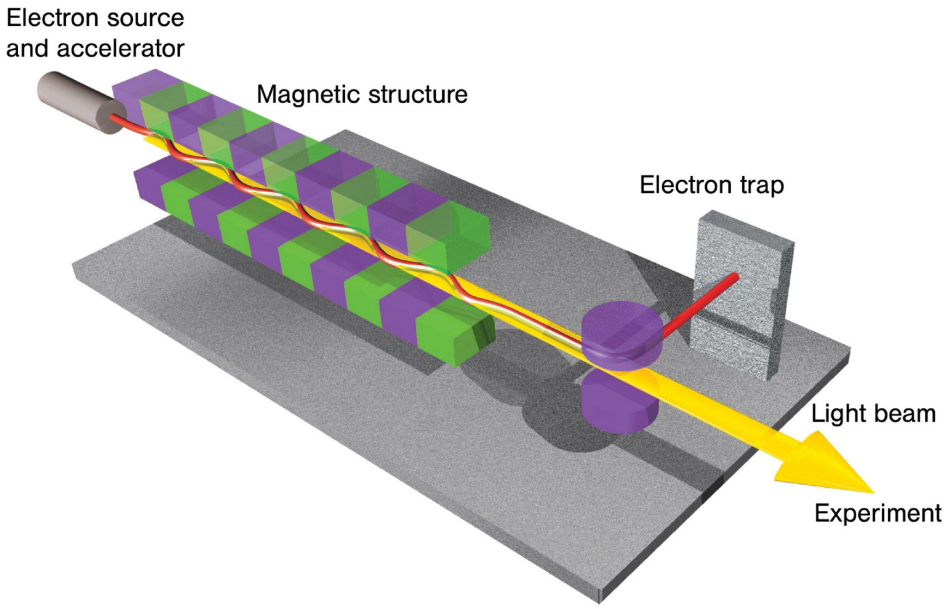

Figure 3.3: Schematic of FEL (`http://hasylab.desy.de/facilities/sr_and_fel_basics/fel_basics/index_eng.html`).

from 0 to 1, where 0 indicates uniformly distributed electrons radiating incoherently and 1 indicates perfectly bunched electrons radiating coherently. A better bunched electron beam will generate more coherent radiation and stronger radiation with larger ponderomotive potential will improve the electron bunching. Such a feedback loop can result in exponential growth in the small signal regime.

The similarity between FEL and laser amplification in plasma can become more apparent by a Lorentz transformation to the reference frame of the relativistic electron beam. The electron beam in the FEL corresponds to the plasma in the laser amplifier, while the FEL undulator magnetostatic field is transformed into the electromagnetic pump wave propagating in the opposite direction.

In the FEL Raman regime, electrons experience collective motion dominated by the electrostatic force which is equivalent to the laser amplification in the Raman regime. And the self-amplification of spontaneous emission (SASE) [84] is a mode of FEL operation which has no initial radiation field to seed the emission and the lasing starts up from the random microbunching on the electron beam. It is similar to the spontaneous

Raman scattering which needs to have a considerably large gain to achieve a notable output. In the superradiant Compton regime of the FEL described by Bonifacio et al. [83, 85, 86] the common ponderomotive force of the laser pulse and the wiggler field is larger than the electrostatic force between the electrons, hence the electrons are trapped and get bunched efficiently and results as supperradiant gain, which is exactly equivalent to the Compton regime of the laser amplification in plasma, therefore it is also known as the supperradiant regime.

3.2.4 Distinction between Raman linear regime and Compton regime

Different amplification regimes have been discussed individually and it can be seen that the Compton regime and the Raman amplification with a chirped pump pulse, although with different principles, experimentally both exhibit laser amplitude growth and pulse shortening. Being able to distinguish between these two regimes is a must in the analysis of experimental results.

First of all, it should be noted that the Compton regime may not be reached immediately. Amplification can start in the Raman regime and then evolve to the Compton regime when the probe amplitude grows sufficiently large to satisfy the threshold condition. If the transition from Raman to Compton regime occurs gradually, it will be difficult to define a clear amplification regime. Section 3.2.5 will focus on the transition between the two regimes.

Secondly, we should be aware that although the two amplification regimes can be clearly distinguished theoretically, it is not easy to determine from the experiment whether the Compton regime is reached. The measurable parameters are: the energy, spectrum and pulse duration of the probe pulse. In the transition, the intensity gain goes from exponential to quadratic which is observed by a slower saturation. Combined with the change in pulse duration and profile, it's nearly impossible to judge in which regime the amplification is. The most convincing criteria would be the strong spectral broadening combined with the pulse shortening.

3.2.5 Transition from Raman to Compton regime

The aim of this work is to realise the transition from Raman to Compton regime of short laser amplification in plasma. As stated previously, when the bounce frequency ω_b is greater than the plasma frequency ω_p, the Compton regime will be reached. In this section, we investigate the transition between Raman scattering, where the electron behaviour is dominated by collective plasma wave effects and the Compton regime, where the electron behaviour is determined by single particle dynamics. In order to do so, Cairns sets up a simple model of electron dynamics to look at electron displacements ξ with parameter $b = \omega_b^2/\omega_p^2$ and $\Omega = (\omega_0 - \omega_1)/\omega_p$ [87]. Normalising time and distances to $1/\omega_p$ and $1/k$. Although that model is just an approximation which is only valid for small amplitude waves, it can give us an idea of how the two regimes merge.

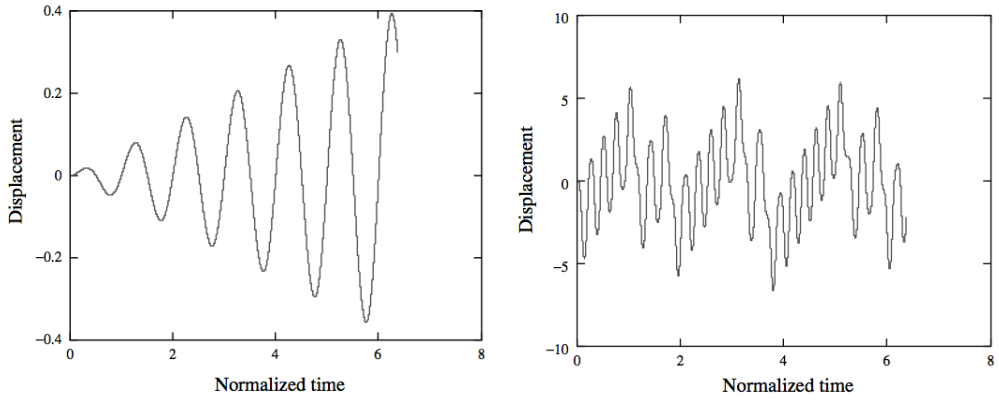

(a) (b)

Figure 3.4: Displacement as a function of time with $\Omega = 1$ and (a) $b = 0.02$, (b) $b = 50$.

Fig. 3.4(a) and 3.4(b) show the displacement as a function of time with $b = 0.02$ and $b = 50$ respectively when $\Omega = 1$ i.e. we are in resonance. With small and large b values, respectively, Fig. 3.4(a) depicts the case of Raman scattering, while Fig. 3.4(b) presents the solution for the Compton regime, where we can see that electron motion is governed by the much faster time scale of the oscillations within the potential wells and there is an occasional jump when the particle escapes from one potential well and gets trapped by the one behind. Similar features are found when $\Omega \neq 1$, since in the

Compton regime the natural frequency is not so important.

However, to see what happens in the transition region between them, the situations when $b = 0.5$ and $b = 1.5$ are also studied, as shown in Fig. 3.5(a) and 3.5(b) respectively. In Fig. 3.5(a) no obvious sign of the bounce frequency is observed. For the first few period the growth is linear, however, when the wave amplitude becomes sufficient to carry the particle to a distance comparable to the spatial period of the driving force the linear growth will saturate. When $b = 1.5$, as shown in Fig. 3.5(b), no clear sign of trapping is seen but the resonant particle oscillation is disturbed. When b goes up to 5, clear indication of trapping can be seen at the starting point for most of the cases.

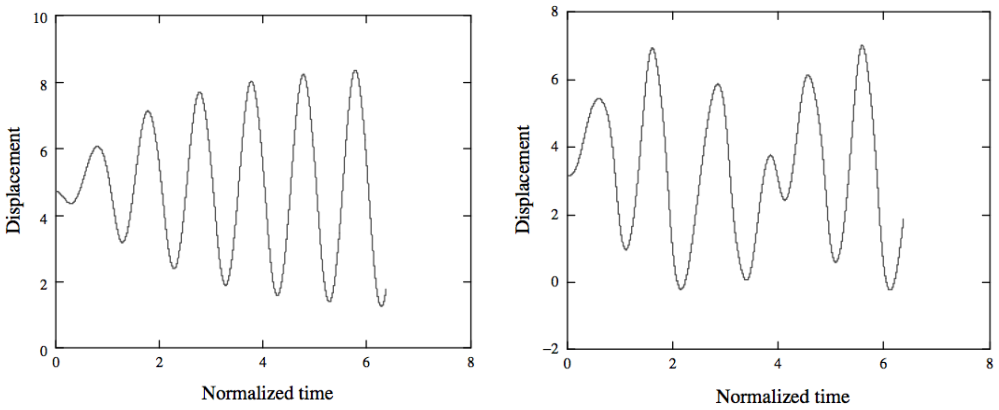

(a) (b)

Figure 3.5: Displacement as a function of time with $\Omega = 1$ and (a) $b = 0.5$, (b) $b = 1.5$.

For the extreme cases when b is either small or large, the particle response is well understood. However, in the transition regime, when b is around 1, it is still not clear how the transition is realised, i.e. whether Compton regime is entered smoothly or if a barrier has to be overcome. Further investigation will rely on the more complicated PIC simulation.

3.3 Limitation of the laser energy gain

Just as the output intensities of the CPA scheme are limited by the size and damage threshold of the optics, the Raman amplification scheme has its own limitations. Var-

ious instabilities can develop during the interaction between the intense laser pulses and plasmas. The fastest growing instability will set the limitation of the amplification [74]. The probe pulse must be directed out of the plasma before it degrades due to any of the instabilities.

3.3.1 Energy flow between the three waves

When two laser pulses collide in plasma, they may exchange photons. The direction of the energy flow between the pulses during this process is governed by the Manley-Rowe relations [88]. Those relations were originally derived to describe the average power flow in inductors and capacitors. Applied to the Raman process, the Manley-Rowe relations indicate that the energy flows from the higher frequency wave to the lower frequency wave, and the fraction of pump energy that is transferred to the plasma wave is the ratio of the plasma frequency to the laser frequency. For the parameters used in this experiment, this ratio is about 0.02 which means almost all the energy of the pump can be consumed by the probe. However, until now no experiment with energy transfer efficiency (i.e. the ratio between the laser transferred energy and the total energy) larger than 10% has been reported. Here, we will study the possible mechanisms which could limit the efficiency of this scheme.

3.3.2 Limitation mechanisms

Theoretical studies suggest a number of mechanisms may limit the efficiency of the Raman backscattering, including Raman forward scattering, modulational instabilities, thermal effects, plasma wave breaking, resonance detuning, the amplification of precursors and etc. Here, we will discuss some likely limiting effects of the experiment presented in this thesis.

- Raman forward scattering

Traditional Raman amplification was plagued by parasitic Raman forward scattering (RFS) [89] of noise, which has a higher growth rate than the backward scattering in gases, liquids, and solids. In plasma, the growth of Raman backscattering is faster than forward scattering, however, this problem still exists because the forward scattered signal propagates along with the parent laser and therefore has more time to grow which is known as a convective instability.

A way of suppressing the parasitic RFS of the pump pulse is to detune the resonance appropriately, for example by using a chirped pulse or a frequency detuned plasma [90]. Therefore, in this experiment, seeding the RFS of the pump pulse with an intense probe can be tolerated in the Raman backscattering amplification process without being significantly amplified.

- Modulational instability

Modulational instability [91, 92] arises as the electrons are accelerated by the intense probe pulse to relativistic velocities. This causes a nonlinear refractive index for the plasma, which will lead to transverse self-focusing and longitudinal self-phase-modulation. For an amplified probe with normalised vector potential $a_1$and frequency ω_1, the growth rate for the modulational instability γ_m in a plasma with frequency ω_p is:

$$\gamma_m = \frac{\omega_p^2}{2\omega_1} a_1^2. \tag{3.28}$$

Using our experimental parameters (plasma density: 1×10^{18} cm^{-3}, probe beam energy: 1 mJ, pulse duration: 60 fs, focal spot size: 60 μm, wave length: 825 nm), the growth rate for the modulational instability is estimated $\gamma_m = 4.67 \times 10^7$ s^{-1} which is 4 orders of magnitude smaller than the Raman backscattering instability, therefore it is not important in our case.

- Thermal effects

Thermal effects on RBS in plasma at finite temperature have been widely studied experimentally, analytically, and numerically [44]. The main consideration includes Landau damping of the resonant Langmuir wave, inverse bremsstrahlung of the pump and probe laser pulses and plasma heating through these effects.

For plasmas at low temperature (as for the case in this experiment $T_e \sim 5eV$ initially), the collisional damping of the plasma wave and the laser radiation absorption through inverse bremsstrahlung may have a significant impact on RBS. Since the electron-ion collision rate decreases very quickly with increasing temperature, the pump energy transfer efficiency can be improved by preheating the plasma in order to diminish the wave damping and minimise the laser absorption.

Moreover, the inverse bremsstrahlung heating can also build up a thermal chirp of the resonance frequency over time by the Bohm-Gross shift due to the different interaction time between the plasma and the long pump pulse. The shift in plasma resonance may cause a reduction of the Raman gain with a monochromatic pump. However, in the scheme of using a chirped pump pulse, it can be used to compensate for the thermal chirp.

For high temperature plasmas, Landau damping is significant, which could suppress the plasma wave excitation and therefore restrain Raman amplification. It was found by numerical simulations that Landau damping could delay the onset of pump depletion and weaken the secondary spikes of the amplified laser pulses [93].

The effects of a spatially and temporally varying plasma temperature on Raman amplification are very complex and subtly depend on the plasma density, temperature and laser parameters. Therefore they will not be addressed quantitatively here.

- Plasma wave breaking

Plasma wave breaking occurs when the oscillation velocity of electrons in the plasma wave is approaching the phase velocity of the plasma wave. Many more electrons can

resonantly interact with the wave than in the case of Landau damping. These electrons are efficiently accelerated by the wave which causes a strong nonlinear damping and eventually breaking of the plasma wave [94]. The plasma wave breaking will dramatically reduce the coupling of the pump and probe pulses hence reduce the gain of Raman amplification. For cold plasma, the wave breaking limit due to the energy transfer from the pump pulse can be estimated as:

$$\frac{\omega_p}{\omega_0} = (4a_0)^{2/3}, \tag{3.29}$$

which shows that the critical pump intensity increases with the plasma density. This limit is valid in the steady-state situation of full pump depletion. Calculations using the "water-bag" model [95] show that this wave breaking threshold can be reduced significantly for plasmas at finite temperature.

Using a low density plasma can increase the interaction time for Raman amplification by delaying the onset of deleterious instabilities. However, wave breaking sets a lower limit for the plasma density. The ideal condition for Raman amplification is having a plasma density slightly above the wave breaking limit and with a relatively short plasma so that the laser-plasma interaction ends before significant destructive instabilities occur. The optimised parameters are investigated through numerical simulations.

- Resonance detuning

Resonance detuning is one of the main factors that can prevent pump depletion and limit the efficiency of Raman amplification. It can be caused by a pump chirp, a plasma density gradient or plasma heating. Analytical calculations indicate that with a chirped pump pulse the overall Raman amplitude gain for the probe pulse is linear with the interaction time [31]. By contrast, when using a monochromatic pump with no resonance detuning, the probe pulse grows exponentially with the interaction time. The detuning caused by the pump chirp can in principle compensate for the detuning caused by a plasma density gradient or thermal chirp.

Experimental, analytical and numerical results show an interplay between these limitation mechanisms. However, it has not been identified which effects play the dominant role. Those factors should all be taken into account for both planning and analysis of Raman amplification experiments.

Chapter 4

Introduction of the experimental setup

The Raman amplification experiment consists of three major components: the pump pulse, the counter-propagating probe pulse and the preformed plasma. This chapter describes the production and interaction of these three components and is organised as follows. First, the terawatt laser system will be briefly described, followed by a discussion of the methods used to produce the pump and probe pulses. Then the experimental setup will be presented, including details on the laser beam geometry, the capillary alignment procedure, the timing settings and the discharge control. In addition, the diagnostics used to characterise ultra-short laser pulses will also be described. The general layout of this experiment is given in Fig. 4.1.

4.1 Description of the terawatt laser system

This experiment is carried out using the TOPS 10 Hz laser system at the University of Strathclyde. The laser system is based on the CPA scheme where pulses generated by a Ti:sapphire oscillator are stretched prior to amplification. The amplification stage includes one regenerative amplifier and three multi-pass amplifiers (two main amplifiers plus one final amplifier), in which the laser pulses are amplified from several nJ to a maximum of 1.6 J. Finally the high energy laser pulse is compressed from around 250 ps to a minimum of 35 fs. The laser pulse spectrum has a bandwidth of 35 nm

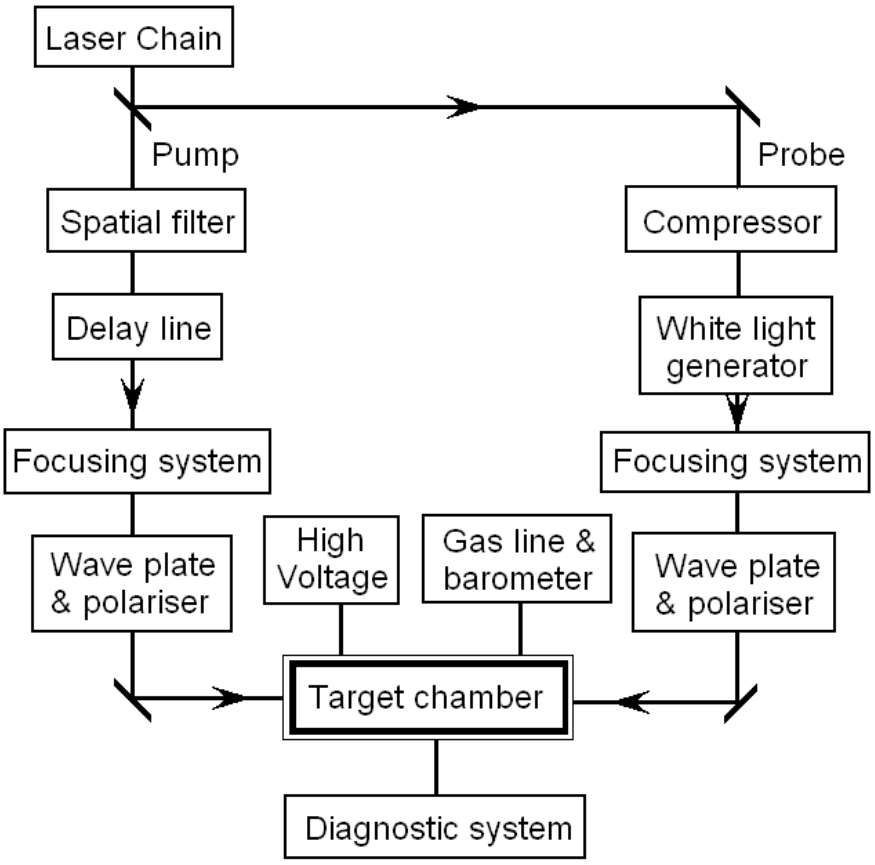

Figure 4.1: Schematic of the general experimental layout.

(intensity FWHM), with a central wavelength at 800 nm. In this experiment, the laser pulse is used uncompressed. Fig. 4.2 shows the diagram of the configuration and the laser parameters at each stage throughout the CPA laser system.

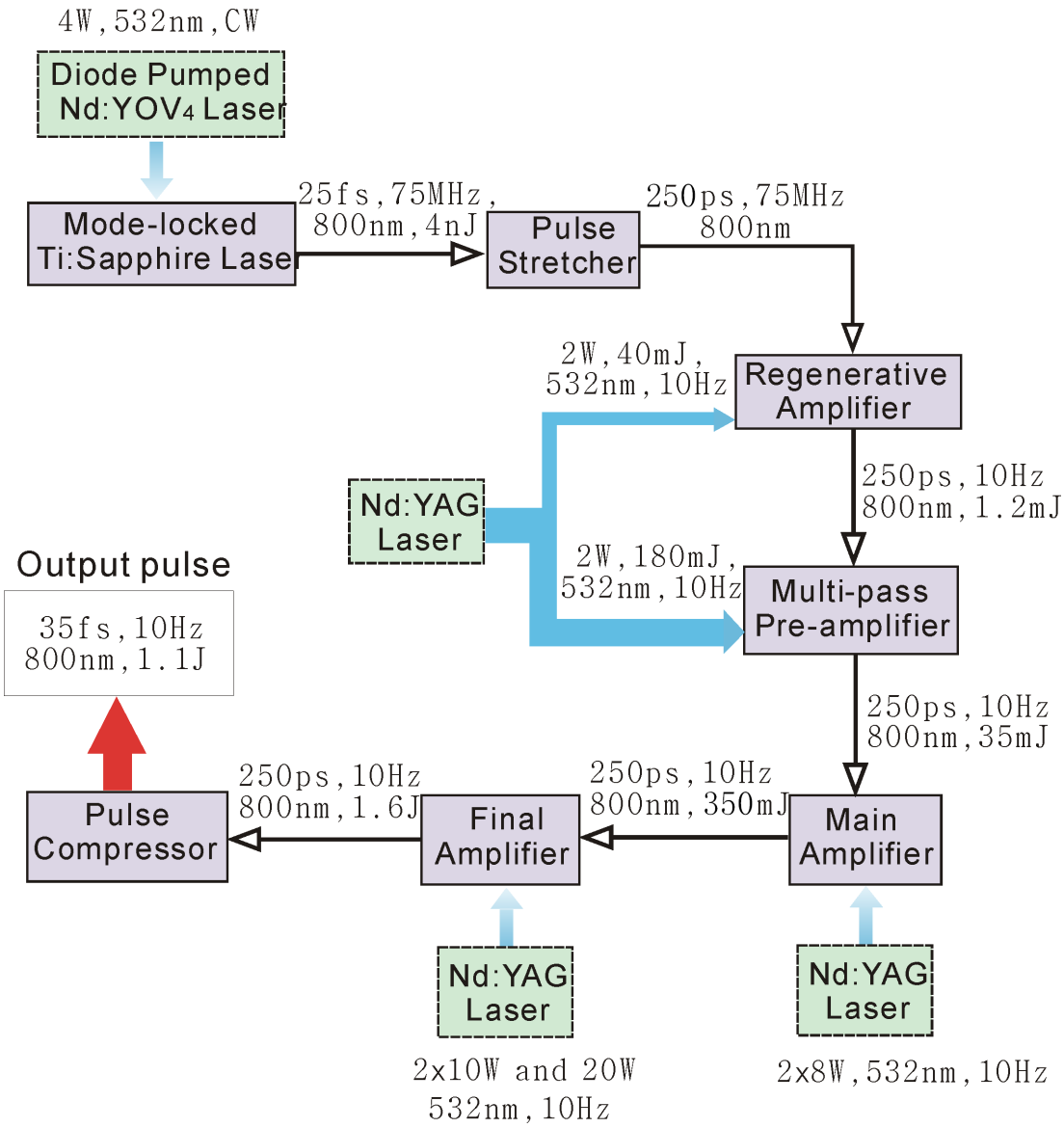

Figure 4.2: Schematic diagram of the laser system.

The Raman amplification experiment is implemented with two pump energy levels. At the low energy level, the on target energy is about 200 mJ, and at the high energy level, the on target energy is maximum 850 mJ. To carry out the Raman experiment with two energy levels and produce the pump and the probe beams, some modifications need to be made to the the TOPS 10 Hz laser system.

- For the low pump energy experiment

A 9 : 1 beam splitter is inserted before the final amplifier where the laser pulse is 250 ps long and has a maximum energy of 350 mJ. 10% of the pulse energy is delivered directly to the Raman setup as the probe pulse. The pump pulse with the remaining 90% of the energy first propagates through a spatial filter made of a short glass capillary in vacuum to clean the transverse laser modes and is then sent to the Raman setup.

- For the high pump energy experiment

Due to the optics arrangement in the laser system, only 90% of the laser beam (i.e. the pump beam of the low energy experiment) is used while the other 10% energy is wasted on a beam block. A Pockels cell is installed after the spatial filter to protect the laser system from damage by the returning pulse in this collinearly colliding experiment (details will be given in Section 4.7.1). A new 9 : 1 beam splitter is set up after the spatial filter and Pockels cell. As before, the probe pulse is directly sent to the Raman setup after the beam splitter, whereas the pump beam will go through the final amplifier and get amplified to different energy levels depending on how many and which of the pump lasers are used. Another spatial filter is placed after the final amplifier to clean the pump beam and also to prevent the probe beam from going back into the final amplifier and being amplified.

After the description of how the pump and the probe beams are delivered from the laser chain to the Raman setup, details of the Raman experimental setup will be introduced in the following sections.

4.2 Generation of the probe pulse

The probe beam obtained from the 10 Hz laser system cannot be directly used in the Raman experiment. There are two additional requirements for a proper probe signal: (1) a short pulse duration of the order of 100 fs for ultra-short pulse Raman amplifi-

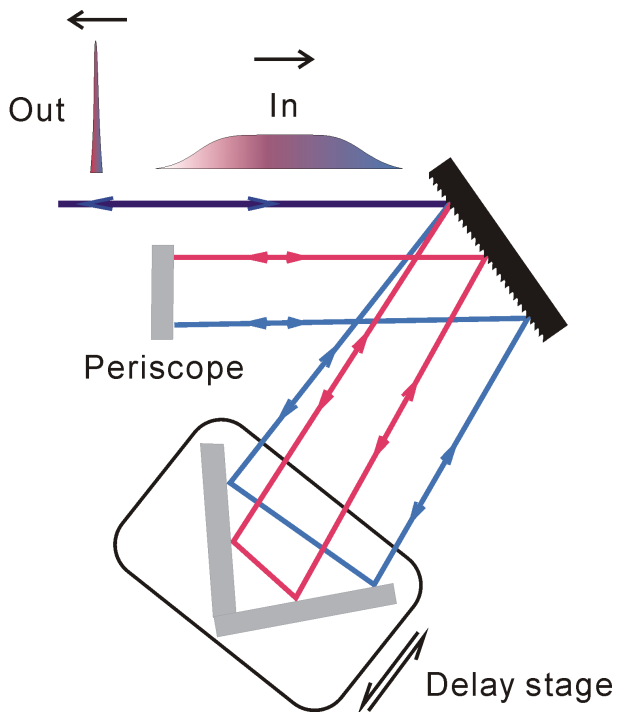

Figure 4.3: Schematic of the compressor setup with different optical paths for short (blue) and long (red) wavelengths.

cation. (2) a central frequency downshifted by ω_p to match the resonance condition dictated by Eq. (2.50), in order to maximise the amplification.

- Compression

To compress the probe pulse, a small purpose-built compressor is employed. It includes one grating and four mirrors (two of them are fixed on a micrometer translation stage to adjust the laser path length and the other two are fixed in position and used as a periscope), as shown in Fig. 4.3. The elements are arranged in a way to provide a double-pass geometry and introduce a negative group velocity dispersion (i.e. shorter wavelengths will go through a shorter path length) to compensate for the positive chirp introduced by the laser stretcher. The minimum compressed pulse duration is 60 fs, limited by the size of the grating. Adjusting the distance between the grating and the mirror pair on the translation stage allows us to produce a not fully compressed probe pulse with either positive or negative chirp rate and pulse length up to several picoseconds. The efficiency of this compressor is tested about 40%.

- Frequency shift

In comparison with the pulse compression, it is more difficult to provide a central frequency shift. Several methods have been tried and employed in this experiment and they will be discussed here.

4.2.1 Laser spectrum modification through self-phase modulation

As one of the consequences of filamentation (introduced in Section 2.6, the laser spectrum modification through nonlinear optical processes can be used together with a low-pass filter to generate the probe pulse with downshifted frequency.

1. Selection of gas

To obtain a broad spectrum with high energy transmission from the filamentation, the right gas needs to be selected. When the laser intensity is very close to the ionisation threshold, ionisation blue-shifting [96, 97] tends to dominate the change of the spectrum. To shift the probe spectrum towards lower frequencies and explore the Raman amplification of a strong signal, gases with higher ionisation thresholds are preferable. According to the parameters shown in Table 4.1, a lighter gas has a higher ionisation threshold making it more suitable for this experiment. However, to get a significant spectral broadening, a fairly large nonlinear refractive index and a short nonlinear interaction length are required. Again, according to Table 4.1, a heavier gas has a larger nonlinear refractive index and a shorter nonlinear interaction length. To make a compromise, A_r is chosen for this experiment.

	I_i [Wcm^{-2}]	n_2 [cm^2/W]	L_{NL} [m]
H_e	12×10^{14}	0.36×10^{-24}	1.078
N_e	7×10^{14}	0.65×10^{-24}	0.599
A_r	2.2×10^{14}	8.5×10^{-24}	0.046
K_r	1×10^{14}	23×10^{-24}	0.017
X_e	0.7×10^{14}	68×10^{-24}	0.0057

Table 4.1: The ionisation threshold I_i, nonlinear refractive index n_2 and nonlinear interaction length L_{NL} of noble gases. n_2 and L_{NL} are given for $T = 295$ K, $p = 1$ bar.

2. Filamentation experiment

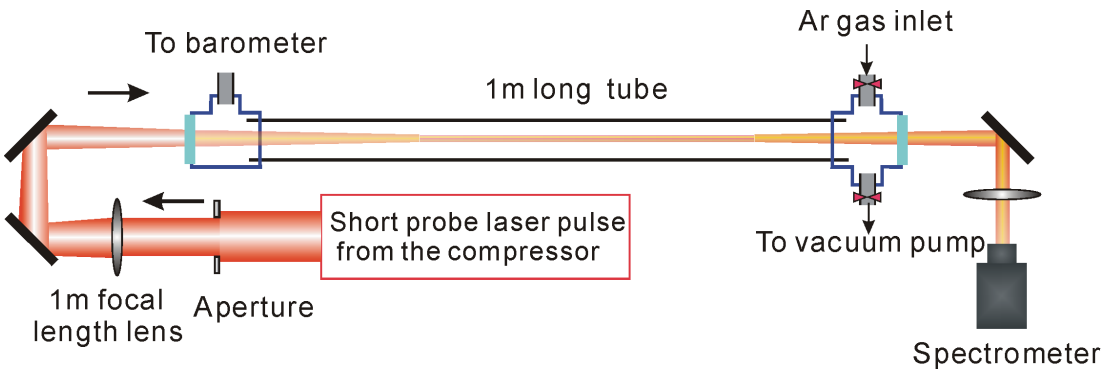

Figure 4.4: Layout of the filamentation experiment.

In the compressor, the probe pulse is compressed from 250 ps to a minimum of 60 fs. It is then directed into a 1 m long sealed transparent plastic tube with 18 mm inner diameter. A vacuum pump and a gas pipe are connected to this tube to evacuate air and insert A_r gas respectively. After the compressor, an aperture is used to change the spot size, then a lens with a 1 m focal length focuses the beam inside the tube. A spectrometer is used for characterising the modified light spectrum. The setup of the filamentation experiment is shown in Fig. 4.4. To generate filaments, the laser beam should not be focused very tightly, otherwise it will just diverge. To pursue the balance between self-focusing and plasma defocussing of a smoothly focused laser beam, a lens with a long focal length is required, as the one used in this experiment. The focal spot diameter is about 100 µm.

As stated previously, the probe pulse is picked up after the main amplifier which is pumped by two Nd:YAG pump lasers SAGA1 and SAGA2 (see Fig. 4.2). Energies of the probe pulse are measured at different positions with different pump lasers (as shown in Table 4.2).

In order to test the possibility of using filament generation to shift the probe frequency, a single Nd:YAG pump laser for the main amplifier is used. The intensity at the focal spot is made slightly above the ionisation threshold by adjusting the pulse duration using the probe's compressor and/or changing the size of the beam size using

	Before compressor	After compressor	After gas tube
No pump laser	0.68 mJ	0.24 mJ	0.14 mJ
With one pump laser	5.3 mJ	1.9 mJ	1.0 mJ
With two pump laser	15 mJ	5.5 mJ	1.8 mJ

Table 4.2: Probe pulse energy at different stages with different pump lasers.

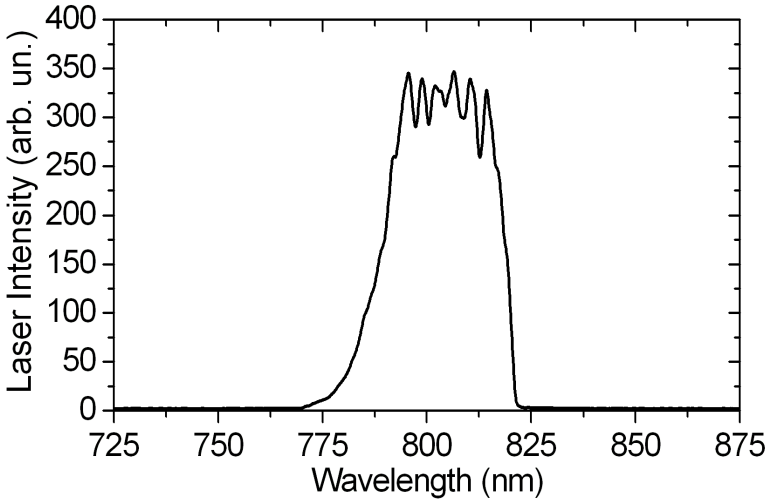

Figure 4.5: The original probe pulse spectrum.

the aperture placed before the focusing lens. After being evacuated by the vacuum pump, the tube is filled with A_r gas. The laser pulse, after propagating through the tube, is directed into a spectrometer, which records the output laser spectra (refer to Fig. 4.4).

The modified spectrum is very sensitive to the laser pulse characteristics as well as the gas pressure inside the tube. In order to maximise the bandwidth, the laser pulse can be adjusted with the compressor and the aperture. As to the gas pressure, the higher the pressure, the more severe the nonlinear effects are. But the filament is more unstable. Therefore, a compromise needs to be found. During the experiment, the pressure is kept between 0.7 and 1 atmosphere.

The laser spectrum after compressor is shown in Fig. 4.5 as a reference. The spectra after the filament generator are presented in Fig. 4.6 from which we can see that

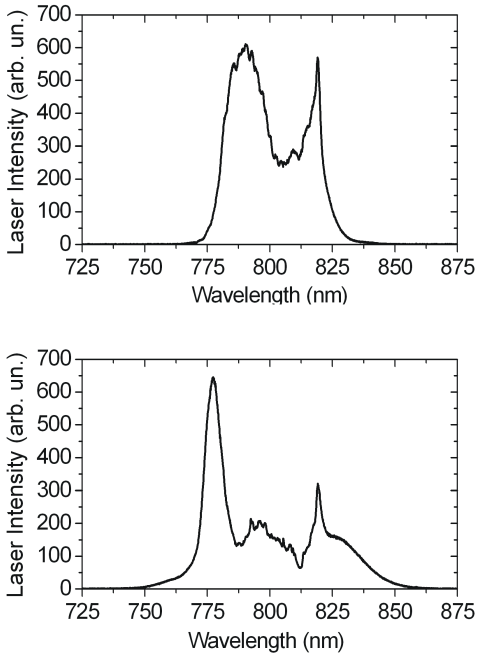

Figure 4.6: Spectra after the filament generator without coloured glass filters in front of the spectrometer for different aperture settings and pressure.

the frequency modulations are quite severe and very sensitive to the input laser pulse parameters. In addition to pulse duration and spot size, the chirp direction also plays an important role on the self-modulation process [98].

The new generated frequencies appear on both sides of the spectrum, but it is preferentially added to the short wavelength side. Although it is possible to make the red-shift dominant, it is not easy to get it stable. A small alignment change can trigger the spectrum to shift to the other side. To ensure that the spectrum does not contain frequencies that could transfer energy to the pump pulse, filters are added to remove the high frequency components. A set of coloured glass filters is used for this purpose. The transmission curves are shown in Fig. 4.7, from which it can be seen that RG-830 and RG-850 filters are the most appropriate. The modified spectrum after propagation through the combination of RG-830 and RG-850 filters is shown in Fig 4.8. The central frequency is shifted to 835 nm and the FWHM bandwidth is 28 nm.

By adjusting the compressor to change the pulse length, the central frequency of the modified spectrum can change from 835 nm to 858 nm (shown on Fig. 4.9) which gives enough allowance to match the plasma frequency and thus the plasma density.

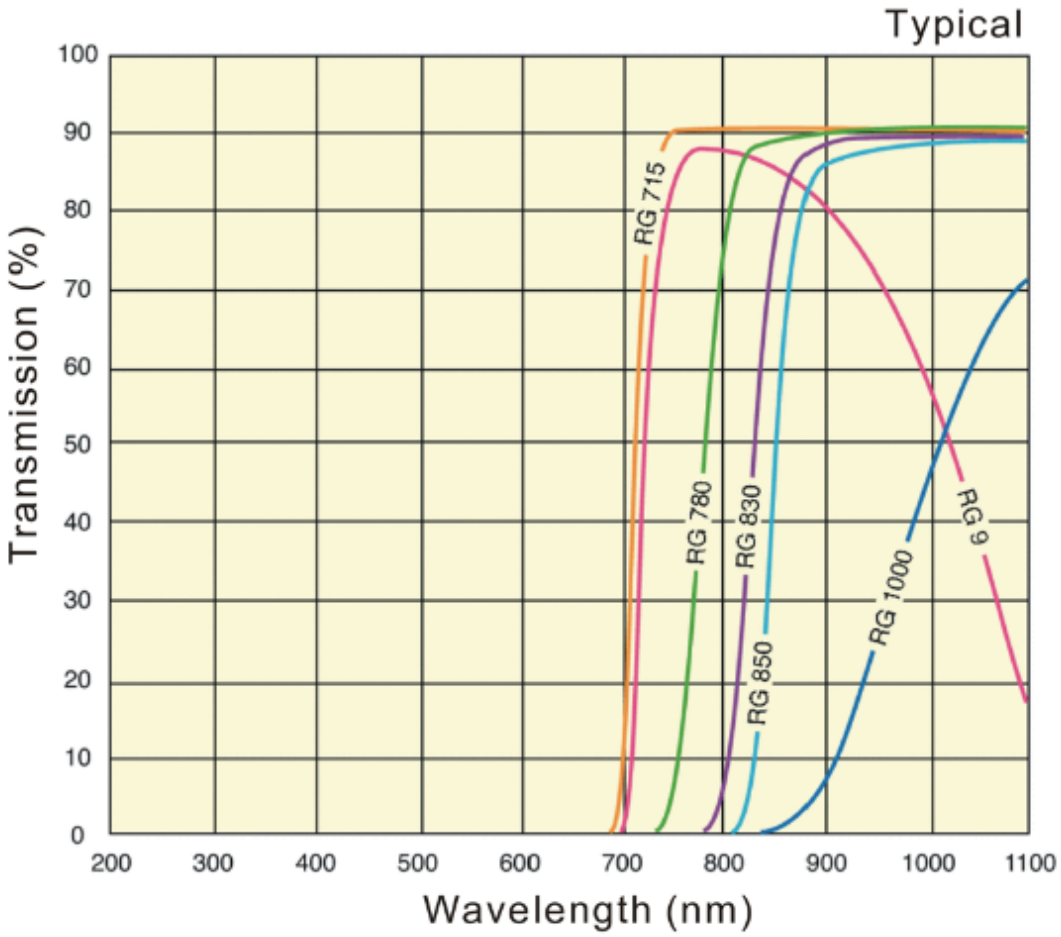

Figure 4.7: The transmission curve of a set of coloured glass filters.

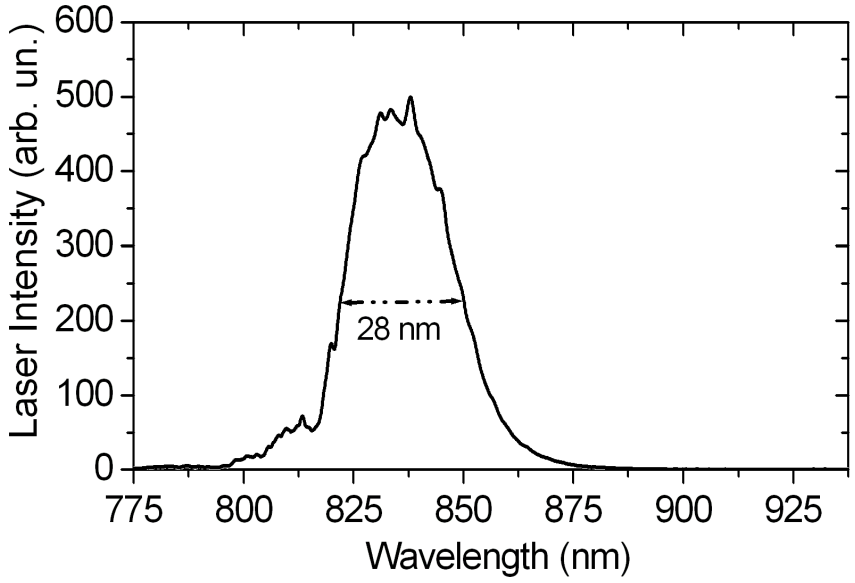

Figure 4.8: Probe pulse spectrum modified through self-phase modulation and filtered by RG-830 and RG-850. The spectrum is centred at 835 nm and has 28 nm bandwidth at FWHM

With the central wavelength of the pump beam at 800 nm, the plasma density required for the parametric energy conservation is calculated and plotted in Fig. 4.10 as function of the probe wavelength. In this calculation, the Bohm-Gross shift is taken into account and the temperature is assumed to be 5 eV.

The focal spot of the probe pulse after the filament generator is imaged with a CCD camera to test the focusability. An image of the focus is shown in Fig. 4.11.

3. Problems impeding the use of filament generation

Although the filament generation experiment to downshift the probe frequency is generally successful, it comes with some operational difficulties when doing the Raman amplification experiment. Firstly, the aperture before the gas tube can not be freely adjusted to get a proper probe spectrum since it will also change the focal spot size which needs to match the size of plasma channel for mono mode guiding through the capillary. Second, the beam quality degrades after the self-phase modulation, which

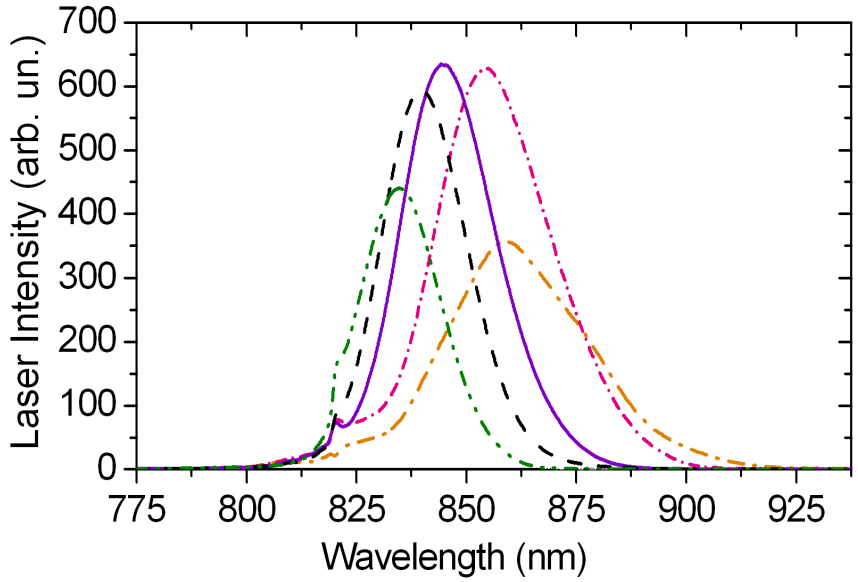

Figure 4.9: Smoothed modified probe spectra (after glass filters) change due to the different laser pulse duration.

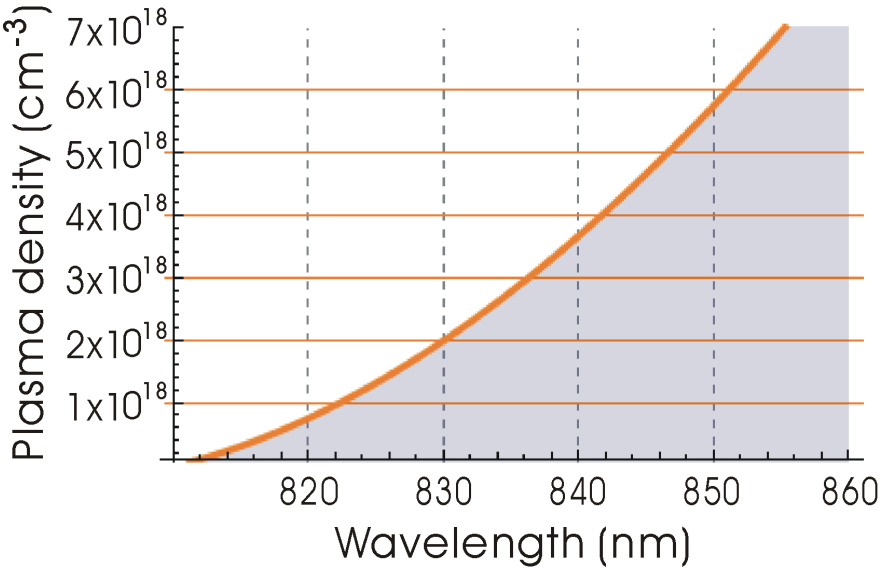

Figure 4.10: Assuming the pump central wavelength is at 800 nm, with different plasma density thus the plasma frequency, the probe central wavelength which satisfy the parametric energy conservation equation is plotted. The Bohm-Gross shift is taken into account and the temperature is assumed to be 5 eV.

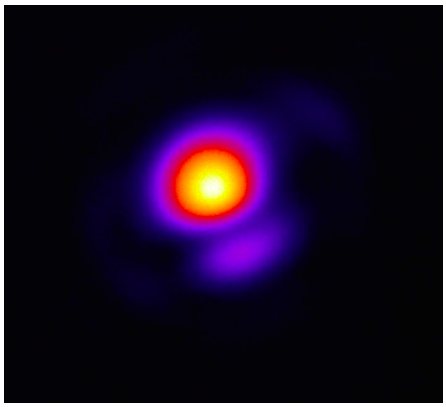

Figure 4.11: Focal spot of the probe pulse after the filament generator.

generates unavoidable hot spots that will affect the amplification process and the usability of the amplified pulse. Third, to enter the Compton regime, an intense probe pulse is preferable, however, the self-phase modulation through filament generation is very sensitive to the pulse intensity and works well only with moderate probe energies.

Due to the practical problems stated above, an alternative way of shifting the central wavelength of the probe pulse is demanded.

4.2.2 Making use of the grating in the probe's compressor

The alternative way of getting the probe central frequency downshifted is to "misalign" the compressor by making the high frequency components in the spatially dispersed spectrum miss the grating. With the narrower spectrum bandwidth, the shortest pulse duration increases to 120 fs.

The advantages of this method are as follows: (1) pulse-to-pulse stability is improved, (2) higher probe intensities become possible, (3) the experimental complexity is decreased. The disadvantage is the longer duration of the probe pulse as result of the smaller bandwidth, but this is not an essential problem that will prevent the investigation of the physics involved in the amplification process.

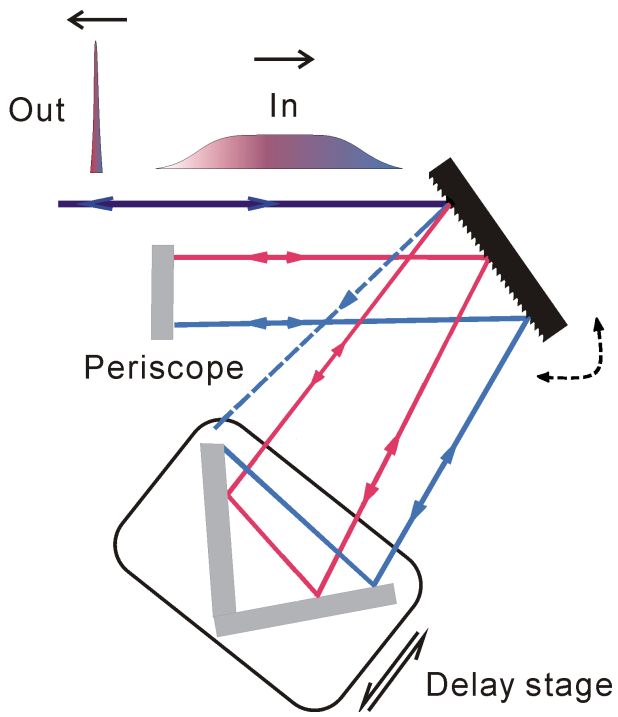

Figure 4.12: The compressor is “misaligned” to cut the high frequency components by the edge of the grating.

4.2.3 Cut-off filter

In order to provide a sufficiently detuned probe pulse and reduce the energy of the returning pump pulse, a cut-off filter is added before the probe pulse propagates into the target chamber. A cut-off filter is an optical device which reflects a particular range of frequencies which are higher than the cut-off frequency, while the remaining frequencies are transmitted. The cut-off frequency varies with the angle between the filter and the incident beam. With the angle increasing, the cut-off frequency increases as well. In this experiment, the cut-off frequency is set to be around 800 nm to reduce energy transfer from the high frequency probe pulse to the low frequency pump and in the mean time to eject the high frequency pump after interaction.

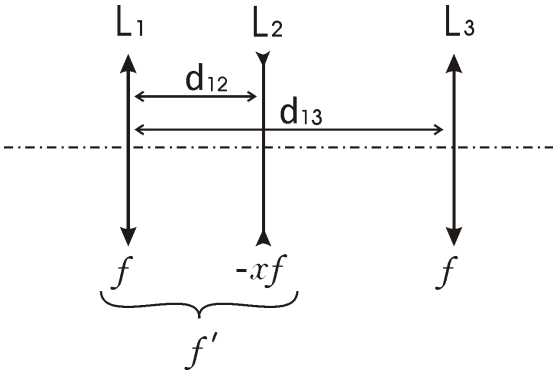

Figure 4.13: L_1 and L_3 are converging lenses with focal length f while L_2 is diverging lens with focal length $-xf$. f' is the focal length of a virtual lens from the combined system of L_1 and L_2. The distance between L_1 and L_2 is d_{12}, between L_1 and L_3 is d_{13}.

4.3 Focusing system

To guide the laser beam through a capillary, a matching spot size is mandatory. The initial spot size at the output of the main amplifier is 20 mm. In order to focus it down to 50 μm at the entrance of the capillary, according to Eq. (2.37), a focusing element with a 1.5 m focal length is required. However, since the divergence of the beam may change slightly from day to day, fine adjustment of the focal spot size and its position is essential for this experiment. For this reason, a zoom lens system is employed in both arms.

As shown in Fig. 4.13, it is designed with three lenses, including two converging lenses (L_1 and L_3 which have the same focal length f) and in between a diverging lens (assuming L_2 has focal length $-xf$). The focal length f' of the virtual lens (i.e. the combination of L_1 and L_2) and the magnification M are given by

$$f' = \frac{-xf^2}{(1-x)f - d_{12}}, \tag{4.1}$$

$$M = \frac{f}{f'} = -\frac{(1-x)f - d_{12}}{xf}. \tag{4.2}$$

For a fixed x, the maximum magnification will be reached when lens L_1 is close to L_2, i.e. $d_{12} = 0$, so $M_{max} = -(1-x)f/xf$. Due to the symmetry of this system the maximum reduction will occur when the laser beam propagate from the opposite direction, in other words, when the lens L_2 is close to L_3 we have $M_{min} = -xf/(1-x)f$.

For this experiment, x is chosen to be $1/4$. The focal length for L_1 and L_3 is 1 m while for L_2 is 0.25 m. Therefore, the magnification of the initial beam spot size is between $1/3$ and 3.

4.4 Capillary and power supply

In this experiment, plasma is generated in a hydrogen-filled capillary discharge waveguide. It provides the amplifying medium and at the same time, guides the laser beam through. The main components of the capillary waveguide system, including the capillary, its housing, gas injection and the high voltage power supply, will be described in this section.

4.4.1 Capillary design and micro-machining

The most important element in this experiment is the capillary. Extending the original design by Hooker et al. [60], the capillary used in this experiment is designed and micro-machined at the University of Strathclyde using femtosecond laser micro-machining technique developed at Strathclyde [99, 100]. Since femtosecond lasers are capable of manufacturing 3-D structures accurately, the femtosecond kHz laser in the TOPS lab is used to machine the capillary.

- Capillary design

A gas-filled capillary for generating plasma and guiding laser pulses is essentially a long and narrow cylindrical waveguide with gas inlets. To make it robust and easy to use, the capillary waveguide is made of two identical sapphire or alumina plates with dimensions of 40 mm $\times$ 10 mm $\times$ 5 mm. Each plate has a laser-machined groove in the centre for laser propagation and two on the top for gas injection, as can be seen in Fig. 4.14(a). The two identical plates glued together will form a 40 mm long, 300 μm diameter circular capillary channel with two gas injections with diameter of 500 μm, as shown in Fig. 4.14(b). Four silicon O-rings are attached between the capillary and

its housing at the entrance of the gas inlets and on both sides of the capillary channel to avoid gas leaks.

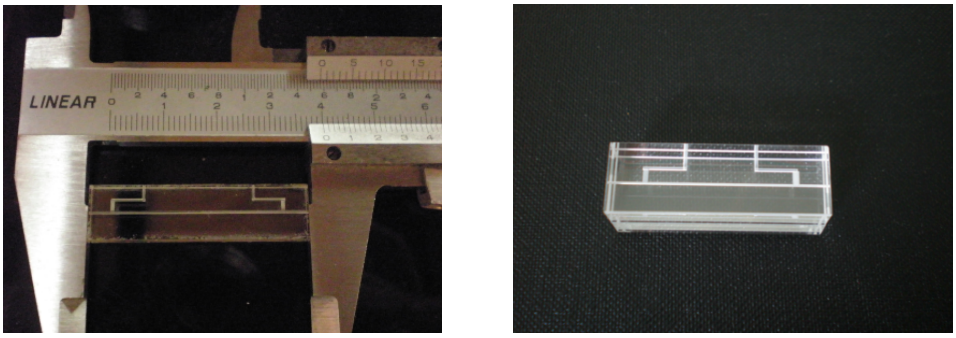

(a) (b)

Figure 4.14: (a) Half of the sapphire capillary (b) Sapphire capillary.

Sapphire (single crystal alumina) and alumina are similar with regard to hardness and thermal conductivity. The main difference is that sapphire is transparent so that the plasma glow can be observed from outside, which allows spectroscopic or interferometric measurements of the plasma density using Stark broadening of the hydrogen lines or interferometry method. The other advantage of using a transparent capillary is that the generation of plasma can be monitored outside the chamber. However, since sapphire is much more expensive and the plasma behaviour can be detected indirectly by looking at the current pulse profile striking through the capillary, most of this experiment is conducted with the alumina capillary.

A new type of capillary has also been designed, where the gas inlets are drilled through one plate, as presented in Fig. 4.15. This is to prevent the gas leaks through the gap between the two glued plates and the o-ring if the two plates are not perfectly aligned. The other advantage of this design is that the force from the screw (refer to Section 4.4.2) pushing the capillary against the o-rings for gas injection will push the two plates even closer. This new type of capillary is employed in the Raman experiment with high pump energy.

- Micro-machining workstation

To machine the capillary, a sapphire or alumina plate is mounted on a X and Y

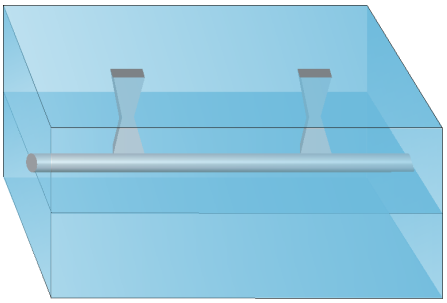

Figure 4.15: Schematic diagram showing how a new design of capillary with gas injection channels on one plate. The diagram is not to scale. The gas injection slots are hourglass-shaped with the cross-section of 200 µm× 700 µm at the centre.

translation stage which is computer controlled through a LabVIEW program. The 50 fs, 1 kHz laser beam is focused onto the plate by a lens, which is fixed on a Z translation stage allowing 3-D manufacturing. The focused laser spot size is w_0 =12 µm with the energy of E =150 µJ, which corresponds to a laser intensity of $I = 6.6 \times 10^{14}$ Wcm^{-2}. The high laser field leads to a rapid ionisation of the material and the hot plasma expands away leaving a crater in the material. Scanning the laser on the plate with speeds from 12 to 24 mm/s will allow $1 \sim 2w_0$ between the centre of two adjacent spots. The scanning speed is determined by the laser repetition rate and the focal spot size. The space between each scanning line is set to be 5 µm. The number of scan is linearly dependent on the required depth of the groove [99].

4.4.2 Capillary housing

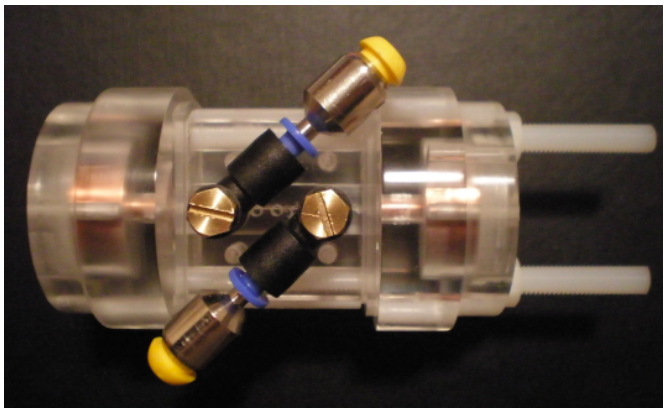

Figure 4.16: The capillary housing consist three parts. The central part holds the capillary and attaches the gas inlet while the two parts on each side hold electrodes. The three parts hold together by two long plastic screws.

The capillary housing that holds the capillary and provides the connections be-

tween the capillary, the high voltage discharge and the gas injections is designed and manufactured at the University of Strathclyde. It is designed to work in a vacuum environment and is composed of three parts, as can be seen in the Fig. 4.16. The central part holds the capillary block and attaches the gas feeds to the channel for gas injection on the top of the capillary. The two end parts of the housing are identical. Each of them holds one electrode that conducts the high voltage discharge through the capillary channel. The three parts are firmly hold together by two long plastic screws.

The electrodes are made of copper with a cylindrical base of 1 cm diameter and a funnel-shaped tip, as can be seen in Fig. 4.17. A hole is drilled in the centre of the electrode for the laser propagation. A metal screw embedded in the cylinder base is used to fix a high voltage wire connecting the high voltage from the vacuum chamber port to the electrode. The electrode tip, with a hole of 0.7 mm in diameter, is in contact with one end of the capillary. An O-ring is placed around the electrode tip to insulate the capillary housing from the discharge and force the gas flow through the electrode hole.

Two plastic tubes are used to supply gas to the capillary, which also offer the flexibility of moving the capillary housing in the vacuum chamber. One end of the plastic tube connects to a metal tube on a flange of the chamber and the other end is connected on the top of the capillary housing by a simple push-through connector, as shown in Fig. 4.16.

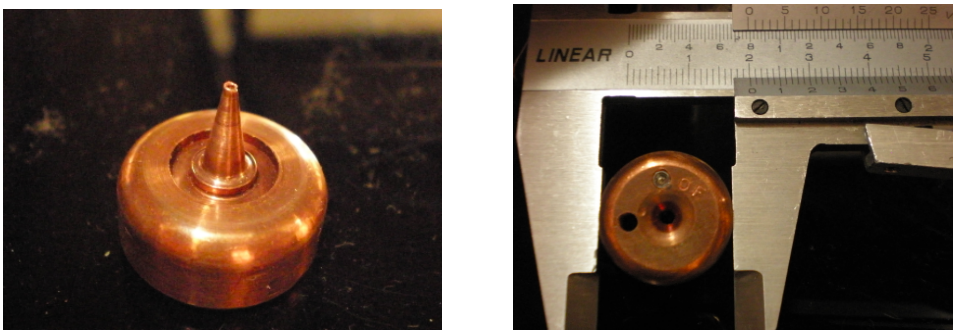

(a) (b)

Figure 4.17: Electrode

The capillary housing is mounted on a 5-axis stage, including X-Y-Z translation stages, and a gimbal mount that provides the rotation axes. These vacuum compatible stages are mounted on the base of the vacuum chamber. To facilitate the alignment procedure, the probe pulse entrance of the capillary is placed in the fixed plane of the gimbal mount.

4.4.3 High voltage power supply

The high voltage power supply produces a 15 kV discharge applied across the anode and cathode electrodes of the gas-filled capillary. When the current of 250 A strikes along the channel, the hydrogen is transformed into an under-dense plasma via avalanche breakdown and plasma heating. This home-built, solid-state, high voltage pulsed power supply is mainly composed of four parts: an external adjustable power supply, a FET (Field Effect Transistors) driver, a main solid-state switch and a circuit for the pulse compression. The structure of the power supply is presented in Fig. 4.18.

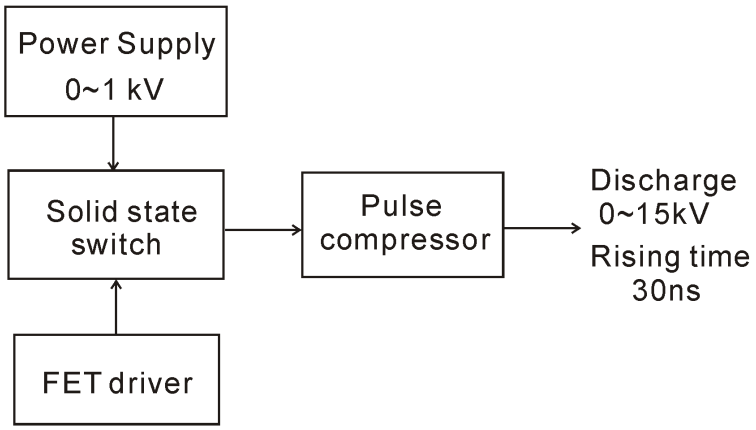

Figure 4.18: Schematic diagram of the circuit of the high voltage power supply

The external adjustable DC power supply provides a maximum of 1 kV to charge up the storage capacity in the solid-state switch. Once charged, it will switch into the primary of a step-up transformer via six parallel IGBTs (Insulated Gate Bipolar Transistors). The FET driver controls the switching of the IGBTs. Taking an external trigger, the FET driver allows the first capacitor to discharge across the gate-drain

junction of the IGBT. Then a high value capacitor slowly discharges across the gate-drain junction to keep it open. The pulse compressor, built from a series of L-C circuit, compresses the high voltage pulse after the transformer from a duration of 3 μs to about 150 ns and reduces the voltage rise time to 30 ns. The hold-off time of the inductors is equal to the charge up time of the capacitors, which enables a discharge rise time of 30 ns to appear along the capillary delivering about a 15 kV discharge with a current of about 250 A, depending on the density inside the capillary.

The temporal jitter of the current pulse, which originally arises from the stochastic nature of the avalanche ionisation process, seriously affects the synchronisation of the laser pulse with the plasma production. This type of high voltage power supply, which has a typical temporal jitter of 10 to 20 ns, induces a relatively large shot-to-shot instability in the experimental results. To minimise the jitter, it is crucial to apply a voltage pulse with minimal rise time.

A new design utilising fast IGBT circuitry as the high voltage switch and a wound transmission line transformer (TLT) for voltage gain is made in order to generate current pulses that suffer very little from the temporal jitter. The tested jitter in the leading edge of the current pulse is reduced to 4 ns. Another desirable attribute of the power supply is minimal applied voltage to reach full ionisation such that electrical noise in the experimental environment is minimised [101]. This new development is planned to be employed in future experiments.

4.4.4 Gas injection and barometers

The capillary is kept in vacuum to avoid any laser breakdown of air. One rotational pump and one turbo-molecular pump are connected in series to form a two stage pumping system to keep the pressure in the vacuum chamber below 10^{-5} mbar. Thus, when gas flows into the capillary the pressure remains less than 10^{-3} mbar, which is sufficient to avoid breakdown and ionisation-induced defocusing of the laser beam. One barometer, connected to the vacuum chamber, monitors the pressure in the chamber.

Gas injection is controlled by a pulse valve connected outside the vacuum chamber. The pulse valve, taking an external trigger, is synchronised with the high voltage discharge. The second barometer between the pulse valve and the capillary is to measure the pressure which is taken as the gas backing pressure for the capillary.

4.5 Timing setting

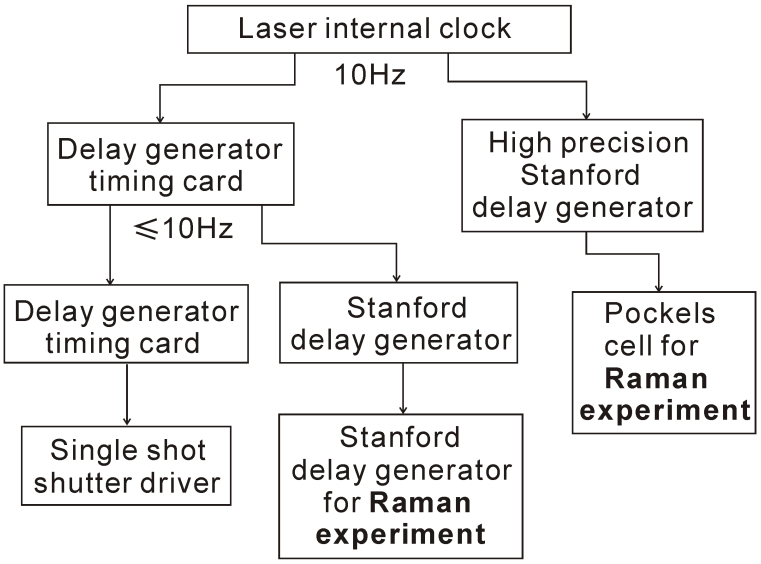

Figure 4.19: Diagram of timing setting for Raman experiment

Timing setting is a crucial factor for this experiment since the two laser pulses, the discharge and the pulse valve for gas injection need to be synchronised together. The triggering system will be introduced first followed by the timing setting for the Raman experiment.

The initial trigger signal is obtained from the laser internal clock at 10 Hz. A computer controlled timing card takes the signal and reduces the repetition rate to less than 10 Hz according to the experimental requirements. This timing card also triggers a second timing card and a Stanford delay generator which triggers the Stanford delay generater for the Raman experiment. The second timing card is used to trigger a single shot shutter, which effectively reduces the laser repetition rate by blocking unwanted

laser pulses before the main laser amplifier.

A high precision Stanford delay generator is triggered by the laser internal clock, in parallel with the first timing card, and is used to trigger the Pockels cell protecting the laser chain from possible back coming radiation from the Raman experiment. For this purpose, the Stanford trigger generator is designed to have a temporal jitter less then 3 ns. To gain enough time for the trigger signal propagating to the Pockels cell and the Pockels cell to respond, the trigger unit takes the timing signal from the previous pulse. A schematic of the trigger system is shown in Fig. 4.19.

The synchronisation of the two laser pulses with the gas injection and the discharge are controlled by the second Stanford delay generator. There are four channels giving TTL signals. Channel A gives the general delay corresponding to the time taken by a pulse to reach the Raman experimental setup from the laser system. The pulse valve is gated by the rising edge of channel A and the falling edge of B with a delay of 210 ms which is the opening time for the gas. Channel B also triggers the discharge at the same time, meaning that once the pulse valve is closed the high voltage discharge strikes through the capillary. Channel C and D are set to trigger the CCD camera in the imaging system and the time-resolved diagnostic system, respectively.

4.6 Time-resolved diagnostic system

With the development of the ultrafast laser technology, it becomes impossible to characterise femtosecond laser pulses by just using electronic detectors, since their response time is typically longer than 1 ns, many orders of magnitude longer than the laser pulse duration. Even for the ultra-fast diode and streak camera, the best temporal resolution is on the order of hundreds of fs.

Lacking fast detectors, the general idea is to use the pulse itself to provide a time gate for high harmonic generation, encoding the temporal electric field of a short pulse into a measurable signal and extracting the field from the data. In the following sec-

tions, several experimental approaches employed in this experiment to characterise ultra-short electromagnetic pulses will be introduced including autocorrelations, cross-correlation, FROG (frequency-resolved optical gating) and SPIDER (spectral phase interferometry for direct electric-field reconstruction).

4.6.1 Autocorrelation and cross-correlation

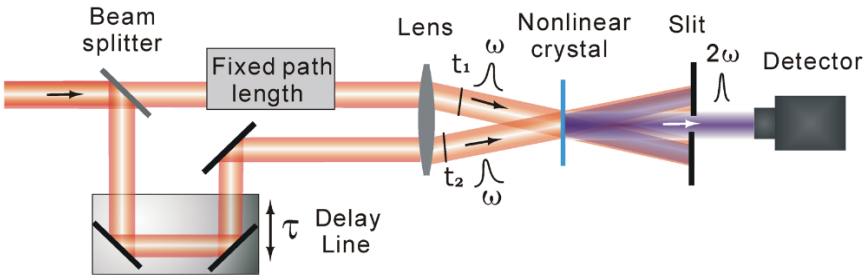

Figure 4.20: Schematic of an autocorrelator setup

Autocorrelation and cross-correlation are techniques used most frequently to measure the temporal structure of ultra-short pulses. In an autocorrelator, one beam is split into two. One travels through an optical path with a fixed length and the other through a path with an optical delay line responsible for overlapping the two replicas in time. Focusing the two pulses on a nonlinear crystal, such as BBO or KDP, a beam at the second harmonic frequency is produced by mixing one photon from one replica and one from the other.

For the intensity autocorrelation, the average power of the generated beam is recorded as a function of the relative delay between the two pulses with an integrating detector, as shown in Fig. 4.20. In such a setup, the translated distance of the delay line L corresponds directly to the relative time delay of $\tau = 2L/c$, in other words, the temporal profile is encoded into a signal of electric field intensity versus distance. For example, when $L = 1$ µm, $\tau \approx 6.6$ fs. The signal at the second harmonic as a function of time has the form:

$$I_{AC}(\tau) \propto \left|\chi^{(2)}\right|^2 \int |E(t)E(t-\tau)|^2 dt = \left|\chi^{(2)}\right|^2 \int I_{\omega_1}(t) I_{\omega_2}(t-\tau) dt, \tag{4.3}$$

where $\chi^{(2)}$ is the second-order susceptibility of the nonlinear crystal, and I_{ω_1} and I_{ω_2} are the replica's intensity. The shape of the autocorrelation signal is a function of the incoming pulses and the conversion factor depends on the pulse shape. A list of relationships between the parameters of the autocorrelation and the input signals are presented in Table 4.3. If the incoming pulse shape is unknown, one can use nonlinear curve fitting to determine the pulse shape and then the corresponding conversion factor.

$I(t)$	$K = \Delta\nu\tau_p$	$G_0^2(\tau)$	τ_p/τ_G
Gaussian $I(t) = e^{-t^2}$	0.4413	$e^{-\tau^2/2}$	0.7071
Diffraction function $I(t) = \frac{\sin^2 t}{t^2}$	0.8859	$\frac{3}{2\tau^2}\left(1 - \frac{\sin 2\tau}{2\tau}\right)$	0.7511
Hyperbolic sech $I(t) = \mathrm{sech}^2 t$	0.3148	$\frac{3(\tau\coth\tau - 1)}{\sinh^2\tau}$	0.6482
Lorentzian $I(t) = \frac{1}{1+t^2}$	0.2206	$\frac{1}{1+(\tau/2)^2}$	0.5000

Table 4.3: Different mathematical descriptions of laser pulses and their time-bandwidth products are given together with the second-order autocorrelation functions and the conversion factors for determining the pulse duration (at FHWM). $\Delta\nu$ is spectral width (FWHM), τ_p is pulse width (FWHM) and τ_G is autocorrelation width (FWHM) `http://www.chem.gla.ac.uk/staff/wynne/p/Blue_Book.pdf`

The multi-shot scanning operation by introducing different delays in the two laser pulses is not practical in this experiment, therefore a single-shot autocorrelator is employed to characterise the probe temporal profile in the preparation process of the experiment, such as characterising the probe pulse after compression and frequency downshift. The difference between a single-shot and a multi-shot autocorrelator is that in a single-shot autocorrelator the two beams need to overlap at an angle in a con-

figuration which can provide a suitable temporal window and resolution, as shown in Fig. 4.21 [102]. A cylindrical lens is a good way to increase the intensity in one axis while keeping the temporal axis large and undistorted. The generated second harmonic signal in the nonlinear crystal represents the time-integrated intensity product. Along the x direction, the autocorrelation function is transformed into a spatial intensity distribution of second harmonic emission which can be recorded with a CCD camera. The FWHM (τ_G) of the spatial intensity distribution is related to the laser pulse duration as $\tau_p = (K\tau_G \sin\phi)/c$, where ϕ is the half angle between the two beams (outside the crystal) and K is a numerical factor governed by the laser pulse shape given in Table 4.3. However, without knowing the phase information, there will be two main ambiguities: the intensity profile is not uniquely related to the input pulse, and the chirp information cannot be determined. Therefore, for probe pulse characterisation, advanced pulse reconstruction methods are then applied, as described in Sections 4.6.2.

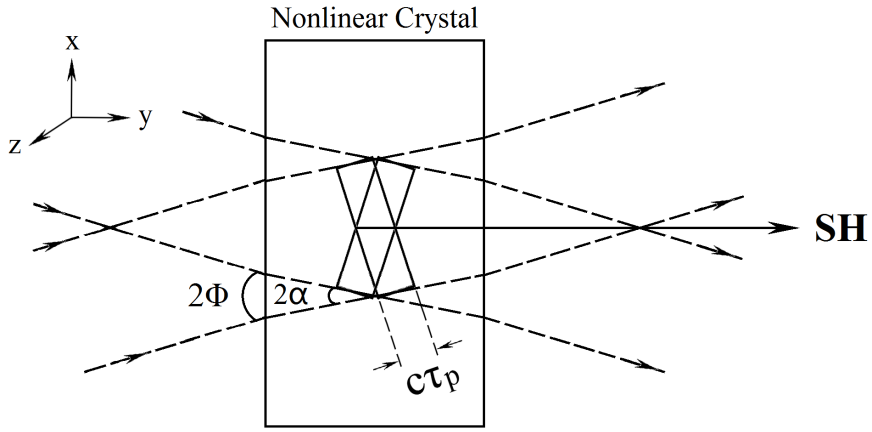

Figure 4.21: Schematic of achieving single-shot autocorrelation of femtosecond laser pulses from spatial intensity profile of second-harmonic beam generated in a nonlinear crystal.

Similar to an autocorrelator, a cross-correlator is also based on a homodyne detection system. The difference is that cross-correlation uses a reference pulse of known character to detect an unknown pulse. An ultra-short pulse is commonly applied to select a single point of the unknown pulse with a relatively long pulse duration. Varying the delay line to make a scan and determine the waveform shape of the pulse under test

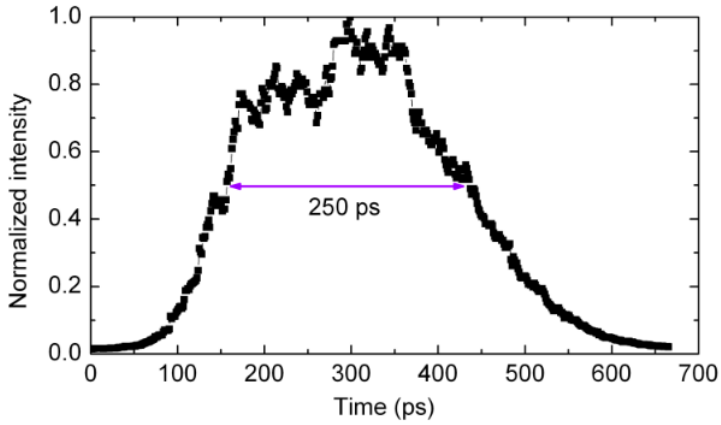

Figure 4.22: Cross-correlation trace of the pump pulse. The pulse temporal waveform has a flat-top and the duration at FWHM is 250 ps.

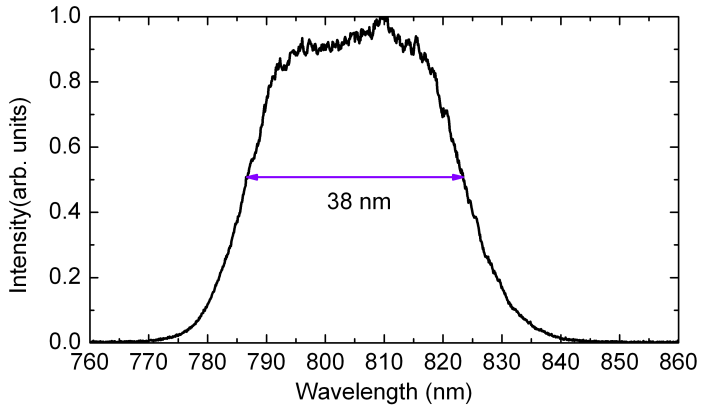

Figure 4.23: Pump pulse spectrum with 38 nm bandwidth at FWHM.

directly from the intensity of the second harmonic signal.

A temporal waveform measurement of the pump pulse is carried out with the cross-correlation technique. The compressed probe pulse is used as the selector and it is set to pass a delay line. The second harmonic signal is recorded by a diode. A LabVIEW program is written to control the motorised translation stage and to record measurements every 0.2 mm. The cross-correlation trace of the pump pulse is shown in Fig. 4.22 together with the pump spectrum in Fig. 4.23.

4.6.2 FROG

Currently, the most widely used devices to precisely characterise the electric field of ultra-short laser pulses with no prior assumptions are the SPIDER [103] and the FROG [104]. Both devices can measure the phase and amplitude of the laser electric field, since they use at least one time-stationary and one frequency-stationary filter, which is a necessary and sufficient condition to fully reconstruct a laser pulse temporal profile [105].

SPIDER systems have the advantage of using a fast and simple algorithm to extract the phase information, in contrast with the complex and slow multiple iterative algorithm required by FROG. Therefore, a SPIDER has been used as a diagnostic for the Raman amplification experiment at first. However, due to the practical difficulty of using SPIDER with weak input signals, it is later replaced by a SHG FROG due to its high sensitivity.

FROG is another useful technique for characterising femtosecond pulses, with which both the intensity and phase of a femtosecond pulse can be determined [106]. There are several versions of FROG with slightly different beam geometries, such as polarisation gate (PG), self-diffraction (SD), transient-grating (TG), second-harmonic generation (SHG), and third-harmonic generation (THG).

The geometry of SHG FROG is similar to the intensity autocorrelator, in which one beam is split into two and then recombine in a nonlinear crystal. The difference is that for the FROG the autocorrelation trace is sent to a spectrometer with a two-dimensional detector attached, such as a CCD camera. The signal can be measured with dependence on delay (time information) in one direction and frequency in the other. Therefore, the time-frequency distribution is uniquely related to the input pulse field. A diagram showing the FROG setup is presented in Fig. 4.24.

The SHG FROG trace is given by

$$I_{FROG}^{SHG}(\omega,\tau) \propto \left| \int_{-\infty}^{\infty} E_{sig}(t,\tau) exp(-i\omega t) dt \right|^2 \tag{4.4}$$

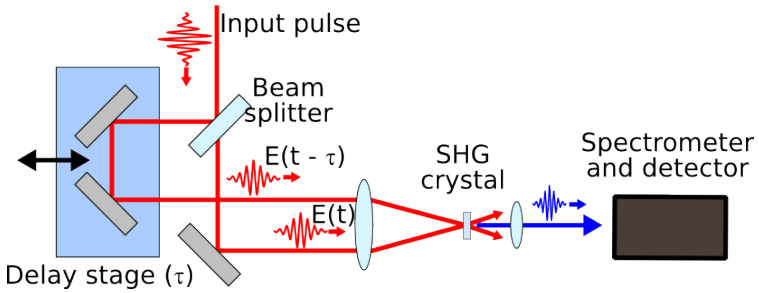

Figure 4.24: Schematic diagram of a SHG FROG setup

and the signal field $E_{sig}(t,\tau)$ is

$$E_{sig}(t,\tau) = E(t)E(t-\tau). \tag{4.5}$$

With a pulse retrieval algorithm described in Ref. [107], a $E_{sig}(t,\tau)$ can be find which satisfies both constraints: Eq. (4.4) and (4.5).

The advantages of this technique are: (a) it is a single-shot measurement, (b) it is possible to measure pulses as weak as 10 nJ and (c) the feedback regarding the validity of the measurement data allows to check and correct a trace for many types of systematic error, even when the source of the error is unknown. The ambiguity is the direction of time as $E(t)$ and $E(-t)$ give the same SHG FROG trace. Practically, this ambiguity can be removed by placing a piece of glass in the pulse which will induce a small trailing satellite pulse. A photograph of the home made FROG setup is shown in Fig. 4.25.

4.7 Experimental setup and alignment procedure

In the previous sections, we have described the laser system, the methods used to generate frequency downshifted and compressed probe pulses, the focusing system for both beams, the gas-filled capillary waveguide together with gas injection and timing control, as well as various techniques of time-resolved diagnostic systems, covering most of the noteworthy details for this experiment. In this section the general experi-

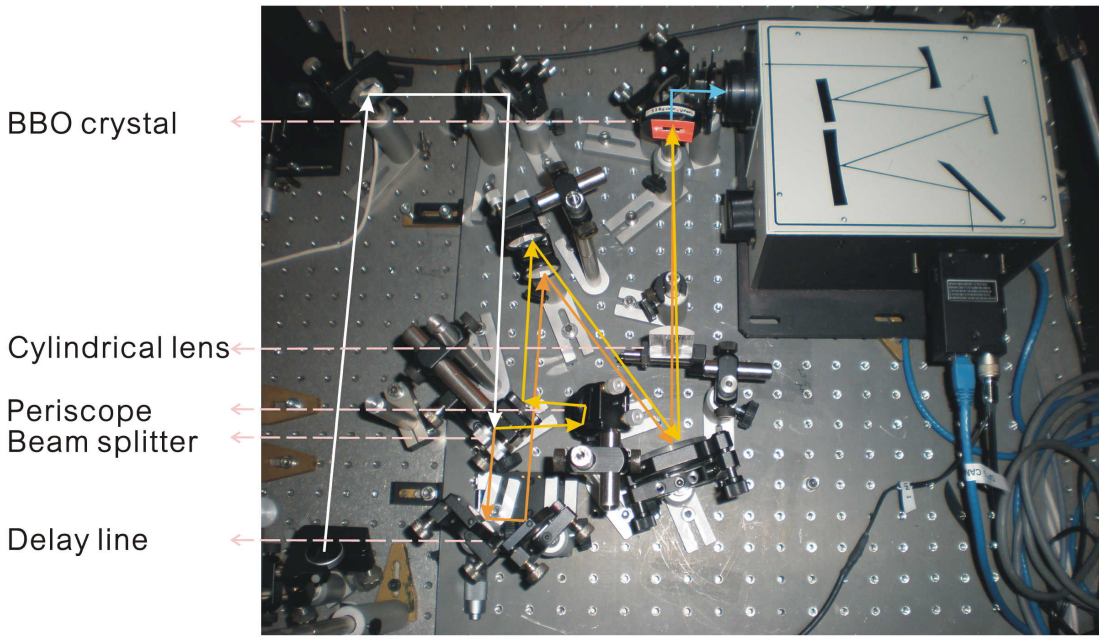

Figure 4.25: A photograph of the homemade FROG setup with the optical path diagram.

mental layout and the detailed alignment procedure will be described.

4.7.1 Experimental setup

The general idea of this experiment is to focus two intense counter-propagating laser beams into a pre-formed plasma channel, whose dual-purpose is to guide the laser pulses over several centimetres and to act as the nonlinear medium for the Raman instability. Stimulated Raman backscattering transfers energy between the frequency components of the laser and plasma waves matching the resonant conditions. Fig. 4.26 illustrates the layout of this experiment with high pump energy level.

The laser beam exiting the main laser amplifier, contains up to 330 mJ of energy and consists of S-polarised chirped pulses with 250 ps FWHM pulse duration, centred at 800 nm with 35 to 40 nm FWHM bandwidth. The laser runs at 10 Hz during the alignment procedure and can be operated at lower repetition rates by using a single shot shutter. When doing the Raman amplification experiment, the laser fires every 5 seconds to allow the gas to be evacuated from the chamber by the vacuum pumps.

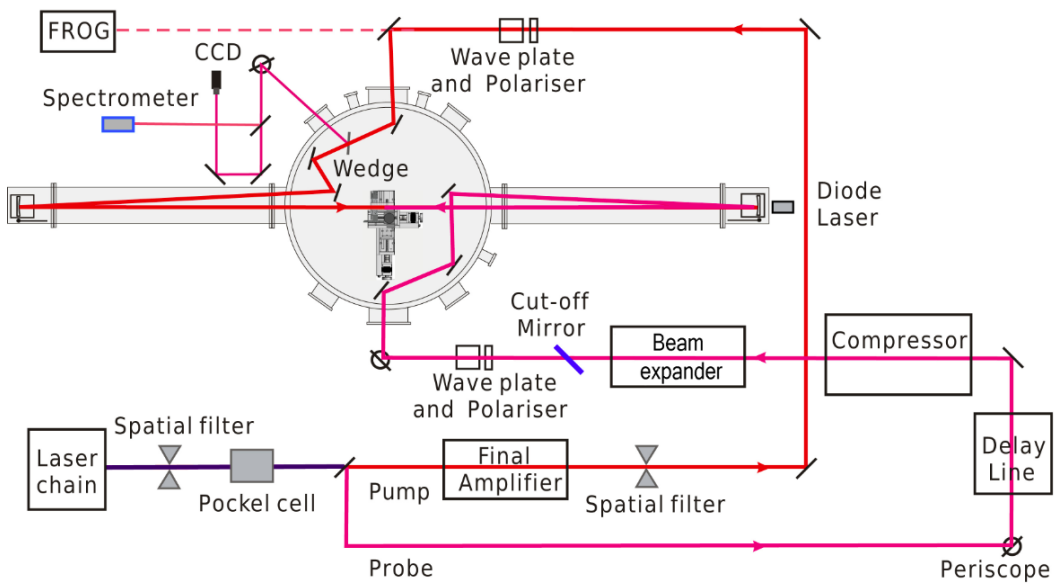

Figure 4.26: Raman experimental layout with high pump energy.

As illustrated in Fig. 4.26, for the high energy level experiment, the laser beam pass through a Pockels cell that is placed just after the main amplifier which has only 3 ns opening time to prevent radiation from coming back to the main amplifier. After the Pockels cell, a beam splitter produces the pump and probe beams with 90% and 10% of the laser energy respectively. The pump and probe beam paths will be discussed in detail in the following sections.

- The pump beam path

After the beam splitter, the pump beam is directed into the final amplifier crystal, which has three pump lasers. The Raman pump beam can be amplified to different energy levels using different combinations of pump lasers for the final amplifier. After being amplified, the maximum output energy achievable is 1.2 J. The pump beam is focused into a purpose made spatial filter to clean unwanted spatial frequencies and add additional protection for the final amplifier from possible back coming radiation. To avoid air breakdown, the spatial filter is mounted in a small vacuum chamber. This chamber consists of a plastic tube and two metal bellows with end windows attached at Brewster angle on each side. A small cone-shaped glass capillary is mounted in the centre of the chamber with the larger radius side facing the beam. This pinhole is

produced by stretching a glass tube and then cutting it in the middle. The laser beam is focused into the narrow side, which has a diameter of 300 μm. The cross section of this stretched glass tube is shown in Fig. 4.27.

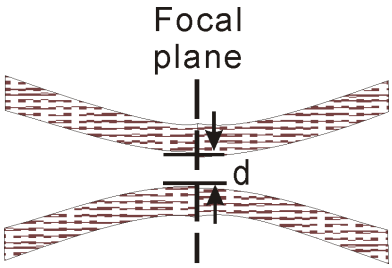

Figure 4.27: Cross section of a stretched glass capillary.

Two plano-convex lenses are placed before and after the spatial filter with 50 cm and 80 cm focal lengths, respectively, to focus and recollimate the pump beam and also to act as a beam expander. The cleaned and expanded pump beam then propagates through a polariser and a quarter wave plate. The polariser transmits the S-Polarised laser beam and the quarter wave plate changes its polarisation from S to circular. After the first set of polariser and quarter wave plate, the pump beam is transmitted into the vacuum chamber. The mirrors used after the wave plate are single stack layer coated to avoid the change of polarisation of the beam.

The pump pulse is focused onto the entrance plane of the capillary in the vacuum chamber by a spherical mirror with a 1.5 m focal length. After interaction, the beam is passed out of the chamber following the probe beam path in the counter propagation direction. On exit, a periscope translates the beam height downwards and rotates its direction by 90 degrees. The S and P components swap in this process, therefore after propagation through a second quarter wave plate the polarisation is rotated to S again. The following polariser, set to reflect S and transmit P polarised light, can dump the out going pump to prevent feedback into the laser system. Due to the depolarisation induced by the lenses in the focusing system, a few percent of the pulse energy propagates through the second wave plate and polariser. Considering the safety of the laser chain, for the high energy experiment, the focusing system is removed and the

adjustment of the pump focus relies on the lens pair before and after the spatial filter.

- The probe beam path

The probe beam, containing 10% of the energy of the main laser beam, first passes through a periscope, which switches the beam polarisation from S to P. An optical delay line is added to controls the relative time delay between the two pulses. The delay line consists of two mirrors mounted on a translation stage controlled by a 'Newport' motion controller. A small compressor compresses the probe pulse down to 60 fs. The pulse duration can be increased to several picoseconds by changing the distance between the grating and mirror (Section 4.2.1). This compressor is purpose-built and the alignment is not straight forward to obtain a very good quality beam without introducing a spatial chirp.

To downshift the central frequency of the probe beam, two methods have been used in this experiment: self-phase modulation in combination with glass filters to downshift the probe frequency (Section 4.2.1) and detuning the compressor grating (Section 4.2.2). In Fig. 4.26, the second method is used.

The compressed and downshifted probe pulse will then propagate through a zoom lens system (Section 4.3) that can be used to adjust the focal spot size and its position. Two cut-off filters just after the focusing system, are set to transmit only low frequency radiation. Following the P polarised probe beam propagates through a polariser and a quarter wave plate. The probe pulse polarisation is first cleaned and then changed to circular before a periscope transmits it into the vacuum chamber. It is then focused onto the other entrance of the capillary.

An optical wedge that has anti-reflective coating on one side to reduce energy loss of the pump pulse, picks 4% of the output probe pulse and reflects it to the diagnostics, a CCD camera and a spectrometer. The rest of the probe leaves the vacuum chamber along the path of the pump beam. Its polarisation is changed to P after a periscope and wave plate, and again ejected by the polariser in the pump path. The ejected probe is transported to the FROG system (Section 4.6.2) for temporal measurements.

Moreover, in order to obtain a left rotating and a right rotating circular polarised beam at the interaction position for the pump and probe beam, respectively, it is necessary to ensure that the number of reflective optics between the wave plate and the capillary for pump and probe path must be an odd number.

4.7.2 Alignment procedure

The alignment procedure in this experiment, including the preliminary set up and the daily alignment routine, is briefly introduced in this section.

- Equal path length check

For a two beam experiment, it is very important to obtain equal path lengths for the pump and the probe pulses to ensure their temporal overlap inside the capillary. The path length of each beam is about 18 m after the beam splitter. The pump pulse passes through an extra amplifier, while the probe passes through a double pass compressor. Since the pump path length is longer, a delay stage is added into the probe line. To check the overlapping of the two pulses, a doubling crystal is placed at the position of the capillary at a small angle. The reflection of the stronger beam and the transmission of the other one propagate roughly colinealy in the crystal. Moving the delay stage until a frequency doubled blue signal is observed indicates that the two pulses are overlapping temporally and spatially in the crystal.

- Polarisation check

As a consequence of the collinear counter-propagating geometry of the two laser beams, both beams will return to the laser chain and may be amplified and damage the laser system. Protection relies on the two pairs of polarisers and quarter wave plates, which have been introduced in Section 4.7.1.

To align the two pairs of polarisers and quarter wave plates, due to the symmetric geometry of the two beams, only one beam is used. Take the pump for instance. The first polariser is placed at an angle that will allow the S polarised input beam to transmit through. To align the first wave plate, a polarising beamsplitter cube (Fig. 4.28)

which separate S and P polarisation in two directions, is placed after the wave plate. Rotating the wave plate and checking the two outgoing beam's energies after the crystal until they are equal will make the beam after the wave plate circular polarised. With this circular polarisation, the pump pulse propagates through the chamber without the capillary in place. Now the crystal is put after the second wave plate to check the energies of the S and P components and the second wave plate is rotated until the circular polarisation is switched to linear, which is perpendicular to the input probe beam. The second polariser is set to eject the output pump pulse. So far the two pairs of polarisers and quarter wave plates are roughly aligned to dump the back coming radiation.

Since the polarisation is not perfectly maintained after interaction with a series of optics between the two wave plates, a pure linear polarisation can not be obtained by the second wave plate. Therefore, minor adjustments are needed to minimise the back coming radiation.

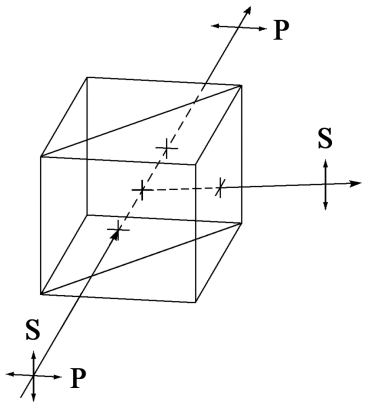

Figure 4.28: Polarising beam-splitter cube.

- Beam and capillary alignment

Aligning the two laser beams from the laser chain to the target chamber and focusing them from opposite directions through the capillary in vacuum is one of the greatest challenges of conducting the Raman experiment. A careful step by step beam alignment procedure is developed for this purpose. This procedure will be briefly presented here.

When setting up the experiment, a series of apertures are placed to reference the beam position before the target chamber. A diode laser is used to mark the axis along which the capillary is placed. The alignment in the vacuum chamber starts from the probe beam and without the capillary in place (it is moved off the beam path with one of the translation stages). In the vacuum chamber, a small rectangular target mounted on a motorised frame that can be remotely moved in and out of the beam path is placed

close to the entrance of the capillary together with a CCD camera monitoring the target. This is used to monitor the beam position and to overlap the probe beam with the diode laser. After being aligned with the diode laser by adjusting the probe spherical mirror, the coarse alignment of the probe beam is completed. The pump is stronger, so it is aligned on the chamber axis using references marked behind the two spherical mirrors.

Part of the probe pulse is picked off and delivered to the diagnostics. The imaging system is set up and calibrated with the CCD camera imaging the a 200 μm slit placed at the input and output planes of the capillary. The camera is translated back and forth until a sharp image of the slit is obtained. With the CCD imaging the entrance, the zoom lens system is adjusted to obtain a matching focal spot size. Then, by moving the camera backward the probe beam at the exit plane of the capillary is imaged. The capillary is finally moved in the beam line and aligned using the 5-axes stage until the probe pulse is transmitted through and at the same position on the CCD camera as without the capillary, which indicates that the capillary is collinear with the probe beam. When the capillary is aligned with the probe, it is kept untouched and used as the reference for fine alignment of the pump beam.

4.8 Conclusion

Laser pulse Raman amplification in capillary waveguide is a very difficult experiment to implement due to the large number of components involved, the required synchronisation and adjustment.

First of all, the laser system presented in Section 4.1 has to supply a high quality, high energy and stable beam. Each step of the production of a suitable (short and frequency downshifted) probe pulse, explained in Section 4.2, needs to be checked to minimise distortion of the laser pulse. As the key component of this experiment, the capillary has to be well designed and coupled to its power system (Section 4.4). To guide the laser pulses through the capillary with high transmission efficiency, matching

the focal spot size (Section 4.3) is also necessary. Timing setting is an other essential requirement, which is described in Section 4.5. The synchronisation of two laser pulses with the plasma, the trigger of the single shot shutter and diagnostic system need to be precisely controlled. Moreover, the custom-built diagnostic system, especially the FROG in Section 4.6 has to be aligned and calibrated.

Chapter 5

Experimental results of Raman amplification in a capillary plasma waveguide

The Raman amplification experiments have been performed for two ranges of parameters: pump pulses of moderate energy interacting with probe pulses spectrally red-shifted via the combination of self-phase modulation and glass filters, and pump pulses of high energy interacting with spectrally filtered probe pulses. In this chapter, the guiding of the pump and probe beams in the capillary is presented first. The dependence of energy and spectral gain on various experimental parameters are than analysed systematically, and their connection with the electron dynamics are discussed. Numerical simulations are performed using a reduced PIC code to enable the interpretation of the experimental results.

5.1 Guiding of laser pulses

A hydrogen-filled capillary discharge waveguide has been employed to guide high intensity laser pulses over longer distances. The guiding mechanism has been reviewed

in Section 2.5.2. As described previously, the capillary in use is 40 mm long and has a 300 μm diameter. According to the measurements performed using Stark broadening of hydrogen lines, the axial plasma density in the capillary is approximately about 1×10^{18} cm^{-3} [108] and the matched focal spot size for the capillary is 55 μm.

5.1.1 Test of capillary guiding

To guide the probe pulse, the capillary's position and angle are finely adjusted to optimise the waveguiding (i.e. guiding just by the capillary wall with no plasma discharge) pattern for high guiding efficiency. Guiding is most efficient when the laser beam passes through the centre of the capillary. Therefore, the optimised pattern usually contains a central spot with a ring or symmetric spots around it, as shown in Fig. 5.1(b). When the waveguiding pattern overlaps with the marked position on the computer screen of the probe pulse without capillary in the beam line, the pulsed valve for the hydrogen gas and the high voltage are then turned on. The discharge is synchronised with the pulsed valve and the probe beam arrival time, and the laser is guided by the plasma channel in a single mode. Results of a guiding test are presented in Fig. 5.1, where (a) is the probe beam focus with spot radius of 55 μm, (b) is the laser profile at the exit of the capillary showing a characteristic waveguiding pattern and (c) is the output laser profile with plasma channel guiding containing 85% of the input energy at the focus.

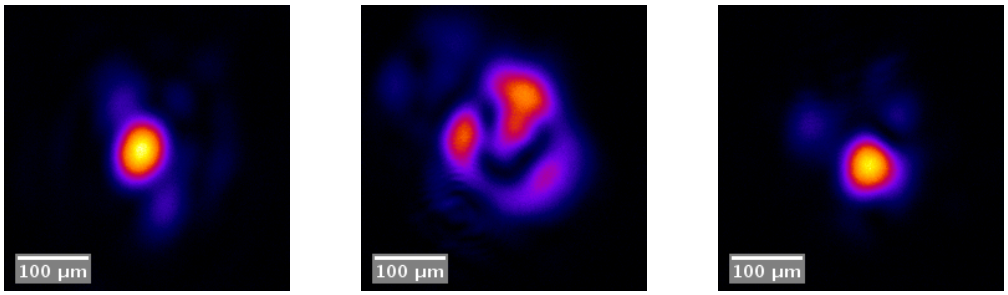

(a) Probe focus (b) Waveguiding (c) Guided probe

Figure 5.1: Images of the laser beam at the entrance and exit of the capillary.

The transmission efficiency is defined as the percentage of the laser energy obtained

from the capillary output compared with the energy contained in the focal spot. It is calculated automatically with an image batch processing program that first finds the pixel with the maximum counts in the image, and then with that pixel as the centre it integrates the counts of the pixels within a certain radius (usually set to the capillary radius). Laser energy loss is dominated by inverse bremsstrahlung absorption in the guiding process at low intensity.

The capillary is then left untouched and it is used as the reference for fine alignment of the pump beam. Similar guiding results are obtained for the pump, which are omitted here.

5.1.2 Relative time delay between the discharge current and the laser pulse

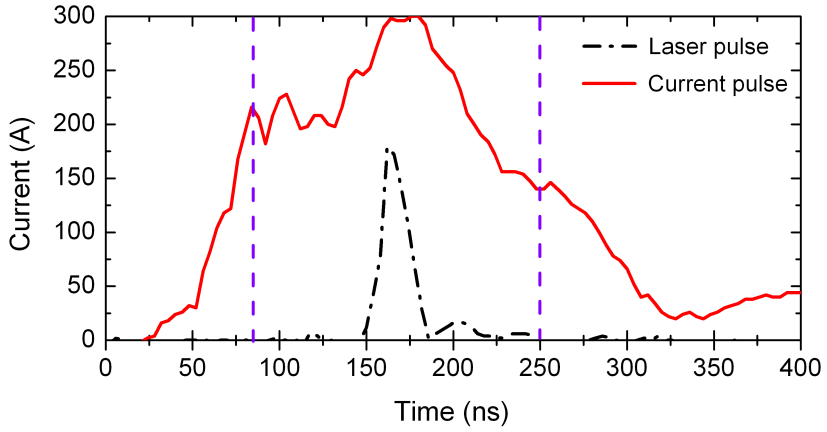

Figure 5.2: High voltage discharge current pulse and the synchronised laser signal shown for the region of high transmission efficiency.

To guide laser pulses through the capillary, the timing of gas injection, high voltage discharge and laser pulse are required to be synchronised. As described earlier in Section 4.5, the relative delay is controlled by a Stanford pulse generator. The pulse valve for gas injection opens for 200 ms before the striking of the discharge, which allows sufficient time for gas distribution in the capillary. The transmission efficiency

is studied as a function of the time delay between the striking of the high voltage discharge and the arrival of the laser pulse. Fig. 5.2 shows the timing of the laser signal picked off by a photodiode with the synchronised discharge current trace as the reference. The region between the two vertical dashed lines, which has an approximate width of 170 ns, is where transmission efficiency is high ($\sim 80\%$).

After the test of guiding, the next step is to find the temporal overlap (i.e. the zero delay) between the two pulses in the plasma channel by scanning the delay stage.

5.2 Amplification results - scanning the delay stage

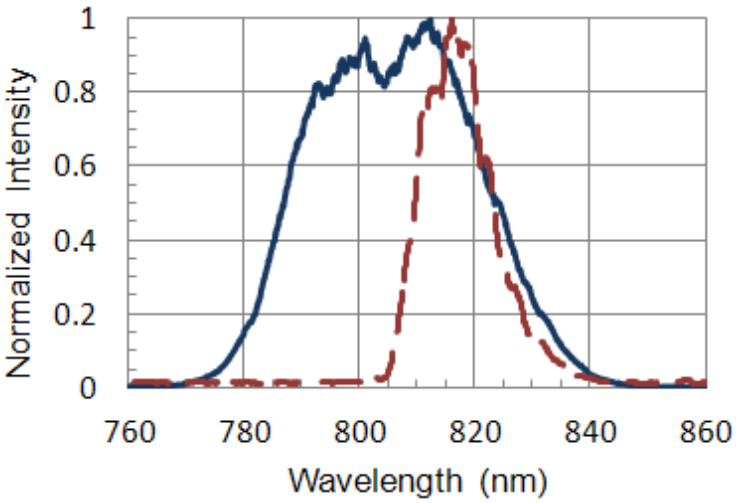

Figure 5.3: The normalised spectra of pump (solid line) and probe pulses (dash line).

As a first step, the temporal overlap of the pump and probe pulses in the plasma channel should be found prior to the high gain amplification experiment. For this reason, only moderate pump energies are used in the experiment. The pump pulse wavelength is centred at 805 nm and has a FWHM temporal duration of 250 ps with an on target energy of 445 mJ. To simplify the experimental operation, filament generation is not employed, instead the probe spectrum is modified by realigning the compressor to cut wavelengths shorter than 805 nm. Therefore, the probe spectrum is centred at 818 nm and is about 80 fs long with the energy of 1.3 mJ. The normalised spectra of

the pump and probe pulses are shown in Fig 5.3.

With these parameters, the Raman amplification process remains in the linear regime. The dependence of the amplified probe energy, spectrum and pulse duration on the relative time delay between the two pulses are presented in the following sections. These results can not only be used to check the right position of the translation stage for the zero delay but also help us to study the development of the Raman amplification process with a long chirped pump pulse and a short probe pulse in a plasma waveguide channel.

5.2.1 Energy gain measurements

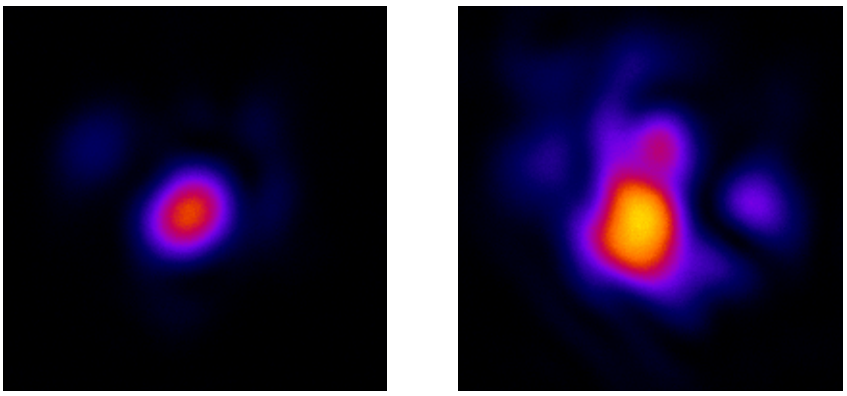

(a) Guided probe pulse (b) Amplified probe pulse

Figure 5.4: (a) Image of the guided probe pulse through the capillary. (b) Image of the probe pulse with 240% amplification by the pump pulse.

The amplification experiments are firstly attempted with the translation stage at a position where the two beam paths are checked to have the same length with the doubling crystal. We first discuss the energy measurements. After the probe pulse propagates through the capillary, a small portion of the beam is split off and transmitted to the diagnostic system by an optical wedge. A 50:50 beam splitter transmits half of the beam onto a CCD camera via a lens to monitor the laser spot shape and the energy gain, while the other half is reflected to a spectrometer. The camera (*FL2-14S3M-C*) has a 1/2" sensor with 1360×1024 active pixels and is used together with a $\times 4$ magnification imaging system. The pixel size is 4.65 μm$\times$ 4.65 μm.

The measured energy gain with the translation stage set at different positions indicates that the temporal overlap of the two pulses in the plasma channel is achieved. Fig. 5.4 shows the CCD measurements of (a) a guided probe pulse through the capillary and (b) an amplified probe pulse with 240% energy gain. The energy gain is defined by $G = (E' - E)/E$, where E' and E are the integrated counts calculated from the images with and without the presence of the pump beam, respectively.

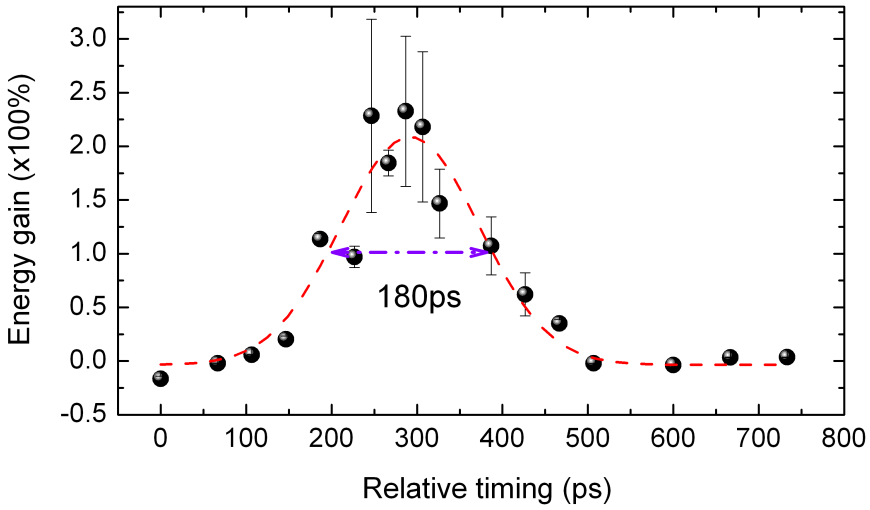

Figure 5.5: Probe energy gain plotted as a function of the relative delay time between the pump and the probe pulses, compared with a Gaussian fitting curve (with on target energy of 445 mJ for the pump and 1.3 mJ for the probe, and pulse durations of 250 ps and 78 fs, respectively).

By adjusting the translation stage position and repeating the Raman amplification experiment under the same conditions, we obtain a set of measurements of the probe energy gain for different time delays between the two pulses, which are plotted in Fig. 5.5. Here, the value of E' is the best amplified shot for the given conditions, whereas E is the average of the five best guided shots without pump present. The error bars shown in the figure are the standard deviation of E.

To better understand Fig. 5.5, it is necessary to clarify that the point where the relative delay is equal to 0 corresponds to the time when the probe arrives at the entrance of the plasma channel and starts to interact with the higher frequency components at the

back of the pump pulse (arbitrary zero point) as it exits the capillary. Positive delays correspond to translation stage positions where the probe path length becomes shorter and the interaction starting point moves towards the pump's entrance. It is also worth noting that when the path length changes by L, the interaction position changes by $L/2$. The various stages of two pulses interaction within the plasma channel are shown schematically in Fig. 5.6.

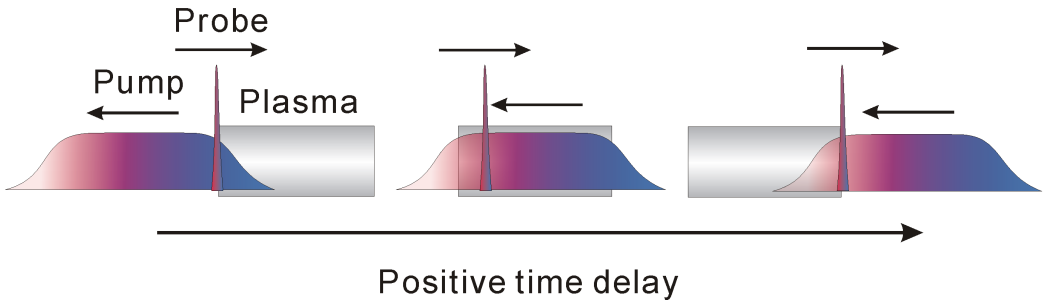

Figure 5.6: Interaction situations with positive time delay between the two pulses. For the three situations depicted here, the probe pulse interacts with only the back part of the pump, the whole pump and only the front part of the pump pulse, respectively.

The gain is up to 2.4 times and the amplification ($G > 0$) occurs for about 400 ps. A Gaussian fitting curve is made on the energy gain versus the relative time delay. The width (FWHM) of the Gaussian fitting curve is 180 ps, which corresponds to a 10.8 cm path length change and is determined by two factors: (1) the length of the plasma channel and (2) the duration of the pump pulse.

Fig. 5.7 (a) shows the case where the probe pulse arrives at the entrance of the capillary while the pump is about to exit the channel. This corresponds to the start of the overlap of the two pulses in the plasma channel when scanning the delay stage (i.e. the 0 relative delay). Fig. 5.7 (b) shows the opposite case where the probe pulse exits the capillary, only interacts with the front of the pump pulse and after this no gain can be observed. To compare the situation (a) with (b), Fig. 5.7 (c) shows the translation stage at the same position as (b) but at a time when the pump pulse is leaving the capillary. In the time from situation (b) to situation (c) the pump pulse propagates over 11.5 cm (the pump pulse length plus the capillary length), therefore the probe should

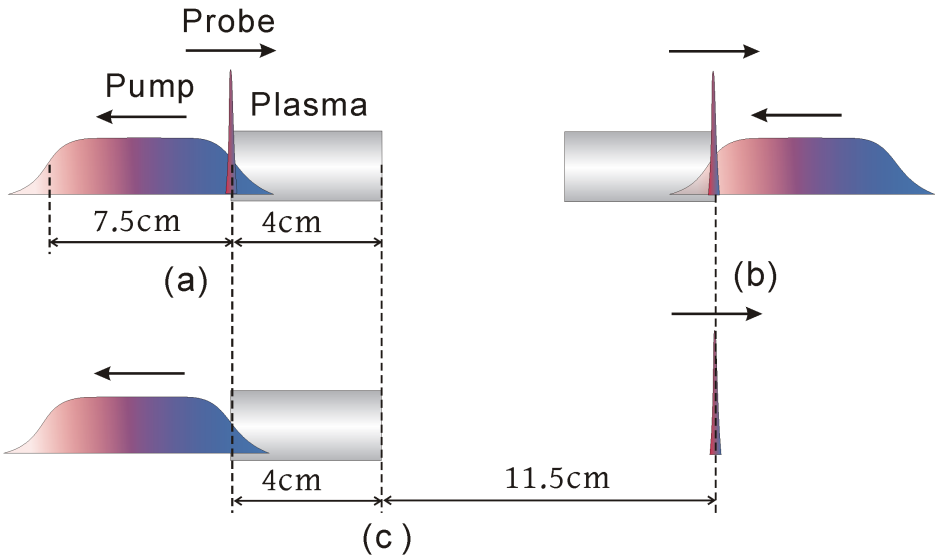

Figure 5.7: (a) Probe pulse at the capillary entrance interacting with the back of the pump pulse. (b) Probe pulse at the output of the capillary interacting with the front of the pump pulse. (c) The equivalent situation of (b) with the pump at the same position as (a). Here the laser pulse length is given by its FWHM.

travel the same distance. Thus, comparing (a) and (c), it can be seen that the delay range of the probe pulse for observing the Raman gain is limited to the pump pulse length plus twice the capillary lengths, which is 15.5 cm. Here the laser pulse length is given by its FWHM.

The experimental measurement (10.8 cm) is shorter than the theoretical predicted distance (15.5 cm), which can be explained by (1) the plasma density drops at both edges of the capillary and (2) the filtered probe spectrum limits the range of pump frequencies that are resonant with the probe pulse. This can be seen more clearly in the spectral analysis.

5.2.2 Spectral analysis

Following the discussion of energy gain calculated from the CCD camera, the next step is to study the frequency dependence from a spectral analysis. As described earlier, a small part of probe signal is picked off in the chamber and focused onto a spectrometer. This spectrometer (Ocean Optics *USB 4000*) is equipped with a 1200 grooves per mm

grating and has a spectral range from 653 to 947 nm. The recorded signals $I(\lambda')$ and $I(\lambda)$ are the probe spectra with and without the pump pulse present, respectively. These can be used to obtain the spectral gain as a function of wavelength: $G(\lambda) = (I(\lambda') - I(\lambda))/I(\lambda)$.

Varying the delay between the two pulses, the short probe pulse will interact with different parts of the positively chirped pump pulse, as illustrated in Fig. 5.6. The initial pump and probe spectra are shown in Fig. 5.3. The amplified probe spectra and the gain curves as a function of the time delay are shown in Fig. 5.8(a) and Fig. 5.8(b) respectively. All spectral graphs have the same scaling of the ordinate in Fig. 5.8(a).

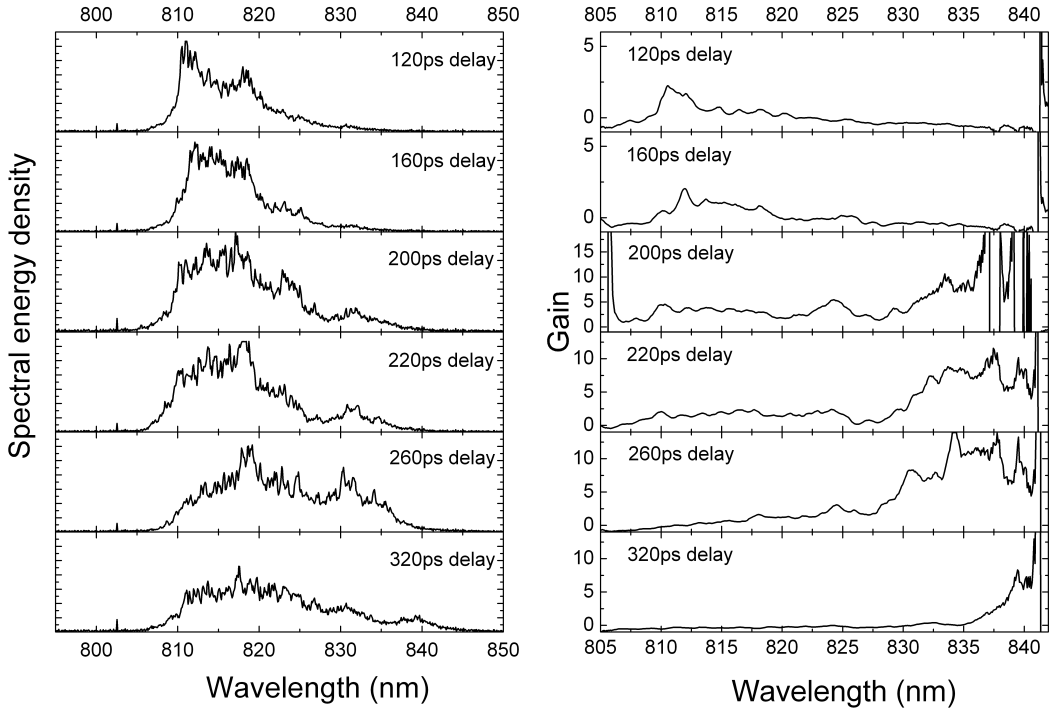

(a) (b)

Figure 5.8: Measured spectra (a) and gain curves (b), of the amplified probe pulse for different pump-probe delays.

With positively increasing time delays, the probe arrives at the capillary earlier and encounters the front of the pump pulse (lower frequency components). The change in frequency of the amplified probe reflects the chirp of the pump pulse through the Raman process. As can be seen in Fig. 5.8(a) and Fig. 5.8(b), the amplified spectra and

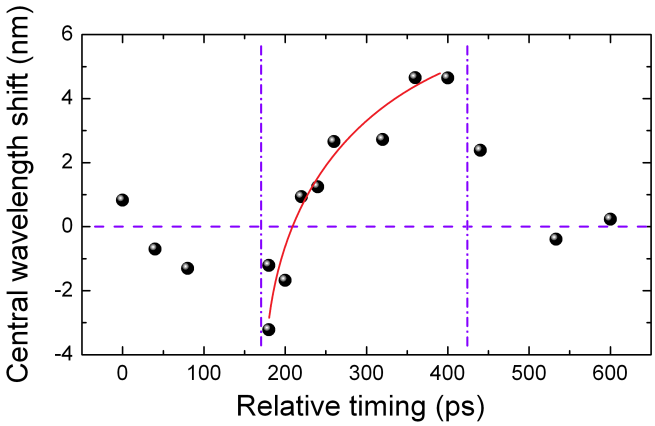

Figure 5.9: The shift of the amplified probe central wavelength (centre of mass of the spectrum) as a function of the relative time delay. The two vertical dash lines mark the region where significant energy gain is obtained.

the gain curves shift to longer wavelengths with positive time delays.

To present the data of Fig. 5.8(a) in a more intuitive way, the shift of the central wavelength of the amplified probe pulse versus the time delay is plotted in Fig. 5.9. The central wavelength is calculated as the centre of mass of the spectrum. Substantial energy gain of the probe pulse is observed when the time delay is between 170 ps and 425 ps, as can be seen in Fig. 5.5. Therefore, paying attention to this area marked between the two dashed lines in Fig. 5.9, the amplified probe central wavelength shifting from shorter wavelengths (negative shift) to longer wavelengths (positive shift) is a direct consequence of gradually stronger amplification of the probe lower frequencies. When the probe only interacts with the front or the back of the pump pulse, as shown on both sides of Fig. 5.9, due to the low initial intensity of the frequency components in resonance, the central wavelengths of the amplified probe fail to reflect the resonance with the frequency component of the pump.

According to Fig. 5.5, Fig. 5.8, and Fig. 5.9, we can roughly divide the scanning process into two regions: (a) before 260 ps and (b) after 260 ps. In region (a), the probe starts to interact with the back of the pump and with positive time delays it encounters with more frequency components where resonance can occur until the whole probe bandwidth gets amplified. It is worth noting that it is not necessary for the probe to interact with the whole pump to obtain full bandwidth amplification due to the overlapping of their spectra. At the end of region (a), with all the frequencies amplified, the

total energy gain reaches its highest value. The gain for longer wavelengths is larger than for shorter wavelengths, as shown in Fig. 5.8(b), because the resonant components of the pump for longer wavelength are more intense. Moreover, at shorter wavelength, the probe can lose energy to the pump through the reverse Raman process. With increasing delays, the probe pulse interacts with more pump frequency components that are not resonant with the probe, thus the total energy gain remains constant. In region (b), the probe begins to not overlap with the front of the pump, and therefore higher frequencies can not be amplified, which results in a drop of the total energy gain.

Following the spectral analysis of the experimental results, the next step will be to present the FROG measurements that have been applied to Raman amplification for the first time.

5.2.3 FROG measurements

In addition to the CCD camera and the spectrometer, a FROG system has been employed to detect the change of the probe pulse temporal profiles before and after amplification. The FROG principle and setup have already been introduced in Section 4.6.2. However, to extract the laser pulse information from the measured signals, pulse-retrieval software is also required.

Two FROG related programs have been used to process the data: (1) Femtosoft *FROG* is a standalone retrieval algorithm, which cannot process experimental data in real time, but contains a powerful set of features and algorithms. (2)Femtosoft *QuickFrog* is a program that continuously reads data from the camera and displays the results in real time. With *QuickFrog*, laser beam parameters can be checked when tuning the laser or doing experiments. The *FROG* program is used to reprocess important data off-line.

QuickFrog can be operated in two modes: (1) Time Mode, where the measured 2D trace and the retrieved trace as well as the pulse intensity and the phase as a function of both time and wavelength are displayed on the screen, as shown in Fig. 5.10. The

saturation level of the signal on the detector and the results including temporal and spatial FWHM together with the FROG errors are also available. (2) In Space Mode, the FROG algorithms are disabled and simple spatial profiling is available. This mode is used for aligning the FROG setup, as well as for obtaining basic information on the spatial profile of laser pulses.

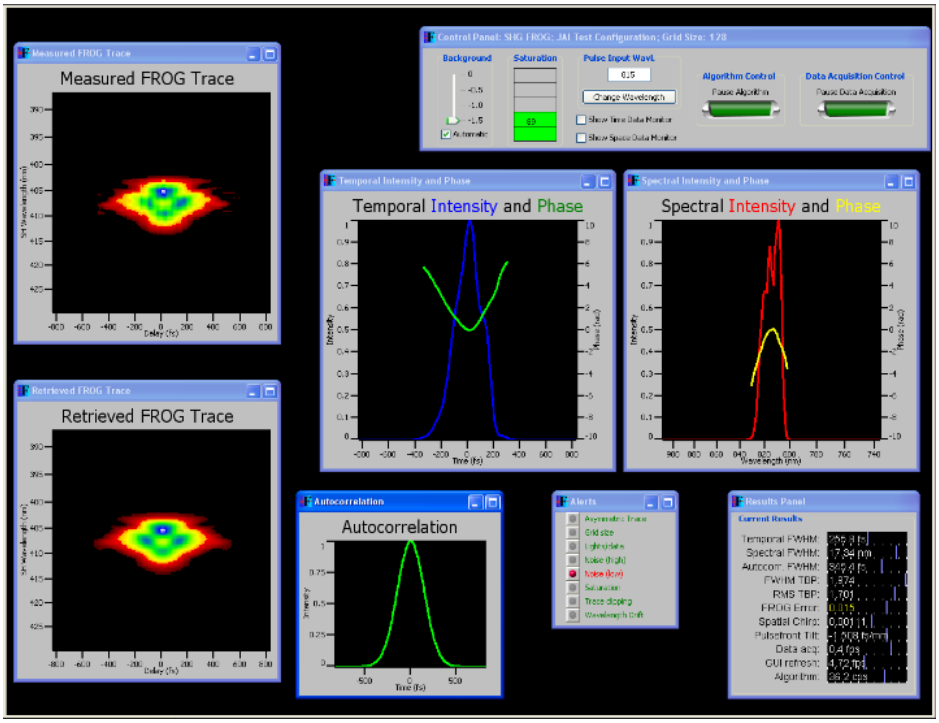

Figure 5.10: The program panel of *QuickFrog* in the Time Mode.

Before presenting the temporal profiles obtained from the FROG measurement, it is necessary to point out the limitations when the FROG is used in this experiment, for future improvements. First of all, the data processing programs only works at 8 bit. As a result of the limited dynamic range, not all the measurements can be used to retrieve a FROG trace because sometimes the signal can saturate the detector and often it is too weak. As a result, setting up a proper filter by gauging the amplified signal strength is essential when operating the FROG system. Secondly, the probe pulse transmitted through the capillary always has a tiny angular offset. After several meters of propagation, not all the shots are transmitted perfectly to the detector and some develop an asymmetrical shape producing a large FROG error. Therefore, running

the *FROG* program off-line again to reprocess the data enables us to get more usable results. To overcome these limitations, a new version of the processing program that can support cameras with larger dynamic range is required. Then, the stability of the laser and the experimental setup can be improved.

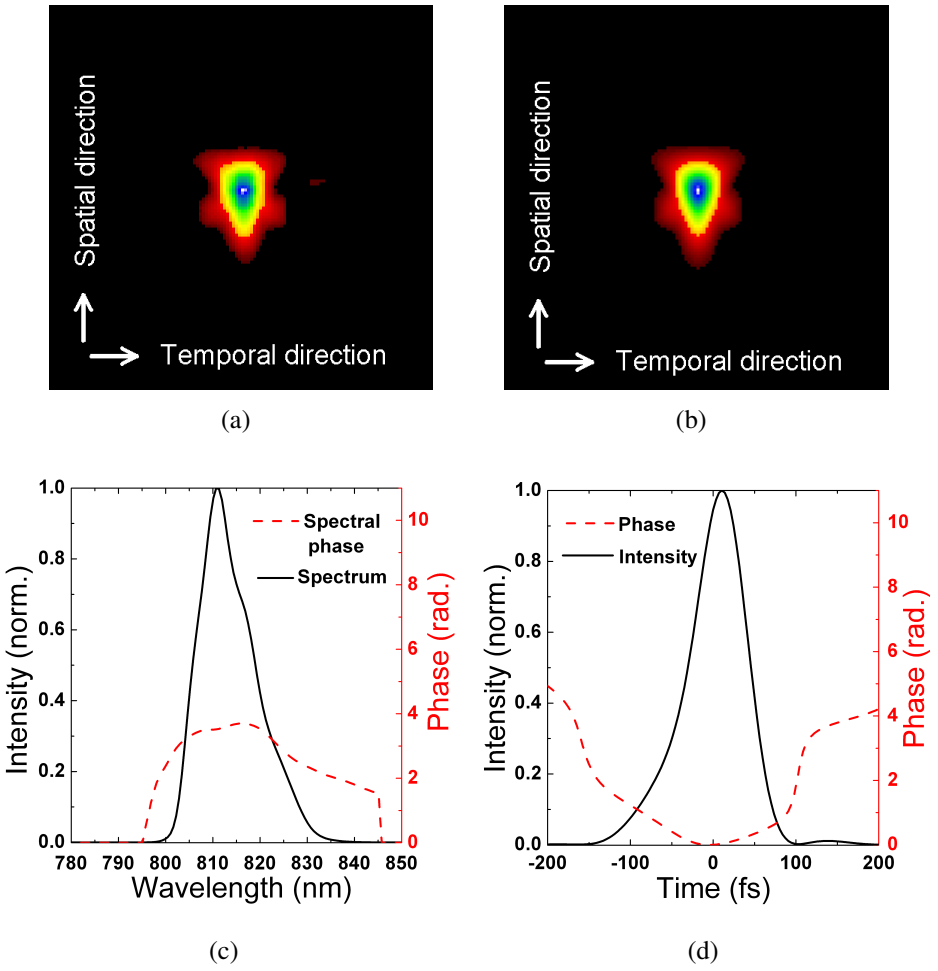

Figure 5.11: A FROG measurement of a capillary guided probe pulse: (a) the measured FROG trace, (b) the retrieved FROG trace (reprocessed by the *FROG* program), (c) and (d) the retrieved spectral and temporal profile and their respective phases.

Fig. 5.11 and Fig. 5.12 are typical FROG measurement results, including (a) FROG trace recorded using the 8-bit CCD camera and (b) retrieved FROG trace, (c) and (d) the retrieved pulse intensity and phase in the frequency and time domains, respectively. The vertical axis of the FROG trace corresponds to the wavelength while the horizontal axis is time. The spectral and temporal width of the laser pulse are measured by the FWHM. Fig. 5.11 shows the probe pulse which after being guided through the capillary

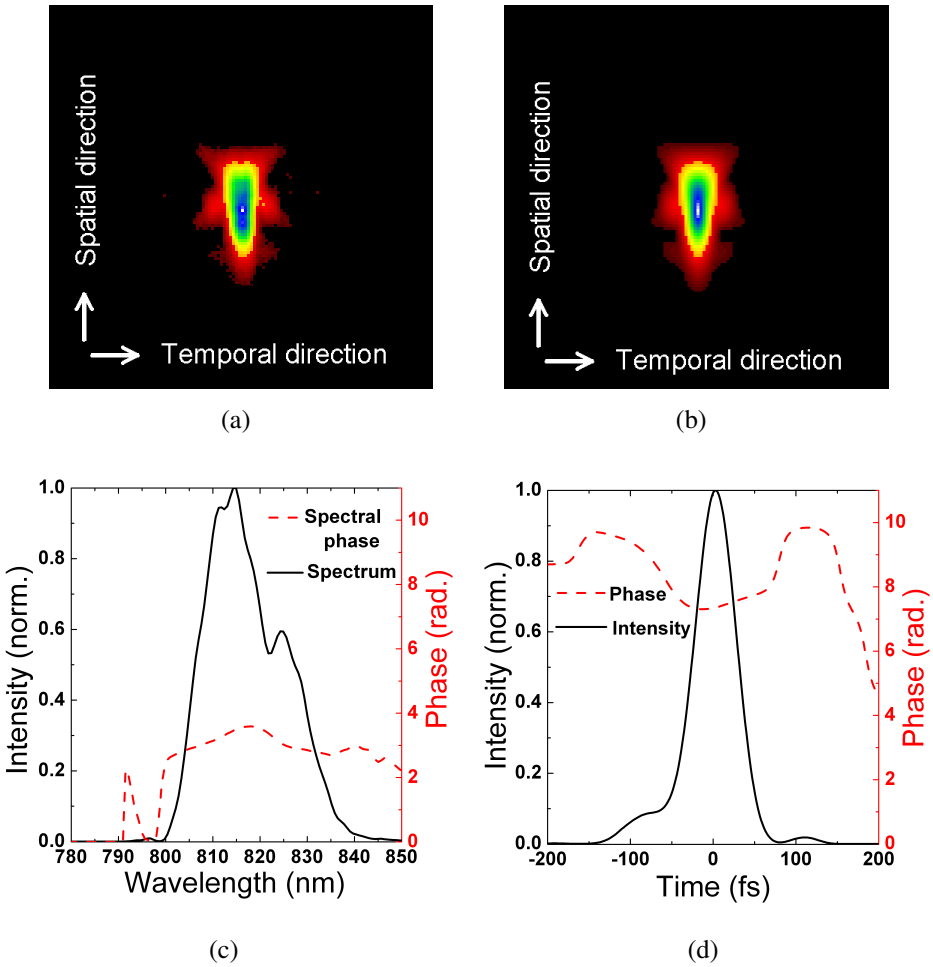

Figure 5.12: A FROG measurement of a probe pulse with amplification: (a) the measured FROG trace, (b) the retrieved FROG trace, (c) and (d) the retrieved spectral and temporal profile with their respective phases.

has a pulse duration of 115 fs, while Fig. 5.12 presents the amplified probe with a shortening of its duration to 96 fs. These results are reprocessed off-line to minimise the FROG error. The pulse intensity depends on the efficiency of second harmonic generation, the pointing, filters etc. therefore can not be used to obtain the gain value.

The measured pulse duration and spectral bandwidth with different time delays between the two pulses are summarised in Fig. 5.13. Focusing on the region where significant energy gain is obtained (between the two dashed lines), we can see that the pulse duration decreases and the bandwidth increases with the positive time delays. Together with the energy and spectral gain versus the time delay, Fig. 5.13 can help to reproduce the history of the probe pulse evolution.

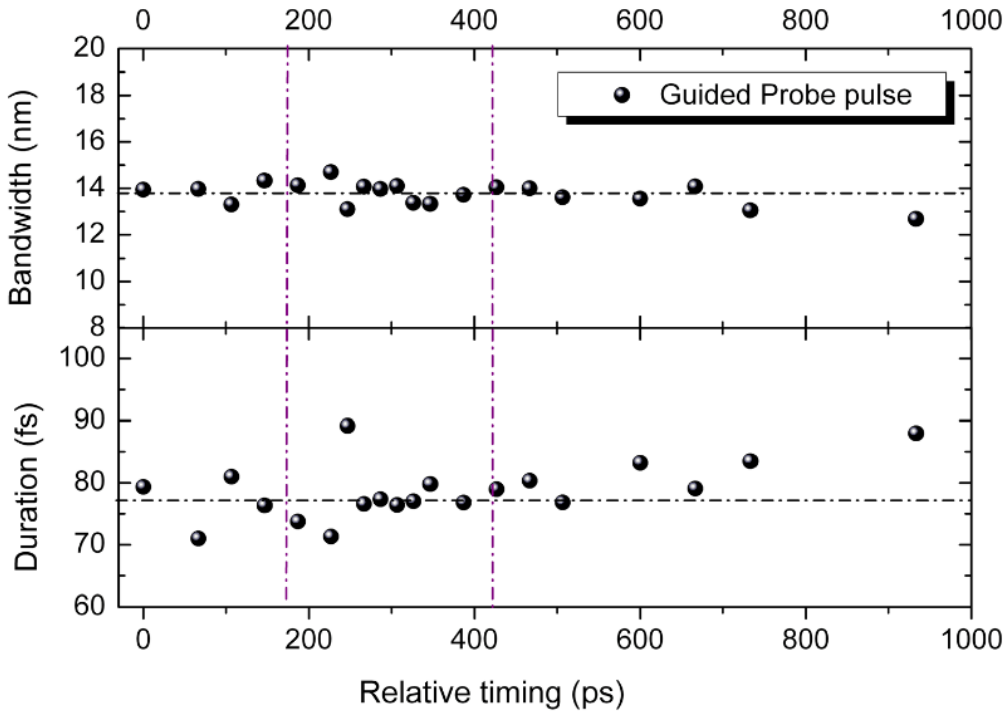

(a)

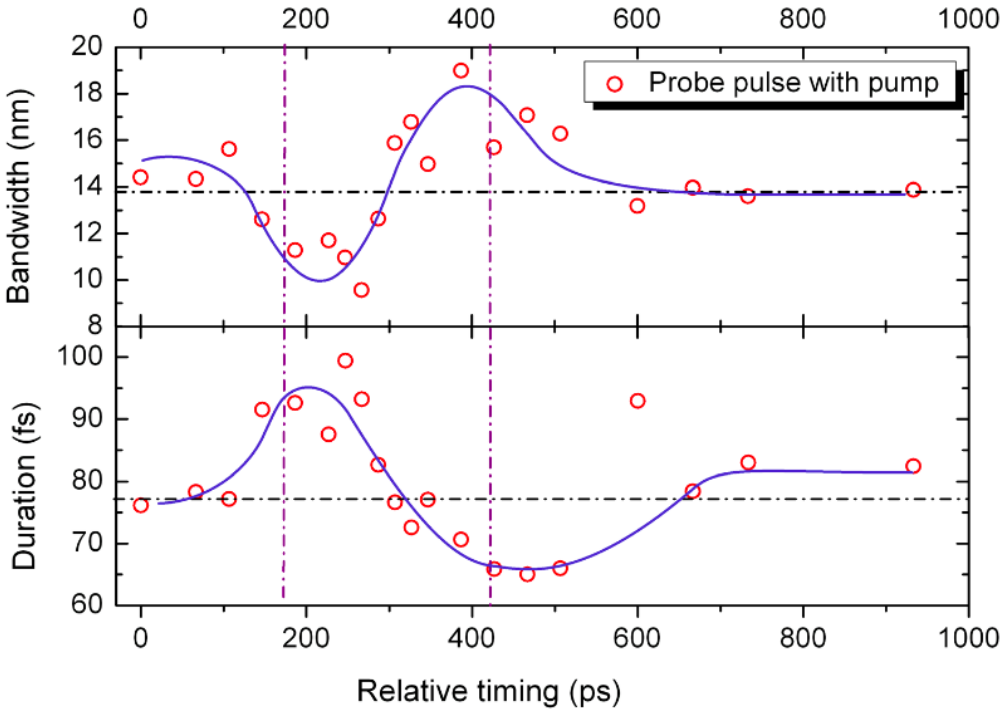

(b)

Figure 5.13: The probe pulse spectrum bandwidth and pulse duration without (a) and with (b) amplification obtained from the FROG measurements are presented as a function of different time delays. Between the two vertical dashed lines is the region where significant energy gain is obtained.

In theory, when interacting with a chirped pump pulse in the linear regime of Raman amplification, the probe pulse duration should remain more or less constant, if its whole bandwidth gets amplified with a similar gain. However, with different time delays, the probe interacts with different parts of the chirped pump pulse (see Fig. 5.6), therefore, only frequencies in resonance will be amplified. On the other hand, even when the whole probe bandwidth is amplified, in practice, the spectral gain curve usually is not flat due to different frequency components having different amplitudes, which leads to a variation of the spectral and temporal profile of the amplified probe pulse.

For example, at time delay of 160 ps, a typical set of FROG measurement are presented in Fig. 5.14, from which we can see that the amplified probe spectral phase remains roughly the same, while the spectral intensity profile is deformed due to a strong partial amplification at shorter wavelengths, around 810 nm, which is consistent with the spectrometer measurements in Fig. 5.8(a). The spectral variation leads to a narrower bandwidth and a longer pulse duration.

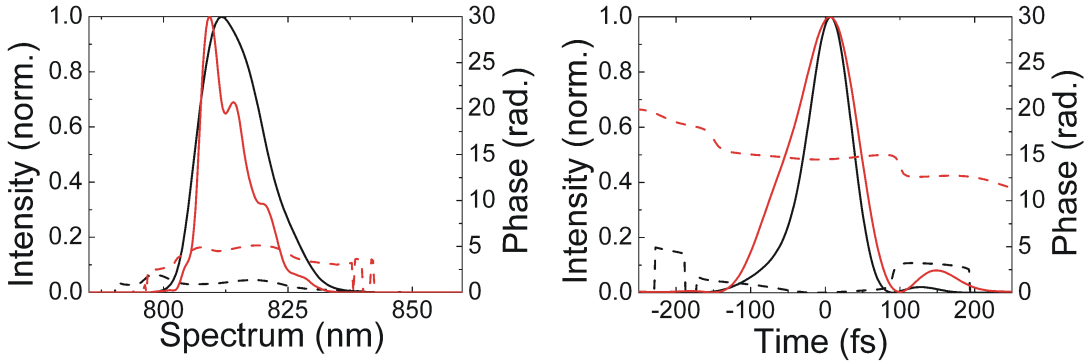

Figure 5.14: FROG measurement of probe pulse spectrum intensity and temporal intensity profile before (black solid line) and after (red solid line) amplification with phase (dash lines) at time delay of 160 fs.

As higher probe frequencies (shorter wavelengths) move out of resonance, the longer probe wavelengths experience large amplification because their resonant components of the pump are relatively intense. As shown in Fig. 5.15, at time delay of 380 fs, strong amplification of the low frequency probe with initially low intensity deforms

its spectrum in a way that leads to a larger bandwidth and a shorter pulse duration at FWHM, as expected from the Fourier relationship.

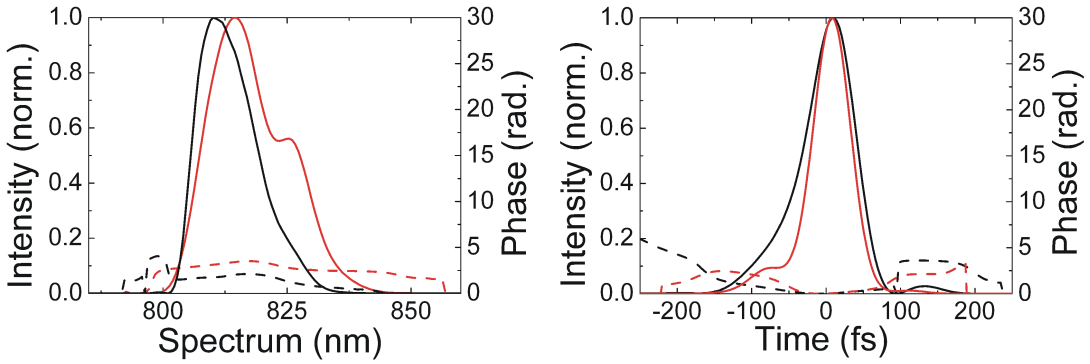

Figure 5.15: FROG measurement of probe pulse spectrum intensity and temporal intensity profile before (black solid line) and after (red solid line) amplification with phase (dash lines) at time delay of 380 fs.

To summarise, in this section, the energy gain, spectral gain, central frequency shift and the changes in bandwidth and pulse duration are studied. The asymmetry of the changes of the spectral bandwidth and the pulse duration with the scanning of the delay stage are due to the probe pulse frequencies being not sufficiently downshifted from the pump frequency by the plasma frequency, as shown in Fig. 5.3.

5.3 Amplification of red-shifted probe pulses

After the spatial and temporal overlap of the pump and probe pulses are assured, amplification of frequency red-shifted probe pulses is performed. The implementation of this experiment becomes immensely complicated when employing self-phase modulation to generate the frequency shifted probe pulse. Since the filamentation is a process that is very sensitive to the input signal parameters as well as the alignment, the probe spectrum is not stable. One way to handle this problem is to combine the nonlinear process of the probe pulse passing through the glass window of the filament generator with a relatively weak filamentation process. The probe and the pump spectra are shown in Fig. 5.16. The shifted probe wavelength is centred at 840 nm with a

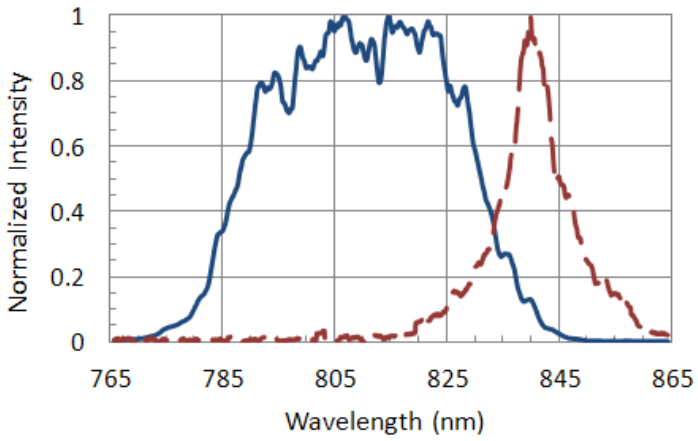

Figure 5.16: The normalised spectra of pump (solid line) and red-shifted probe pulses (dash line).

bandwidth of about 11 nm. With the probe signal at the optimal frequency, a series of measurements have been carried out varying different parameters, such as the backing pressure in the capillary, pump energy, probe pulse duration etc. The results are presented and discussed in the following sections.

5.3.1 Energy measurements

- Energy gain dependence on pump energy

The experiment is carried out with increasing pump energy from 100 mJ to 330 mJ with the focal spot size of 65 μm. The probe pulse contains 0.5 mJ with 200 fs pulse duration, which is the optimal parameters for filament generation. The delay stage is set to maximise energy amplification. As expected, the output probe energy increases strongly with the pump energy. The best energy gain of the probe pulse as a function of the normalised vector potential of the pump pulse is plotted in Fig. 5.17. An exponential fit (1-D theory) of the data is added to compare with the theoretical gain curve. A plasma density of 1×10^{18} cm^{-3} is taken to calculate the theoretical gain. The measured gain is lower than the theoretical value due to several factors:

• The narrow gain bandwidth in the Raman linear regime results in only part of the pump spectrum (see Fig. 5.16) utilised for probe pulse amplification.

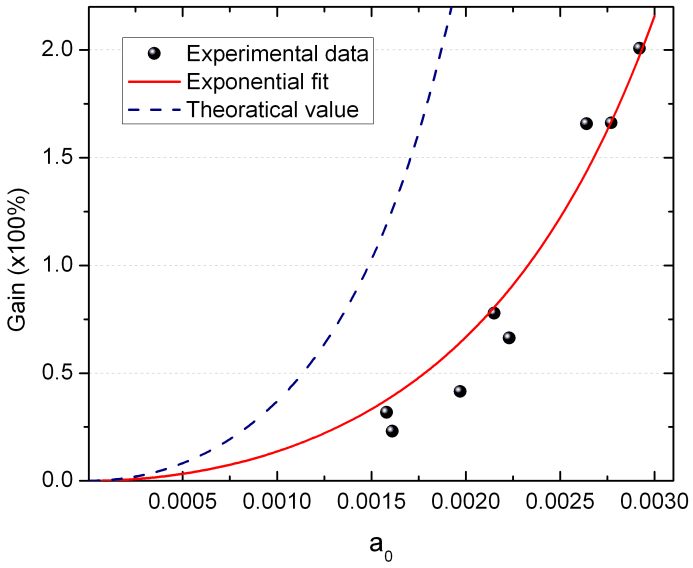

Figure 5.17: Experimental energy gain with exponential fitting and a theoretical gain curve.

• The pump energy loss during propagation in the capillary is not taken into account. The guiding efficiency is about 80%.

• The gain value is calculated with the evaluated peak intensity of the pump pulse. However, taking the mode structure into account (i.e. 3-D effect), the pump intensity is less on the side, therefore when integrate the gain it will be lower than if the calculation is based on peak intensity.

• Thermal effects and other nonlinear detrimental effects are not taken into account.

From the energy measurements, no tremendous gain boost is observed compared with the experiment of the probe pulse without filament generation. Fig. 5.17 indicates that the amplification process remains in the Raman linear regime.

- Energy gain dependence on electron plasma density

The experiment is also performed with increasing backing pressure and hence increasing plasma density. As shown in Fig. 5.18, the energy gain increases with the electron plasma density, as expected. The error bars indicate the statistical deviation of the best

5 shots. As reflected in the gain expression, the growth rate γ depends on the electron plasma density n_e ($\gamma \propto \sqrt{n_e}$), since the pump and probe pulses are coupled via the plasma wave, a larger number of electrons leads to a larger energy transfer from the pump to the probe and the plasma wave. However, when the pressure is too low or too high, the three waves will out of resonance and decrease the gain.

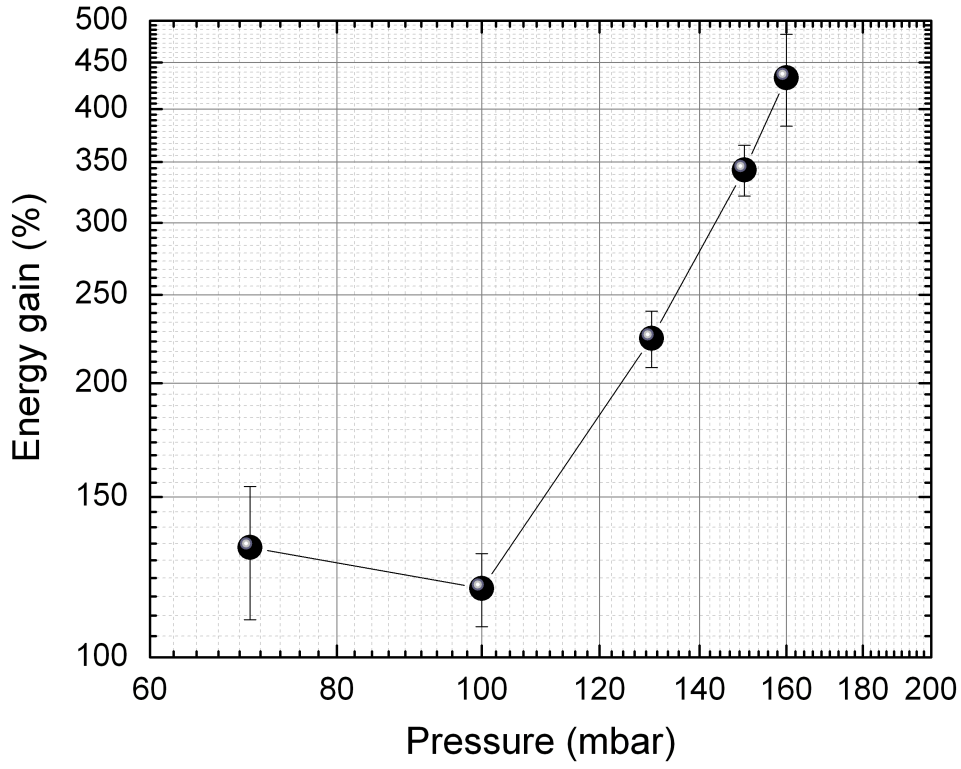

Figure 5.18: Energy gain with backing pressure.

The measurements suggest that with higher plasma densities, the energy gain can be increased dramatically. However, practically, the capillary can not work with densities higher than 2×10^{18} cm^{-3}. With the increasing backing pressure in the capillary, the high voltage discharge encounters difficulties ionising the gas and hence causes problems operating electronic devices. It is worthwhile emphasising that the aim of this work is not to obtain the highest gain but rather to investigate Raman amplification in plasma, and furthermore, use the relatively low plasma density and high pump and

probe amplitude to test the properties of the Compton regime.

5.3.2 Spectral measurements

For the spectral measurements, no significant spectral broadening is observed. However, the spectra show a special feature, which can be seen in Fig. 5.19. There are narrow peaks on top of the amplified spectrum which is not seen for experiments without filament generation. Spectra in one batch of measurement share the same features including the number and the positions of the peaks. These peaks might be caused by the degraded probe pulse quality in the filament generation process or due to chirp and phase modulation.

In order to improve the pulse quality, the probe pulse is further stretched to about 250 fs before going through the filament generator. However, the already complicated operation gets more difficult to generate red-shifted spectral components. With central wavelength shifted to 820 nm, the energy gain does not improve.

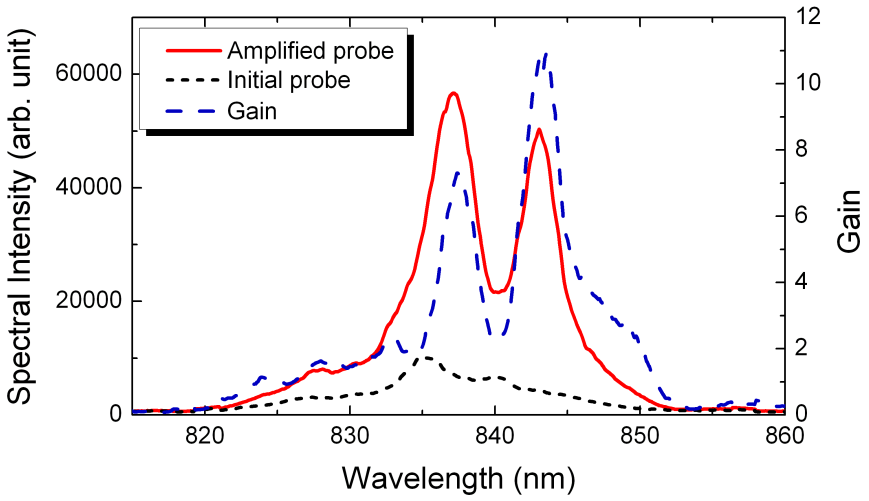

Figure 5.19: Spectra of the probe pulse with (red solid line) and without (black short dashed line) the amplification and the gain curve (blue dashed line). Both the probe spectra are smoothed by the average of adjacent 20 points. The energy gain for this shot is 250%.

5.3.3 Conclusion

Within the frame of this work, the laser pulse Raman amplification is expected to reach its optimal regime associated with high energy gain. However, as a direct consequence of the mutual restraints of the laser pulse character for the generation of filament and the capillary guiding, the signal quality cannot be assured. To reduce the operational complexity of the experiment when employing the full power of the laser, the decision was made to go back using the compressor and cut-off mirror instead of the filament generator to shift the probe pulse central frequency.

5.4 High gain measurements and gain saturation

The conclusion drawn from the previous section, where the filamentation is identified as a limiting factor for energy gain improvements, advises us to generate the probe pulse by cutting the high frequency components with the compressor and the cut-off mirror. As a result, the probe central wavelength is only slightly longer than that of the pump pulse, which reduces energy transfer from the probe to the pump, however, not all the pump frequencies can be utilised for probe amplification. The optimal laser frequency versus various plasma densities can be checked in Fig. 4.10.

Moreover, with the Pockels cell for Raman experiment installed (refer to Section 4.7.1) for additional protection for the laser chain, the full laser energy of 1.6 J is used for the pump beam. Taking all the losses into account, the highest on target pump energy is about 840 mJ. With the large range of pump pulse energies, the amplification experiment is performed with different parameters for investigating the evolution of the Raman amplification process. The difficulty in carrying out high pump energy experiments is the unavoidable leakage of the pump pulse transmitted through the wave-plate and polariser, which will be focused and, when too severe, could damage the optics in the experimental setup. A series of rigorous checks are required to ensure the safety of the Raman experiment optics and the laser itself.

5.4.1 High gain measurement and spectral broadening

- Energy amplification

With the parameters listed in Table 5.1, the best energy gain of 650% is obtained and the images of the probe pulse with and without amplification are shown in Fig. 5.20. The optical quality of the amplified pulse remains acceptable. No filamentation instability and severe deformation in shape are found.

	Pulse duration (FWHM)	On target energy	a_0	Focal intensity
Pump pulse	250 ps	825 mJ	3.9×10^{-3}	3.2×10^{13} Wcm^{-2}
Probe pulse	250 fs	0.9 mJ	5.0×10^{-3}	5.0×10^{13} Wcm^{-2}

Table 5.1: Experimental parameter for the highest gain measurement.

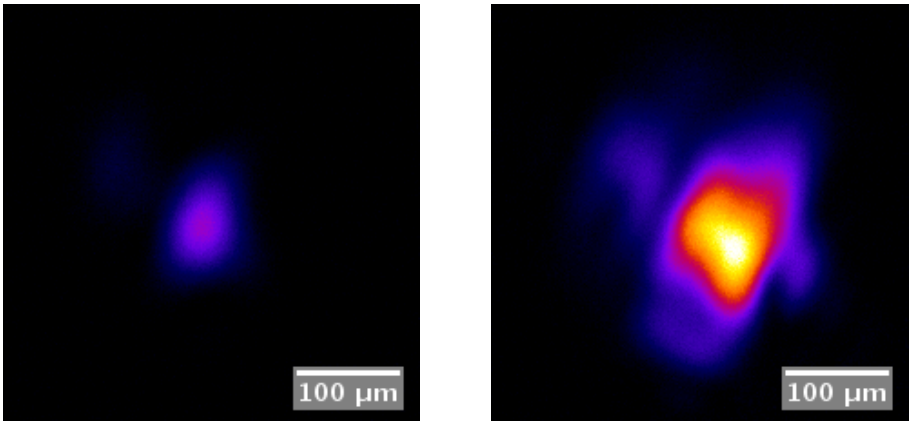

(a) Guided probe pulse (b) Amplified probe pulse

Figure 5.20: Images of the probe pulse at the exit of the capillary with best energy gain.

Fig. 5.21 shows the spectrum intensity normalised with the energy gain measured from the CCD camera. A clear spectral broadening can be observed, especially on the high frequency side. A peak is formed between 800 nm and 810 nm. A further investigation of spectral broadening will be presented in the following section.

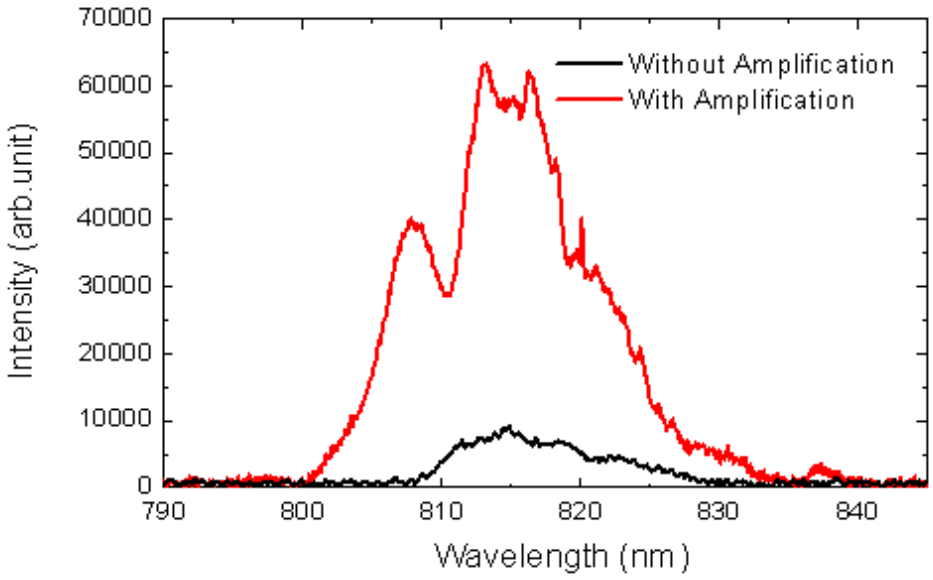

Figure 5.21: Spectra of the probe pulses with and without interaction of the pump pulse. The spectral intensity is normalised according to the energy gain taken by the CCD camera.

- Spectral broadening

Spectral broadening of the probe pulse after Raman amplification is observed, especially on the short wavelength side. As illustrated in Fig. 5.22, more than 50% bandwidth increase is achieved for this shot. The figure also shows the integrated spectral energy distribution curve, which indicates that the amplified pulse has 10% of its energy distributed in the new frequencies on each side of it. The spectral gain curve shows a relative low value at the centre, compared with the two peaks at both sides. This special gain feature is associated with most of the shots having large energy gain and indicates that nonlinear effects are becoming more important.

The measured spectral broadening could be a consequence of spectrum profile deformation or the emergence of new frequencies or a combination of these two. The broadening due to the appearance of new frequencies is an indication of reaching the Compton regime, where the ponderomotive force of the beat wave is sufficiently strong to cause the electrons to undergo synchrotron oscillations in the optical lattice and the pulse compresses to π/ω_b, where ω_b is the bounce frequency.

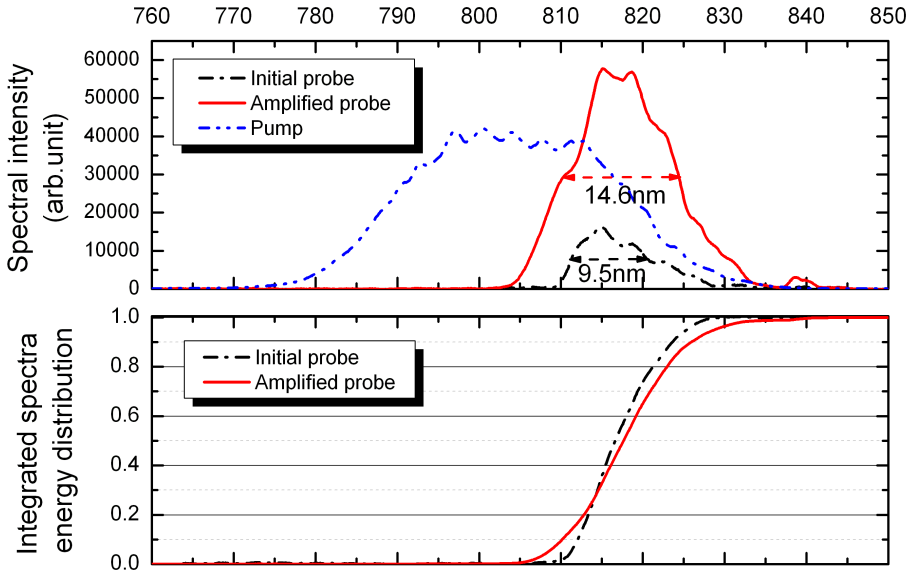

Figure 5.22: Spectra of the probe pulses with and without the amplification. The bandwidth increases from 9.5 nm (FWHM) of the initial probe pulse to 14.6 nm for the amplified probe pulse. The pump spectrum is measured from the scattered radiation from the laser chain, thus providing information about the spectral separation between the pump and probe pulses. Integrated energy distributions of the spectra for the initial and amplified pulses show that about 20% of the energy of the amplified pulse is contained in both sides of the spectrum.

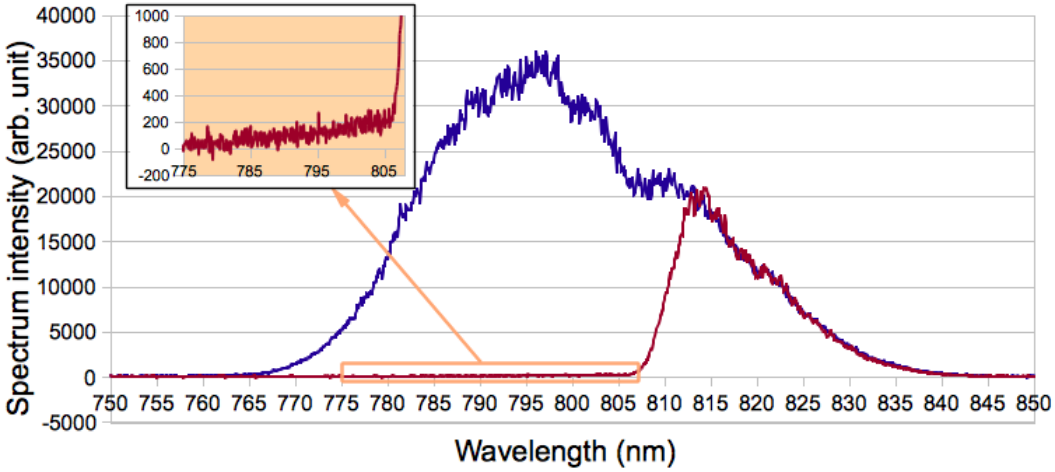

Figure 5.23: Probe pulse spectra before (blue line) and after (red line) the compressor.

To identify the origin of the spectral broadening, a close look at the probe pulse spectrum is required. The measured probe spectra before and after the compressor are shown in Fig. 5.23. It is observed that a small signal exists between 795 nm and 807 nm. If this is real, the bandwidth increase on the blue side of the amplified probe pulse could just be gain saturation of the small signal existing there. However, the gain curve does not match the gain profile calculated from the pump. It is more likely that the probe signal between 795 nm and 807 nm is an artefact of the spectrometer due to scattering inside the box and grating. Therefore, the spectral broadening is due to the appearance of new frequency components on the amplified probe pulse, which suggests that the amplification process is gradually changing from Raman amplification to the nonlinear regime.

In many amplified probe spectra, the amplification on the high frequency side is much stronger than at other frequencies, as can be seen from the peak between 800 nm and 810 nm in Fig. 5.21 and Fig. 5.24. To explain this phenomenon we need to look at the electron motion as discussed in Section 3.2.3. Before the ponderomotive force dominates the electron motion, it starts by trapping some low energy electrons causing them to undergo synchrotron oscillations. As trapped electrons are accelerated in the plasma-wave potential, the plasma wave loses energy to compensate, and undergoes a frequency downshift [109]. A lower plasma frequency results in a blue shift of the amplified probe pulse spectrum.

The probe pulse duration is not obviously compressed as observed in FROG measurements, since the electrostatic force due to space charge still dominates the electron oscillation and even in the pure Compton regime the pulse compression scales with $\tau \sim 1/z^{1/2}$, which is a slow process.

In this experiment, the calculated bounce frequency is $\omega_b = 2.1 \times 10^{13}$ rad s^{-1}, which is still lower than the plasma frequency $\omega_p = 5.6 \times 10^{13}$ rad s^{-1}, however the increasing ponderomotive force is still able to trap a significant number of electrons. This can be defined as a transition regime [87] between the Raman linear and the Comp-

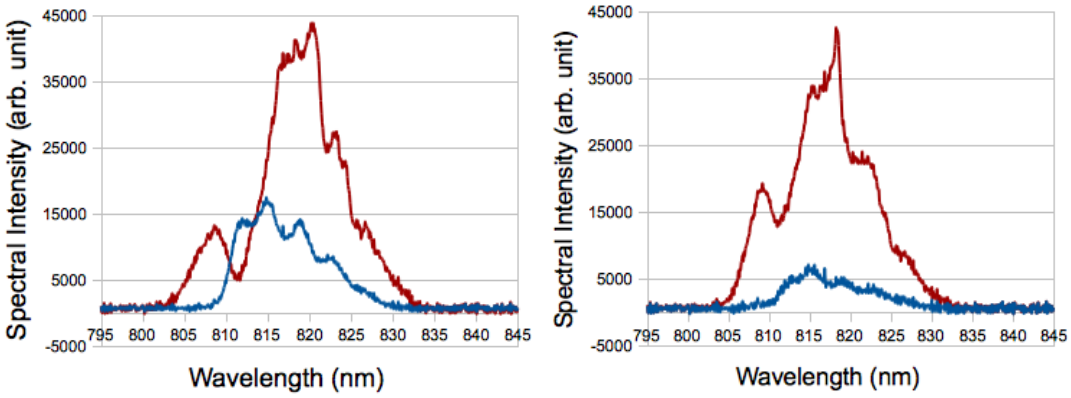

(a) (b)

Figure 5.24: Initial (blue) and amplified (red) probe spectra with strong amplification at high frequency side for two cases.

ton regime, in which the plasma behaviour dominated by collective effects transforms to behaviour determined by single particle dynamics, i.e. the Compton regime. It is worth noting that the calculation of the bounce frequency is just a rough estimation of the simplified scenario [77].

Special feature

Apart from the broadening of the amplified spectrum, there is also a small bump that appears at wavelengths around 837 nm, which can be seen clearly in Fig. 5.25, as well as in Fig. 5.21 and Fig. 5.22. Fig. 5.25 shows that approximately 10% of the energy of the amplified pulse is contained in the small bump, which is shifted by approximately $2\omega_p$ with respect to the pump central frequency. Moreover, the profile of the small bump is very similar to the main pulse. In the Compton regime, it is possible to have sidebands separated by ω_b. However, the dynamics of the electrons are still not dominated by the ponderomotive force.

In this experiment, if the plasma wave is strongly driven, the nonlinearities give rise to electron oscillations at frequency of $2\omega_p$. Therefore, the amplification of these frequency components can also be the backscattering of the pump from the harmonics of the plasma wave. It is difficult to identify the origin of this feature experimentally,

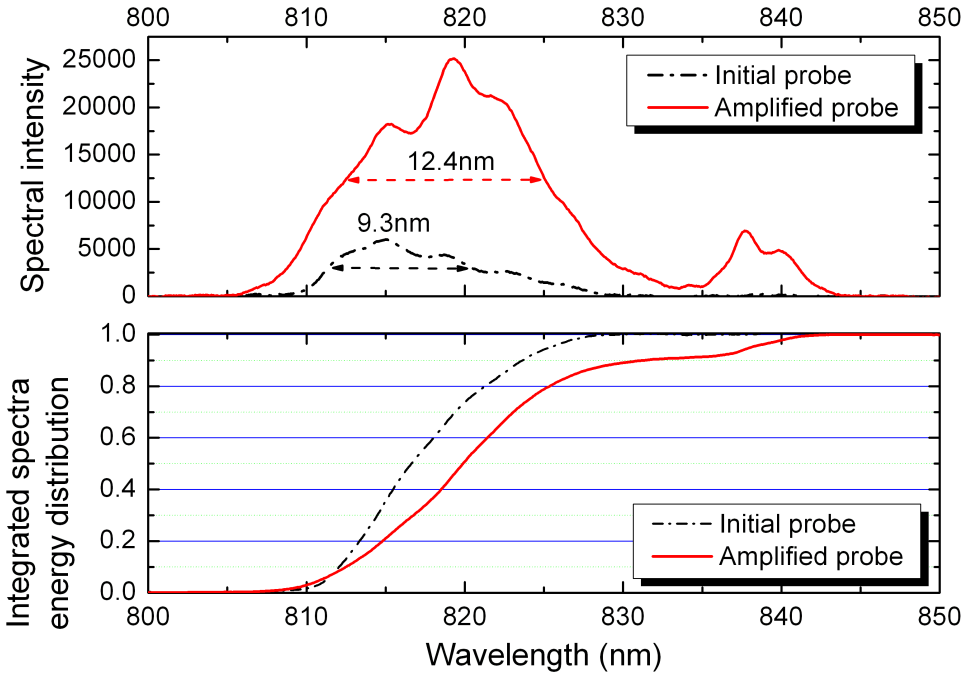

Figure 5.25: Spectra of the probe pulses with and without amplification. In addition to the bandwidth broadening from 9.3 nm (FWHM) to 12.4 nm after amplification, there is a large amplification between 835 nm to 843 nm. Integrated energy distributions of the spectra show that about 10% of the energy of the amplified pulse is contained in this wavelength range.

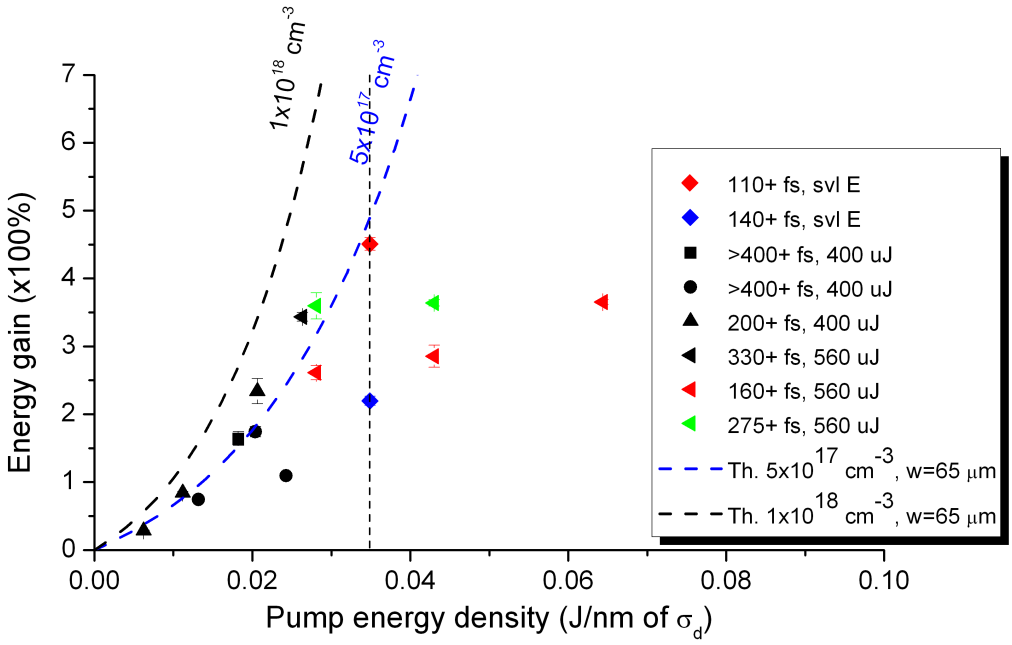

Figure 5.26: The probe pulse energy gain as a function of the pump pulse spectral energy density with different probe pulse chirp rate ("svl E": several energy, "+": positively chirped probe pulse, "-": negatively chirped probe pulse).

therefore 1D aPIC simulations are performed and the harmonic components are found through Fourier transform of the plasma wave (details are given in Section 5.5) which indicates the pump backscattering on the harmonics of the plasma wave contributes to the small bump on the probe lower frequency side.

5.4.2 Energy gain saturation

When increasing the pump pulse energy, more shots with large energy gain are obtained, as expected. However, beyond a certain threshold, probe energy gain saturation is observed. Fig. 5.26 demonstrates the best probe energy gain for each set of experimental parameters as a function of the pump pulse energy density. The spectral energy density of the pump pulse is calculated by dividing the pulse energy by the standard deviation of its spectrum. The motivation of using spectral energy density is to obtain a plot with the pump power to remove the uncertainty in spectral bandwidth or pulse duration.

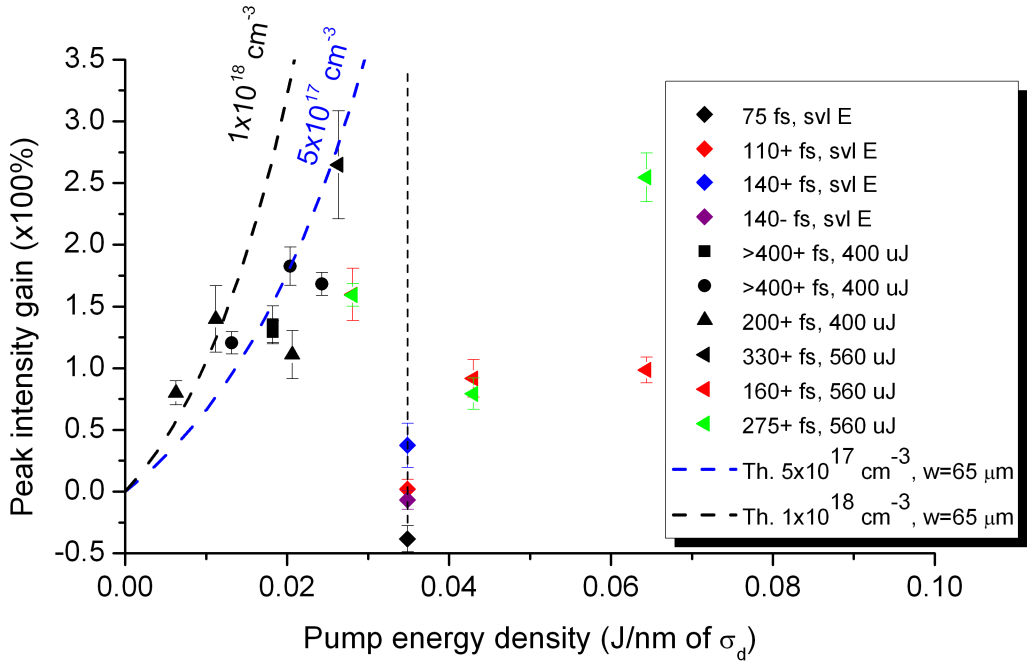

Figure 5.27: The probe pulse intensity gain as a function of the pump pulse energy density with different probe pulse chirp rate ("svl E": several energy, "+": positively chirped probe pulse, "-": negatively chirped probe pulse).

Fig. 5.26 exhibits a two-stage feature. In the first stage, the probe energy gain increases with pump energy density following an exponential increase. When the pump pulse energy density achieves 0.035 J/nm, the second stage is reached, where the probe energy gain does not change much with increasing pump energy.

The two-stage feature is also demonstrated in Fig. 5.27, which shows the relationship between the pump spectral energy density and the probe pulse intensity gain. The intensity gain is measured by comparing the peak intensity of the probe pulses before and after amplification. It is easy to establish that the boundary separating the two stages here is at the same position as the one in Fig. 5.26.

Moreover, measurements of the bandwidth change of the amplified probe pulse as a function of the pump pulse energy spectral density, as shown in Fig. 5.28, reveal a decrease followed by an increase. It is clear that the point separating the bandwidth change from decreasing to increasing is the same as the point dividing the two stages in both Fig. 5.26 and 5.27.

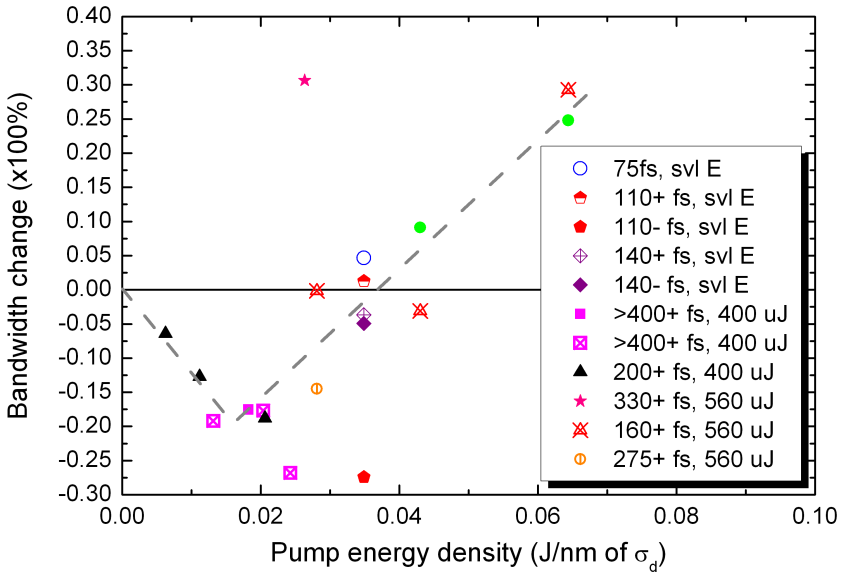

Figure 5.28: The probe pulse bandwidth change as a function of the pump pulse energy density with different probe pulse chirp rate ("svl E": several energy, "+": positively chirped probe pulse, "-": negatively chirped probe pulse).

Fig. 5.26, 5.27 and 5.28 all show a two-stage feature with the same threshold separating the two stages. In the second stage, the probe pulse energy and intensity saturation with increasing pump energy together with the broadening of the bandwidth indicate the onset of plasma nonlinearities.

The parametric instabilities in the nonlinear regime is extremely complex and has not been completely understood. There are several mechanisms that could affect the growth. Referring to the discussion in Chapter 3, it is likely due to the combination of two types of nonlinear effects: wave-wave and wave-particle interactions. As discussed in the previous section, one possibility is that the ponderomotive force starts to drive electron motion. The two-stage feature appears since the gain becomes lower in the transition regime. Other possibilities for the gain saturation are thermal effects. These can cause plasma wave breaking and in that case the plasma wave will not scatter in proportion to the force driving it. Although the transition to wave breaking of uniform plasma waves in cold plasma has been well defined, in a thermal plasma the transition is less obvious and entering the wave breaking regime is more gradual as

a function of the density and temperature [110]. Again, with the help of aPIC simulations, the dominant effect can be determined. From the simulation results, particle trapping are seen only when with high energy pump while the plasma wave breaking also occurs when using moderate pump energy. Therefore, the particle trapping might be the main factor causing the gain saturation.

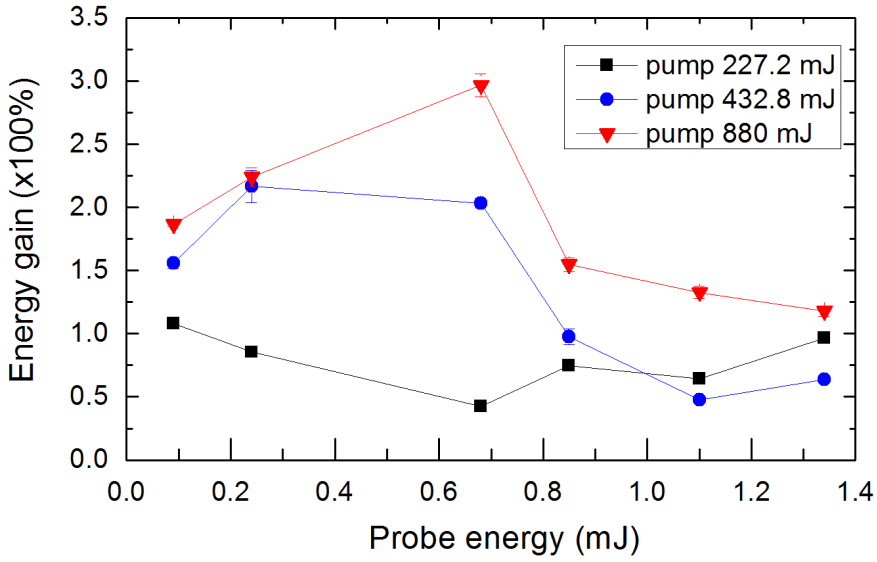

Figure 5.29: The probe pulse energy gain as a function of the probe and pump pulse energy.

The conclusion that the ponderomotive force starts to play an important role in the amplification process can also be verified by the measurements of the Raman gain with different probe pulse energies, since the ponderomotive force is proportional to the product of the stimulated backscattered and the pump field amplitude. The change of the probe pulse energy is realised by setting the polariser at different angles. The positively chirped probe pulses has 170 fs pulse duration before interaction and varies between 150 to 250 fs after the interaction.

As shown in Fig. 5.29, with low pump energy (227.2 mJ in the figure) the Raman gain is independent of the probe pulse energy, as predicted by the theory. However, with higher pump energies (432.8 mJ and 880 mJ), the gain decreases with the increasing probe pulse energy. No evidence is found for deterioration of the pulse quality with increasing energy, so the amplification limit originates from the interaction process.

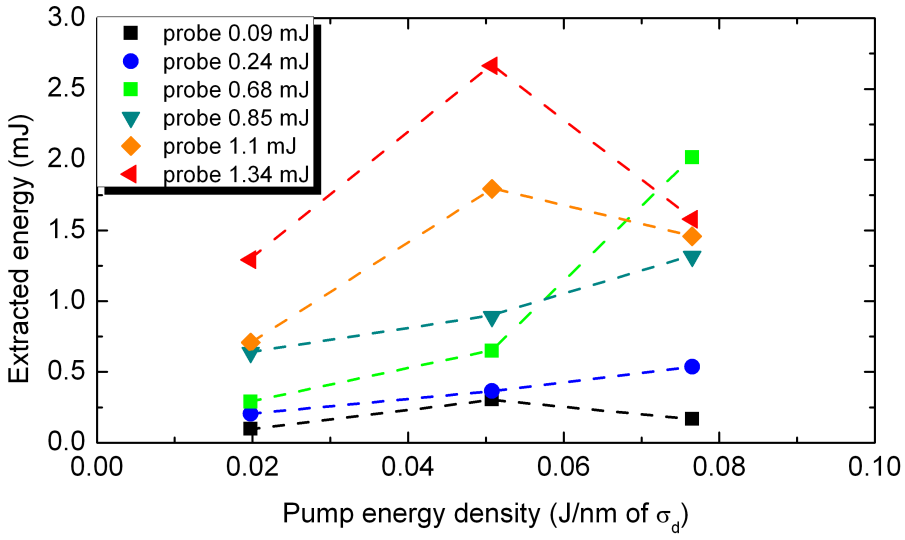

Figure 5.30: The energy extracted from the pump pulse as a function of the probe energy and pump pulse spectral energy density.

The scan of probe pulse energies allows the ponderomotive force to be varied without affecting other nonlinear processes. Therefore, the mechanism that saturates amplification is likely to be electron trapping by the ponderomotive force. To demonstrate the amplification saturation in another way, Fig. 5.30 summarises the same set of data with the best energy extraction from the pump pulse as a function of the probe pulse energy and the pump pulse spectral energy density. It is calculated that energy amplification drops when $|a_0 a_1| \approx 1.2 \times 10^{-5}$.

The gain saturation seems to contradict the observation that the best energy gain is obtained with a high pump energy. This is explained from the pump pulse spectrum for this set of measurements which is slightly blue shifted, as shown in Fig. 5.31. More energy located at the higher frequency side will result in a larger probe amplification.

In Fig. 5.26, 5.27 and 5.28, the probe pulses have different chirp rates which also plays a role in the interaction process and the explanation will be attempted in the next section.

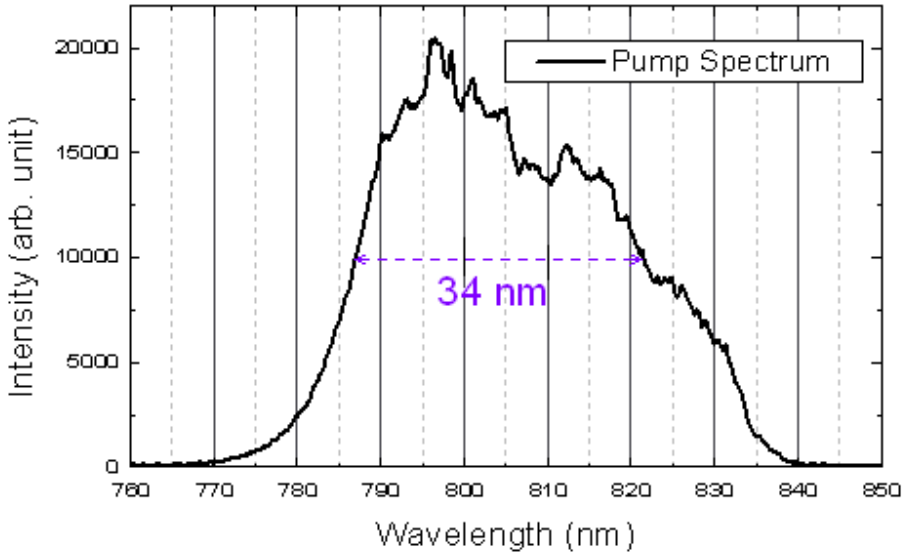

Figure 5.31: For the best energy gain measurement, the pump pulse spectrum has a slightly blue shifted profile.

5.4.3 Energy gain dependence on the chirp rate of the probe pulse

The change of probe pulse chirp rate and direction can be realised by the grating compressor, which is a part of the setup for the generation of the probe pulse (Fig. 4.3). The fully compressed probe pulses have a duration of 75 fs. The compressor has also been set to produce positively and negatively chirped probe pulses of about 105 fs and 140 fs. The on target energy for the pump and probe pulses are 340 mJ and 0.5 mJ, respectively. This experiment was performed when the filament generator is in place.

Fig. 5.32 shows the energy gain for the probe beam with different chirp rates, from which we can see that amplification is low for the shortest probe pulse and positively chirped pulses have higher gain than negatively chirped pulses. The reason for the low gain with a fully compressed probe pulse is that the probe pulse duration is shorter than the period of the electron plasma wave, which is the fundamental time-scale in plasma. For this measurements, moderate backing pressure is used corresponding to a plasma density of around 1×10^{18} cm^{-3}. Table 5.2 shows the period of the electron plasma wave for different plasma densities.

To remove the detrimental effects from the filament generator, it is then taken out

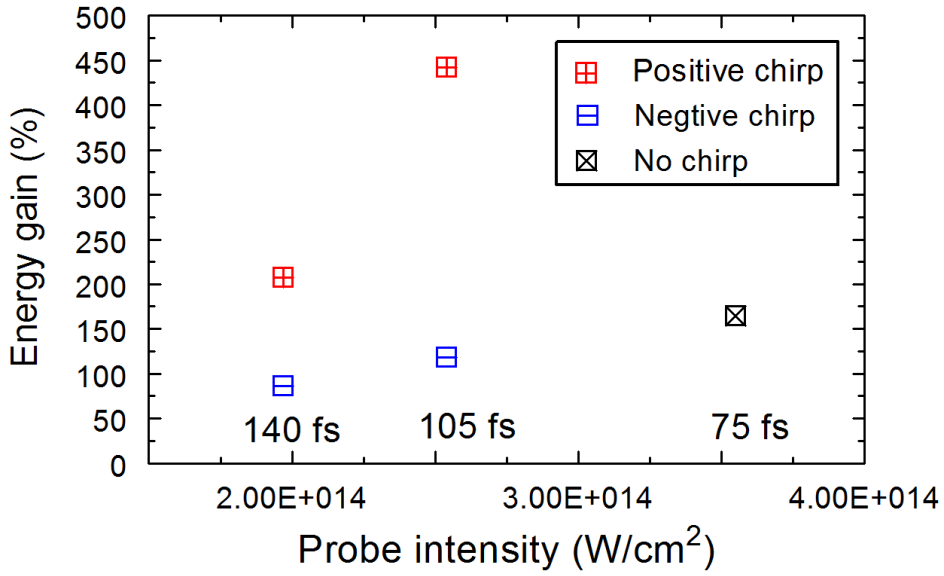

Figure 5.32: Energy amplification of fully compressed and chirped probe pulses.

Plasma density	5×10^{17} cm^{-3}	1×10^{18} cm^{-3}	2×10^{18} cm^{-3}
Period of electron plasma wave	157 fs	111 fs	78 fs

Table 5.2: Plasma density with corresponding period of electron plasma wave.

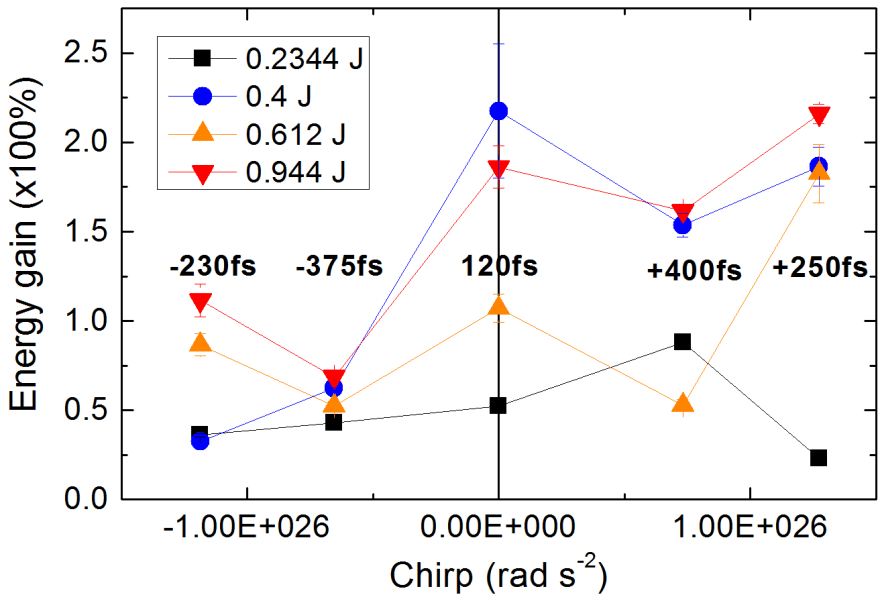

Figure 5.33: Energy gain as a function of probe chirp rate and pump energy.

from the setup and the probe spectrum is cut by the grating in the compressor. In this case, the bandwidth is narrower therefore the fully compressed pulse is about 120 fs. Changing the chirp rate of the probe pulse, the experiment is repeated with different pump energies. The pulse intensity changes with the duration but the energy of the probe is kept at 0.93 mJ. The energy gain as a function of probe chirp rate is summarised in Fig. 5.33. These measurements also show that the energy amplification is larger for positively chirped pulses than for negative ones. Moreover, since the fully compressed pulse duration is longer than the plasma period, the gain does not drop as in the previous experiment.

The mechanism that leads to a higher gain for positively chirped probe pulses is not yet fully understood. A possible explanation is presented in Section 5.6 in Dr. Farmer's thesis [111]. Simulation results show that the positive probe is preferable for amplification, same as the experimental result. However, the parameters used in the simulation are different from the experimental parameters, for example, the pump pulse is not chirped in the simulation and the intensity for both pulses are much higher than the actual laser pulses used in the experiment.

A recent published paper by Toroker [112] presents the probe pulse chirping effect on Raman amplification which may be also useful to explain this phenomenon. In the paper, they explained that it is optimal for the laser amplification with minimum probe duration at the exit of a plasma channel. When propagating in the plasma channel, the probe pulse will experience a group velocity dispersion which will result in pulse stretching. If the probe pulse has a positive chirp rate prior to it entering the plasma channel, the group velocity dispersion could be compensated for [112]. However, the plasma density need to be high enough to have a significant group velocity dispersion. Furthermore, the simulation results from 1D aPIC code using only the first order solver also shows the preference of positively chirped probe interacting with positively chirped pump. Since the first order solver does not take the plasma wave dispersion into account, it suggests that there are also other factors that affect the amplification

process for different chirp directions.

Moreover, the trapping induced plasma frequency downshift [109], as mentioned before to explain strong amplification of short wavelengths of the probe pulse, can also compensate the probe frequency increase and provide a better resonance condition for driving a plasma wave. 1D aPIC simulations are performed for probe pulses with different chirp directions and larger amplification is obtained with a positively chirped probe pulse, which is consistent with the experimental results. Comparing the electric field of plasma waves at different positions of the interaction, a larger electric field is achieved with the positively chirped probe (see Section 5.5). The importance of the trapping effect in the plasma driving process needs to be assessed in further investigations.

5.5 PIC simulation results

Numerical simulations can be used to perform virtual experiments to allow the study and visualise of complex plasma dynamics. PIC codes are a good way to simulate intense laser-plasma interactions. Taking advantage of the computational power of computers, PIC simulations trace the motion of particles in plasma to show the amplification processes and aid the analysis of the experimental results. In contrast, a three-wave field model does not describe the various kinetic effects such as particle trapping, frequency modulation and wave breaking of the plasma wave, which are all important mechanisms in our experiments, especially when the plasma wave is strongly driven.

To obtain an insight into the experimental results, 1D simulations of RBS have been performed using a reduced-PIC code known as aPIC [113], which employs envelope equations for the two laser pulses and a fully particle-like description for the plasma, similar to the reduced PIC [114], quasi-static PIC [115] and turboWAVE [116]. The transverse current is modeled as the product of plasma density envelope while the laser vector potential represents the coupling between laser and particles. Instead of

calculating the plasma density envelope using a PIC method as used by other reduced-PIC codes, the code we use applies the laser envelope to the particle current by spatially averaging over a ponderomotive bucket. This averaged PIC code is known as aPIC. Due to the averaging, the simulation time step does not resolve the laser frequency and, as a result, the simulation time is shorter than a full PIC method by a factor of ω/ω_p, where ω is the laser frequency. A moving window, which defines the simulation domain, is also implemented in the aPIC code to improve computational efficiency. Thermal spread of plasma electrons and heating from Landau damping are correctly included into this code, as they are non-collisional phenomena, however, heating from the laser pulse due to inverse Bremsstrahlung is not accounted for. The particle cell ratio is set to 50, which is sufficient to properly describe the Maxwellian distribution. Apart from a full 1D aPIC code, there is also a simplified version only using the first order solver that does not take plasma dispersion into account.

5.5.1 Simulation for the experiment with the highest gain

Simulation using the full 1D aPIC code is carried out for the experiment with the highest gain. Apart from a slightly higher energy gain, the main features are consistent with the actual experimental results. At high pump and probe pulse energies, wave breaking, bandwidth broadening, strong amplification on the high frequency side (spectral shift towards higher frequencies), as well as the small bump at low frequency side are all observed. This simulation is performed with plasma density of 1×10^{18} cm^{-3} and temperature of 50 eV, since with increasing energy, the long pump pulse can heat the plasma dramatically [117]. The a_0 for pump and probe pulses are 5.5×10^{-3} and 4.0×10^{-3}. Their wavelengths are centered at 800 nm and 816 nm with spectrum bandwidth of 32 nm and 10 nm respectively. Both laser pulses are positively chirped.

An energy gain of 25 is obtained from the 1D aPIC simulation. Fig. 5.34 shows the probe spectra before and after amplification. An obvious gain broadening is achieved indicating that not only are all the frequencies present in the laser pulse amplified, but

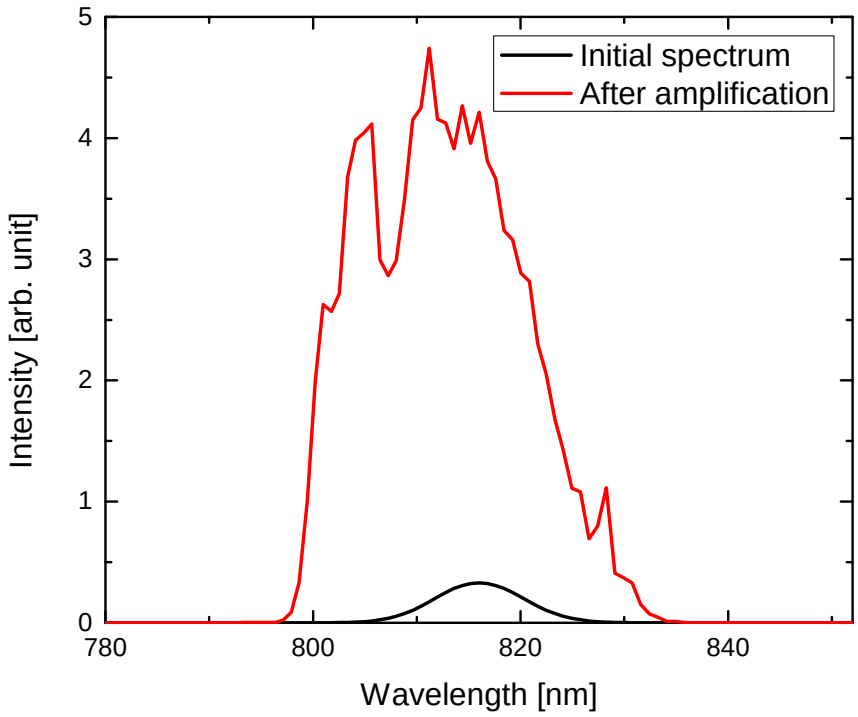

Figure 5.34: Initial and amplified probe pulse spectra of aPIC simulation for the highest gain experiment at 50 eV.

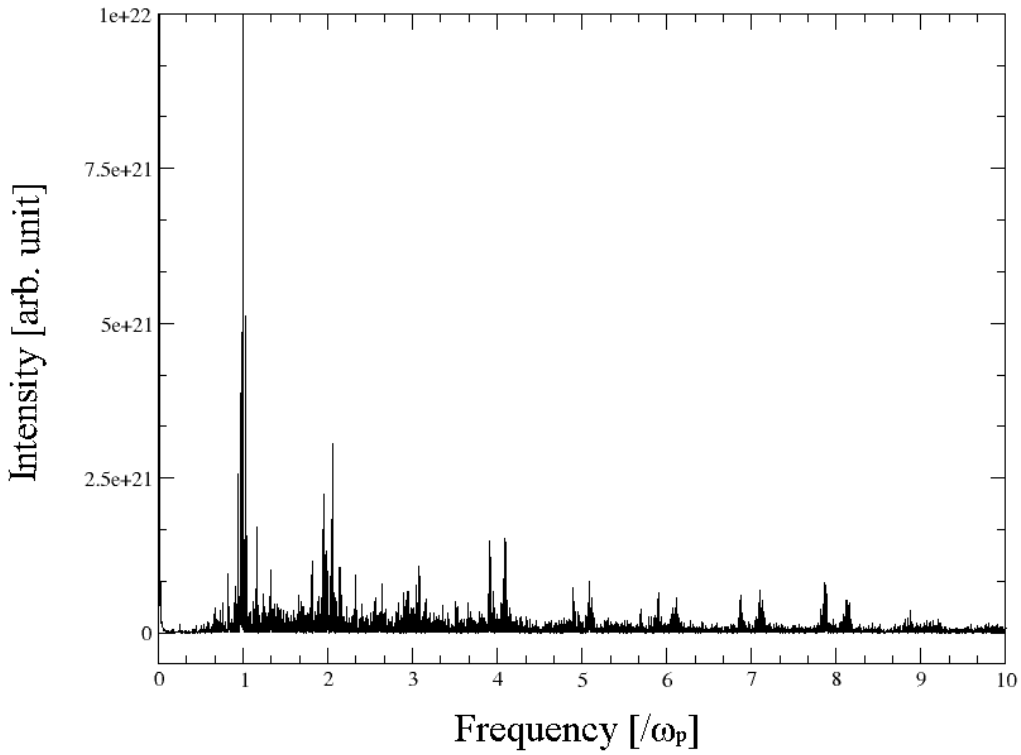

Figure 5.35: Fourier transform of the plasma wave.

new frequencies are generated. A strong amplification on the short wavelength side and a small bump on the long wavelength side can be seen on the amplified spectrum which are the features also observed in the experimental results, as shown in Fig. 5.21. Harmonic components are identified in the Fourier transform of the plasma wave, as shown in Fig. 5.35, which indicates that the plasma wave is strongly driven.

For the temporal profile, the probe pulse is first stretched due to the interaction with part of the chirped pump pulse and with further amplification of the rest frequencies it is compressed back to the initial pulse duration, as observed experimentally from the FROG measurements.

To understand the origin of these features and analyse them systematically, aPIC simulations using first order solver for the laser envelopes are performed in order to reduce the computing time. This code does not take into account dispersion, however a run including dispersion shows that for the plasma density used in this experiment it does not affect the interaction. The evolution of the spectrum and temporal profile, the

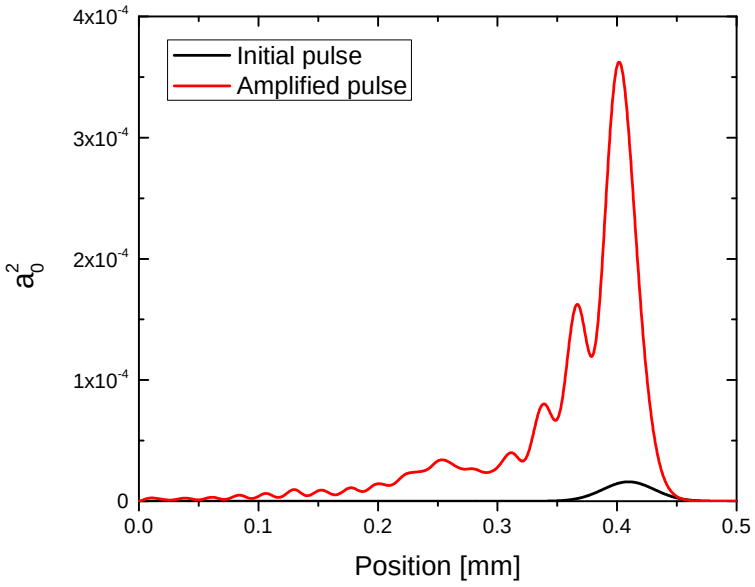

Figure 5.36: Temporal profile of initial and amplified probe pulses of aPIC simulation for the highest gain experiment at 50 eV.

electron longitudinal velocity, the electric field are all investigated and discussed in the following sections.

5.5.2 Discussion and possible explanation for the experimental observation through aPIC simulations

In the simulation, the probe pulse propagates to the right and the pump pulse to the left. The velocity of electrons propagating in the direction of the probe is set to be positive. The simulation time is T, and the physical parameters are dumped at every T/5. In the following simulations, the pump and probe are centered at 805 nm and 817 nm with spectrum bandwidth of 35 nm and 10 nm respectively. The a_0 values are 3.86×10^{-3} and 2.86×10^{-3} for the pump and probe respectively. Taking plasma heating into account, 20 eV is used as the plasma temperature, since moderate pump energy is used here.

- The spectral blue shift

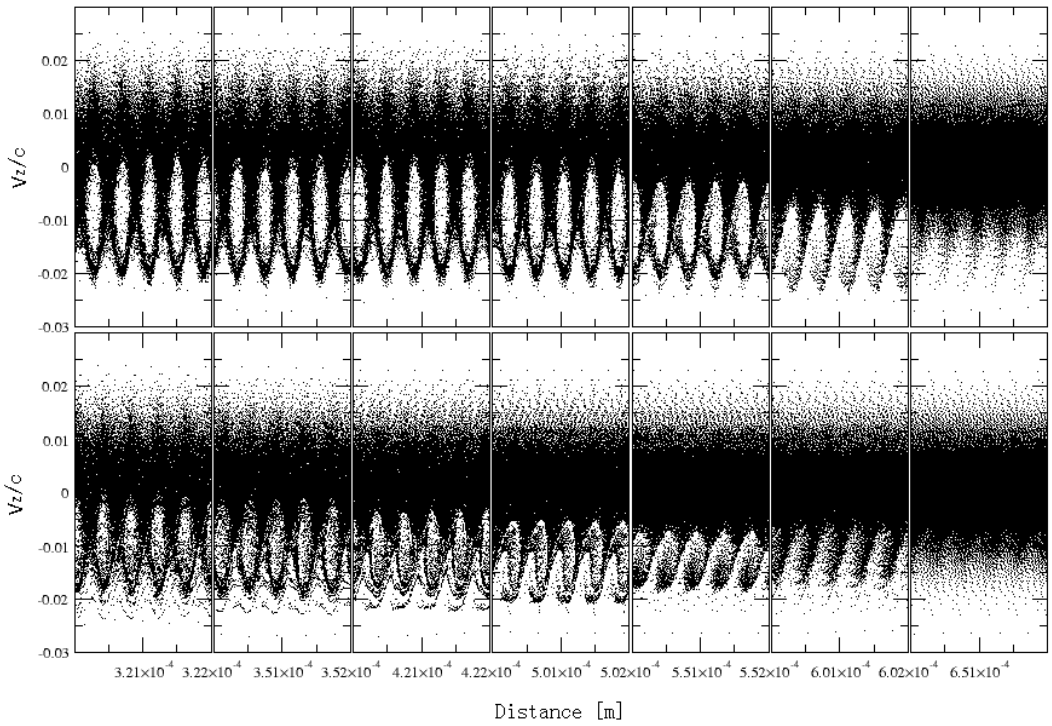

Figure 5.37: Snapshots of the electron phase space at different positions in the moving window at the early time step (T/5) at 20 eV. Top: positive chirp, bottom: negative chirp.

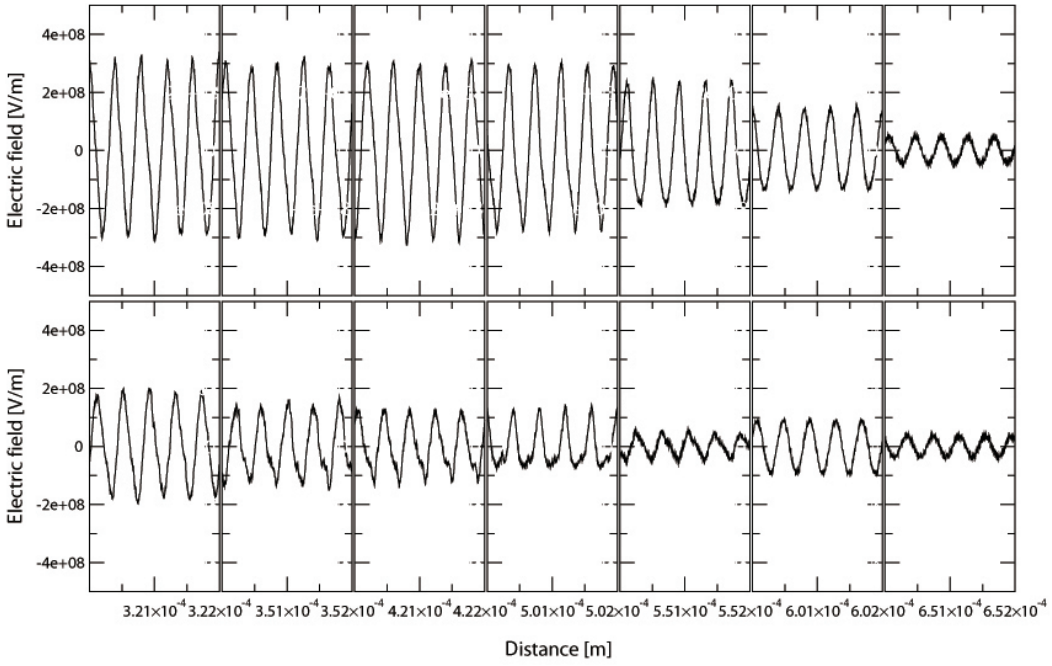

Figure 5.38: Snapshots of the electrostatic field at different positions in the moving window at the early time step (T/5) at 20 eV. Top: positive chirp, bottom: negative chirp.

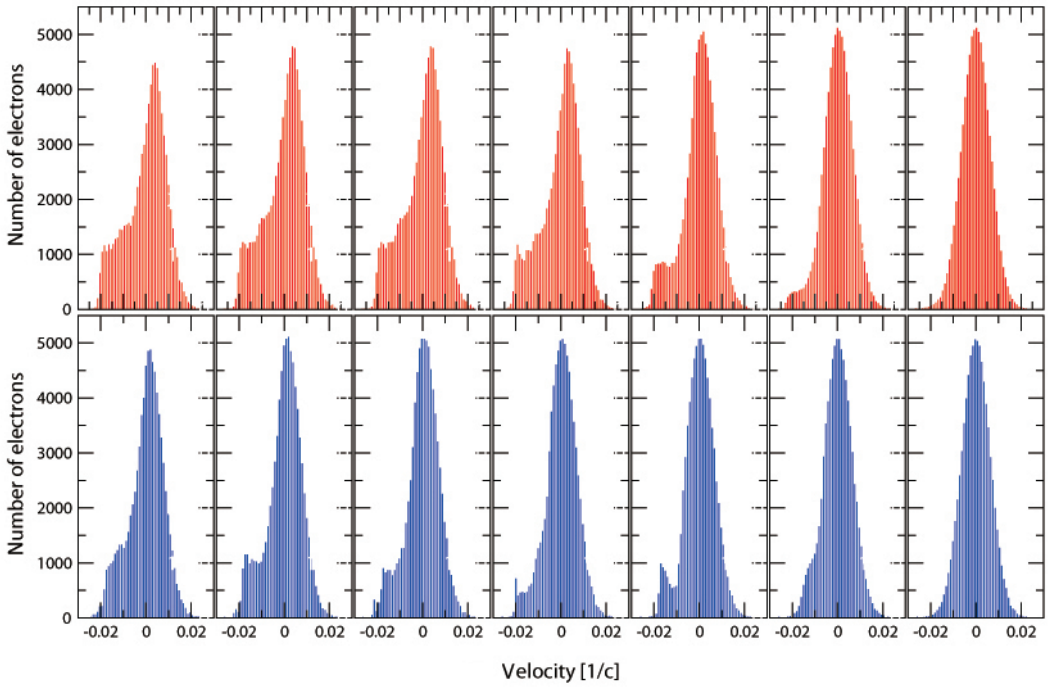

Figure 5.39: Snapshots of the electron velocity distribution at different positions in the moving window at the early time step (T/5) at 20 eV. Top: positive chirp, bottom: negative chirp.

Fig. 5.37, 5.38 and 5.39 present snapshots of electron phase spaces, electrostatic field and electron velocity distribution at different positions in the moving window at the early time step (T/5) for positively and negatively chirped probe pulse. At T/5, energy gain value is already comparable to the best gain which is achieved between 2T/5 and 3T/5.

The electron phase space in Fig. 5.37 shows the formation of the separatrixs indicating that a fraction of electrons are trapped in the beatwave buckets and undergo synchrotron oscillation. As mentioned before, the trapping induced plasma frequency downshift [109] can result as a frequency upshift for the scattered light. Fig. 5.38 illustrates that the electric fields for positive probe is larger since for the negative case the separatrixs are not as well defined with electrons falling inside the buckets. Fig. 5.39 shows the calculated electron velocity distribution. The generation of a small electron population with negative velocities corresponds to trapped electrons. If electrons oscillate in the ponderomotive bucket and do not escape, they can only acquire

a maximum velocity set by the contour of the separatrix which results as a sharp edge on the negative side and the maximum velocity is certainly defined by the height of the separatrix.

Fig. 5.40 shows the evolution of the energy gain, spectrum central frequency and bandwidth in the interaction process for positive, negative probe and positive probe with low energy pump cases. The speeds of reaching the maximum energy gain are similar for the three cases. Different with the central frequency blue shift and bandwidth change for the case of using high energy pump, the spectra obtained from a low energy pump shows little change in the central frequency and bandwidth. A slight spectral red shift could be assigned to the Bohm-Gross shift of the plasma frequency. If this is the case, temperature increase would result from Landau damping since inverse Bremsstrahlung is not included in the simulation code.

- The probe chirp direction induced energy gain difference

Simulations of the probe pulses with different chirp directions are performed and larger energy amplification is obtained for a positively chirped probe pulse, which is in agreement with the experimental results. Fig. 5.41 and 5.42 illustrate the evolution of the spectrum and temporal profile of positive and negative probe at different time steps (T/5, 2T/5 and 3T/5) at 20 eV. Maximum energy gains are 30 and 13 for positive and negative chirp respectively. The gain ratio is slightly larger than 2 which is in agreement with the experimental results. When using a negatively chirped probe, its duration increases as a result of a long-lived plasma wave, while the positive probe conserves the pulse duration. Spectral blue shift and bandwidth broadening are obtained for both cases.

For the case of both positively chirped pump and probe, the lower pump frequency interacts with the lower probe frequency first. Therefore, the front of the probe pulse has its resonant component ahead of the back of the probe, and the plasma wave is properly driven at the front first. As shown in Fig. 5.43, a larger electric field is achieved at the front of the probe. A larger electric field leads to a higher amplification,

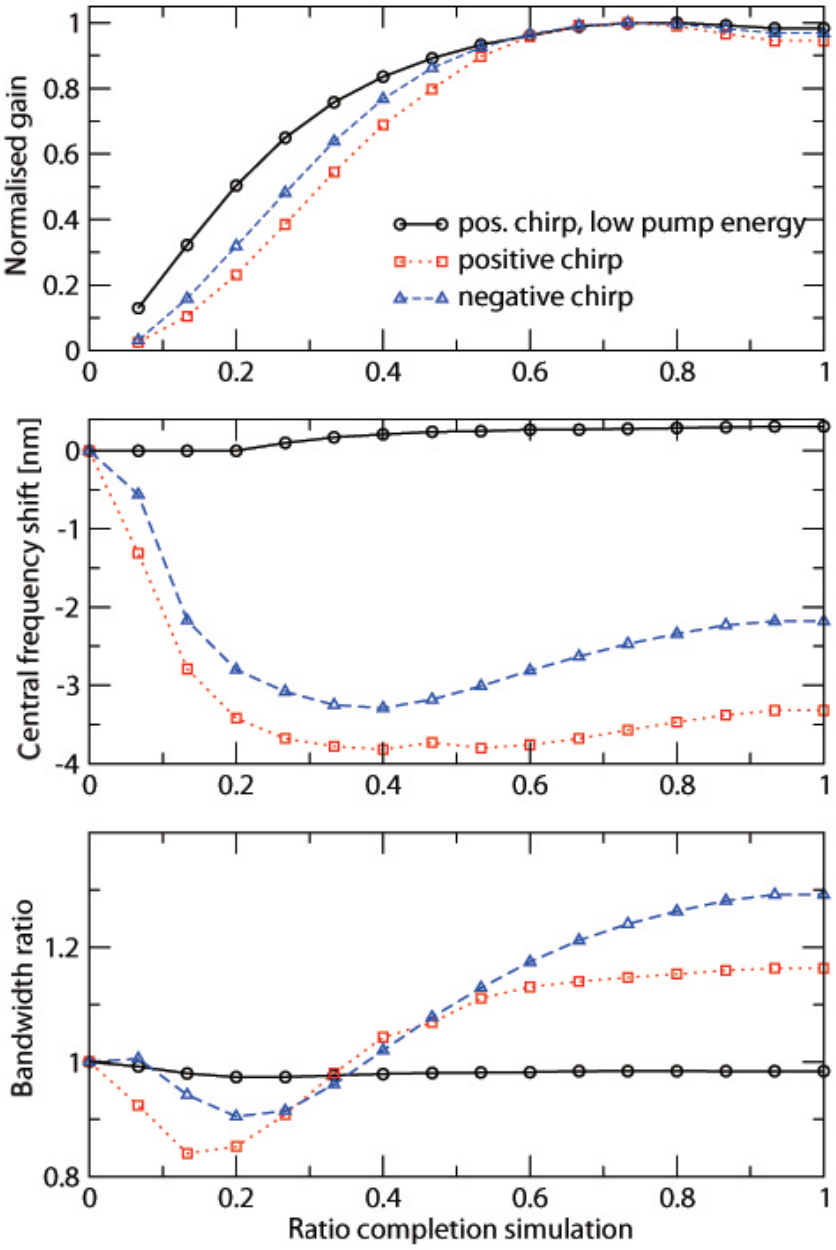

Figure 5.40: Evolution of the energy gain, spectrum central frequency and bandwidth for positive, negative chirp probe and positive probe with low energy pump.

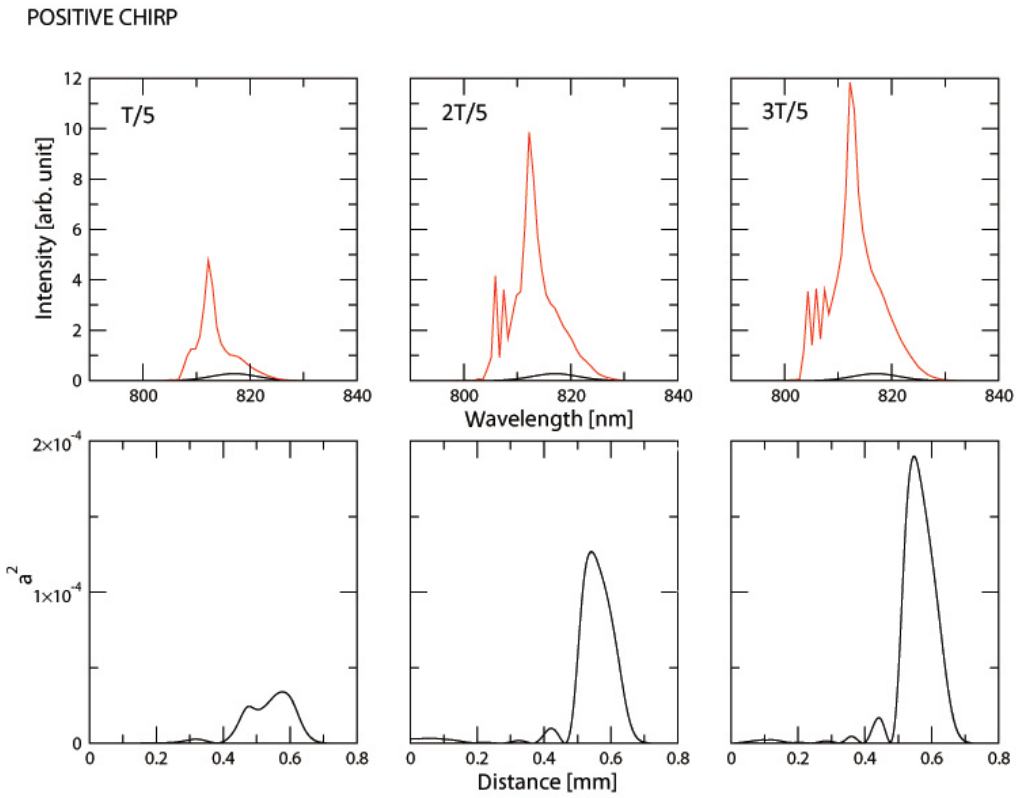

Figure 5.41: Evolution of spectrum (top) and temporal profile (bottom) of a positively chirped probe laser pulse at time step of T/5, 2T/5 and 3T/5, at 20 eV

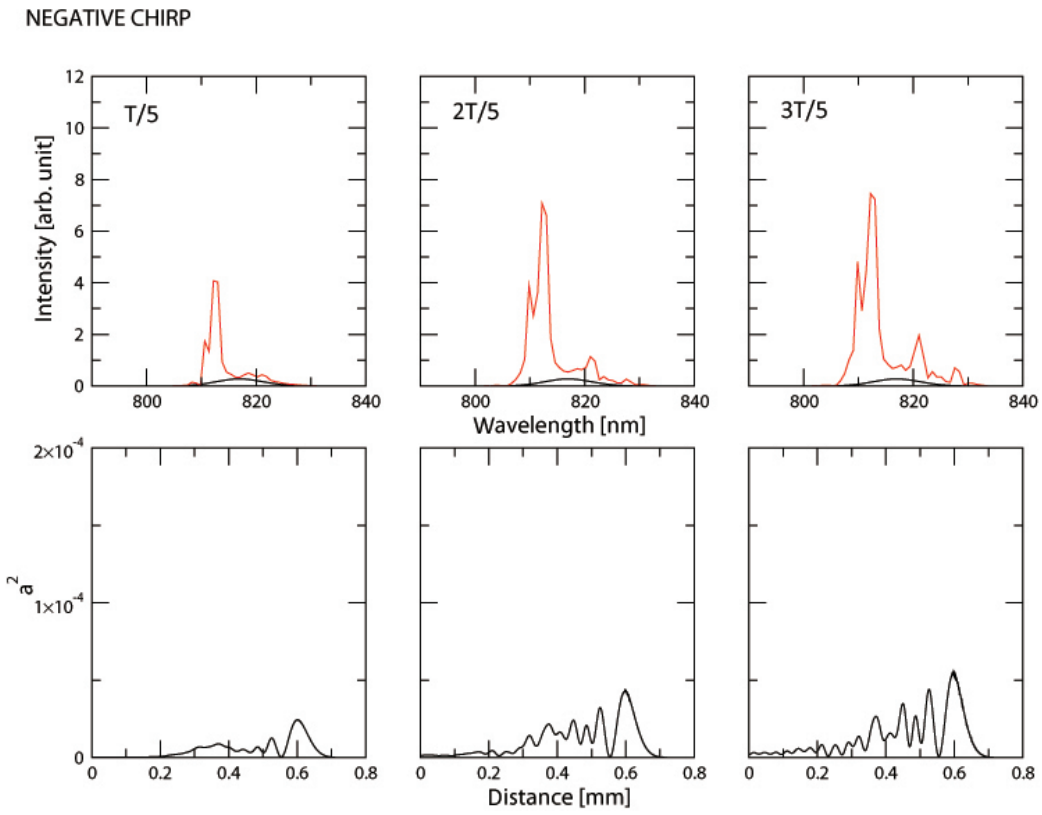

Figure 5.42: Evolution of spectrum (top) and temporal profile (bottom) of a negatively chirped probe laser pulse at time step of T/5, 2T/5 and 3T/5, at 20 eV

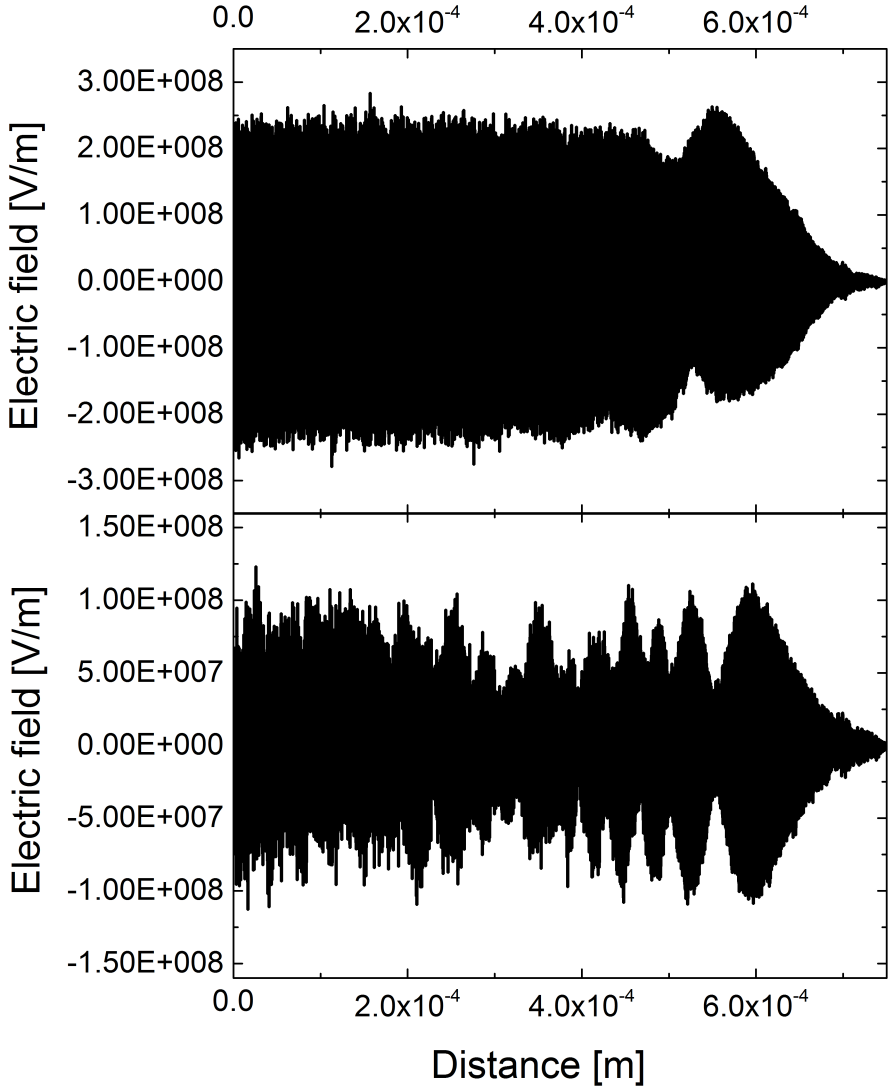

Figure 5.43: Electrostatic field of the positive chirp case (top) and the negative chirp case (bottom) at time step of 2T/5, at 20 eV

as shown in the temporal profile in Fig. 5.41. A well amplified front of the probe pulse drives a stronger plasma wave and gets better amplified, which results in a positive feedback.

On the other hand, in the case of a negative probe, the back of the pulse is amplified first, since it meets its resonant component in the pump before the front, as shown in Fig. 5.42. Moreover, being non resonant, the front of the probe drives the plasma slightly away from plasma frequency. Therefore, the electrostatic field for the negative case is smaller since the plasma is modified by the non-resonant driving force at the front, as illustrated in Fig. 5.43. Moreover, looking at the last snapshot, a low amplitude plasma wave is still present over the full length of the simulation window. This can explain the increased duration of the probe, as the pump may still scatter of the wave. The pulse duration increase is not observed in the experiment, which could result from the fact that the diagnostic (FROG) only has a temporal window of 1 ps and therefore we could only be measuring the front spike, or since the energy gain is much lower, such a plasma wave might be less or not excited at the back of the main pulse in reality.

To conclude, a simulation with parameters of the experiment achieving the highest energy gain has been performed. A similar result with spectral broadening and preserved temporal profile are obtained. Studying the electron velocity and electric field in phase space and comparing these with using a different probe amplitude, the transition regime between the Raman and Compton scattering is explored. We show that it is possible to transfer to the Compton regime through Raman amplification. It is also confirmed that in spite of the criterion for reaching the Compton regime is not satisfied at the end, as the case of this experiment, some electrons are trapped by the ponderomotive potential and their dynamics are governed by the ponderomotive force, while the rest are controlled by the plasma wave. However, it has to be pointed out that since the beatwave frequency and the plasma wave frequency are very similar in this experiment, it is hard to distinguish the electron trapping by the ponderomotive force

of the beatwave and the electrostatic force of the plasma wave.

Possible explanations are given for the features observed in the experiment, including the bandwidth broadening, the spectral blue shift, the frequency components appeared around $2\omega_p$. Moreover, a rough analysis of amplification of probe pulse with different chirp directions is performed. It is confirmed that a higher energy gain can be obtained when interact a positively chirped pump pulse with a positively chirped probe pulse. More work can be done to investigate the amplification saturation with increasing pump or probe energy. For the aPIC code, it can be further developed to run in 2D and the plasma heating due to the pump pulse can be added since the inverse bremsstrahlung heating can also build up a thermal chirp of plasma frequency over time by the Bohm-Gross shift.

Chapter 6

Summary and outlook

6.1 Summary

This thesis reports on experiments aimed towards the development of a new generation of laser amplifiers able to reach higher intensities than current CPA laser systems. The main novelty of this work is utilising a long gas-filled capillary waveguide to generate plasma with relatively low density to set a lower threshold for entering the nonlinear regime. Typical parameters of the plasma channel used in previous published work are few mm plasma with density on the order of 1×10^{19} cm^{-3} which is one order of magnitude higher than this experiment.

As discussed in Chapter 1, Raman scattering can transfer energy from the high frequency components to the low frequency components of two counter-propagating laser pulses in plasma which is a medium capable of withstanding extremely high intensities. The theoretical background is discussed in Chapter 2 and 3, while the experimental details and the results are presented in Chapter 4 and 5, respectively.

The test of the gas-filled capillary discharge waveguide with the transmission efficiency of up to 80% is presented in Chapter 5. Then, a two-stage experiment carried out by colliding a short probe pulse and a long pump pulses in a 4 cm capillary with preformed plasma of density around 1×10^{18} cm^{-3} is presented. A low pump energy

is used in the first stage of the experiment, which is focused on the verification of basic aspects of chirped pulse Raman amplification in the linear regime. The pump pulse centred at 805 nm with 35 nm bandwidth is 250 ps long with an on target energy of up to 445 mJ, while the frequency filtered probe pulse is centred around 818 nm with bandwidth of 13 nm and is compressed to 78 fs with energy of 1.3 mJ. Changing the relative timing between the two pulses, the probe pulse energy gain firstly increases up to 240% and then decreases with the central frequency shifting from high to low frequencies. This is due to the probe pulse first only interacting with the high frequency components at the back of the pump, and then the whole pump pulse, at last only interacting with the low frequency components at the front. FROG measurements show that the probe duration initially increases to about 90 fs and then decreases to about 65 fs, with a corresponding narrowing and broadening of the bandwidth respectively. This asymmetry is due to the filtered probe frequency not being properly downshifted by the plasma frequency (i.e. although the central frequencies of the pump and the probe pulse are separated by ω_p, the probe pulse is just the lower frequency components of the pump pulse. Therefore, only part of the pump pulse energy is effective for Raman amplification). The filament generation, as described in Section 4.2.1, is then employed to downshift the probe pulse frequency by self-phase modulation. The energy gain presents exponential growth with the pump energy and it increases with backing pressure. Despite the better frequency matching, no gain improvement is observed because filament generation is very sensitive to alignment and causes a degradation of the probe beam quality. Therefore, in the second stage, the beam frequency is adjusted by tunning the compressor.

The second stage of this experiment employs higher pump energies, up to 840 mJ. Raman amplification is expected to start in the linear regime and, as the amplified probe intensity grows, to evolve into the nonlinear regime where the density perturbation frequency is not restricted to the plasma frequency. The highest energy gain of 650% is achieved with the pump and probe on target energy of 825 mJ and 0.9 mJ, respectively.

The efficiency of energy transfer from the pump pulse to the probe is 1.4% (only the energy of the pump that actually interact with the probe is used). The highest energy transfer efficiency is 5% in this experiment. When using high pump and probe energies, in addition to the large energy amplification, the spectral gain shows several features not seen in the linear regime. First of all, spectral bandwidth broadening on both sides is observed. This feature indicates that the scattering medium is no longer only oscillating at the plasma frequency. The driving force for this nonresonant oscillation could be the ponderomotive force of the beatwave of the pump and probe pulses. The broadening happens mainly on the blue side because the trapping of electrons in the ponderomotive bucket or the plasma wave observed from aPIC simulation reduces the plasma frequency due to the decreasing of the number of electrons oscillating at the plasma frequency. Another special feature is a small bump observed in the amplified probe spectrum at a frequency which is downshifted by twice the plasma frequency from the pump pulse central frequency. This bump can contain up to 10% of the pulse energy. The origin of this feature could be the backscattering of the pump from the second harmonic of the plasma wave or the secondary scattering of the pump.

These features suggest that the dynamic of electrons with smaller momentum are trapped by the ponderomotive force while other electrons are dominated by the resonant plasma oscillation. Therefore, a transition regime between the linear and the Compton regime could be reached. Simulations in Ref. [87] show that the linear response will still exist even when the criteria for entering the Compton regime is reached, thus this transition stage will hold until the l.h.s. of Eq. 3.26 is much greater then the square of the plasma frequency, indicating the criteria is not strict. Moreover, saturations of the probe pulse energy and intensity gain are observed as a result of either increasing the pump or the probe pulse amplitude, as shown in Fig. 5.26, 5.27, 5.29 and 5.30. It is also demonstrated that a positively chirped probe pulse is better amplified by the positively chirped pump pulse than a probe pulse with negative chirp, as shown in Fig. 5.32 and 5.33.

A reduced PIC code is used to simulate the experiment. The preliminary simulation results are in agreement with the experimental results. Using the experimental parameters, the study shows that although at the end of the interaction, ω_b is still smaller than ω_p, some electrons with small velocity are trapped indicating that this experiment reaches the nonlinear regime of the Raman amplification. Moreover, the physics behind the special features observed from experimental results are investigated, including the spectral blue shift and the probe chirp direction induced energy gain difference.

6.2 Future studies and outlook

For the ultimate objective of developing the next generation of laser amplifier, there is still a long way to go in both theory and experiments. The experimental results and PIC simulations presented here suggest that the gain and stability of the Raman amplifier can be improved by modifying the experimental setup.

First of all, in order to further probe the Compton regime, the pump pulse intensity needs to be increased to strengthen the ponderomotive force. This can be realised by employing a shorter pump pulse. It has been planned to add a compressor for the pump pulse. For a 10 ps pump duration, including the loss of the compressor into account, the on target pump pulse intensity will be raised to 5×10^{14} Wcm^{-2}, which is identified by simulations as having the best amplification. A 10 ps duration implies a 1.5 mm interaction length, which can be realised in a gas jet with no need of a plasma waveguide. For the aim of studying the Compton regime, a relatively low plasma density is required. Due to the shorter pump pulse, the capillary length can be reduced to a few millimetres, but in this case it would be difficult to form a uniform longitudinal plasma density profile. Besides, for a diameter of 300 μm, the scalloping period is 40 mm and it would be advantageous to use a capillary with length equals to one or half of the scalloping period, since the output beam size would always be the same as the input, no matter whether the input spot matches the capillary

diameter or not. Additionally, if the plasma channel is longer than the interaction length, the requirement for the alignment accuracy can be reduced. Given the above considerations, a 2 cm capillary would be preferable. A 2 mm gas jet is an alternative choice, since it is relatively easy to obtain a flat density profile. Because of the higher laser intensity, further experimental studies have been started to test the compression and guiding of the shorter pump pulse.

The power supply used to generate the plasma discharge can also be improved. It is planned to replace the toroidal magnetic transformer-based pulser with a newly designed solid-state pulser developed at Strathclyde, which can provide a current pulse with much steeper rising edge, and therefore, a 8 times reduction of the pulse jitter [101]. Stable plasma formation is crucial for Raman amplification due to the need for consistent and reproducible synchronisation with the laser system. Moreover, the old pulser cannot break down the gas at high backing pressures, however, it may not be a problem with a shorter plasma channel, it will be certainly easier to use the new pulser to strike through a denser gas and produce plasma with density around 3×10^{18} cm^{-3} to 5×10^{18} cm^{-3}, as required for high gain amplification for 800 nm laser pulses which is indicated by theory predictions.

It would also be worthwhile considering the use of a separate laser system for the probe pulse generation. There are two advantages: the two beams can be controlled independently with no mutual influence; more importantly, removing the frequency shift part can reduce the difficulty of performing this experiment and can improve the probe pulse quality. The two lasers will have to be synchronised with the order of 100 fs. Using the same oscillator would ensure the synchronism of around 1 to 10 fs.

In addition to these experimental improvements, theoretical considerations should also be addressed. For example, can the pure Compton regime be accessed through a smooth transition or is there a barrier to surpass? Additionally, when using a much more intense pump pulse, the plasma thermal wavebreaking will be a limiting factor for Raman amplification. And how will the thermal effects affect the Compton regime? To

answer these questions, PIC simulations are essential to accurately model the complex plasma dynamics.

Finally, lets discuss the general prospects of this project. Since we already have a high energy pulse, it may seem natural to just compress it rather than use it to pump another short pulse. The ultimate goal of this project is however to make use of a plasma with a smooth density gradient and a monochromatic high energy pump pulse to amplify an ultra-short probe pulse, since monochromatic high energy lasers are easily available. To achieve this objective, the development of tapered capillary is concurrently performed with the study of the amplification mechanism [108]. Another concern is the efficiency of the amplification process. Although theoretically, the energy transfer efficiency can be 100%, experimentally it is never beyond a few percent. Several articles [110, 118] have endeavoured to identify experimental parameters for favourable amplification through PIC simulations. Ongoing efforts should be made to follow the guidelines provided by simulations to experimentally validate the right parameters to achieve higher energy transfer efficiency. Since reaching the relativistic intensities may stop the amplification and destroy the laser pulse in a plasma, the idea is to use a plasma channel with larger cross-section to amplify laser pulses with a larger spot size to prevent relativistic effects. After amplification the pulse would be focussed to increase its intensity.

To conclude, the plasma based laser amplifier is a promising concept supported with solid theory and lots of novel ideas. During the last few decades, considerable work has been devoted to this scheme, however there are more questions remaining unknown and awaiting to be answered. Therefore, persistent effort is required towards the goal of developing the next generation of laser amplifier.

Bibliography

[1] A. Einstein. Zur Quantentheorie der Strahlung. *Physikalische Zeitschrift*, 18:121–128, 1917.

[2] R. Ladenburg. Research on the anomalous dispersion of gases. *Z. Phys.*, 48:15–25, 1928.

[3] T. H. Maiman. Stimulated optical radiation in ruby. *Nature*, 187(4736):493–494, August 1960.

[4] F. J. McClung and R. W. Hellwarth. Giant optical pulsations from ruby. *Journal of Applied Physics*, 33:828–829, March 1962.

[5] L. E. Hargrove, R. L. Fork, and M. A. Pollack. Locking of He-Ne laser modes induced by synchronous intracavity modulation. *Applied Physics Letters*, 5:4–5, July 1964.

[6] M. Didomenico, Jr. Small-signal analysis of internal (coupling-type) modulation of lasers. *Journal of Applied Physics*, 35:2870–2876, Nov 1964.

[7] D. E. Spence, P. N. Kean, and W. Sibbett. 60-fsec pulse generation from a self-mode-locked Ti:sapphire laser. *Optics Letters*, 16, Jan 1991.

[8] D. Strickland and G. Mourou. Compression of amplified chirped optical pulses. *Optics Communications*, 55:447–449, October 1985.

[9] D. A. Jaroszynski, B. Ersfeld, G. Giraud, S. Jamison, D. R. Jones, R. C. Issac, B. M. W. McNeil, A. D. R. Phelps, G. R. M. Robb, H. Sandison, G. Vieux,

S. M. Wiggins, and K. Wynne. The Strathclyde terahertz to optical pulse source (TOPS). *Nuclear Instruments and Methods in Physics Research A*, 445:317–319, May 2000.

[10] T. Tajima and J. M. Dawson. Laser electron accelerator. *Phys. Rev. Lett.*, 43:267–270, Jul 1979.

[11] J. J. Macklin, J. D. Kmetec, and C. L. Gordon. High-order harmonic generation using intense femtosecond pulses. *Phys. Rev. Lett.*, 70(6):766–769, Feb 1993.

[12] D. C. Eder, P. Amendt, and S. C. Wilks. Optical-field-ionized plasma x-ray lasers. *Phys. Rev. A*, 45(9):6761–6772, May 1992.

[13] C. Fattinger and D. Grischkowsky. Terahertz beams. *Applied Physics Letters*, 54:490–492, Feb 1989.

[14] J. van Tilborg, C. B. Schroeder, C. V. Filip, Cs. Tóth, C. G. R. Geddes, G. Fubiani, R. Huber, R. A. Kaindl, E. Esarey, and W. P. Leemans. Temporal characterization of femtosecond laser-plasma-accelerated electron bunches using terahertz radiation. *Phys. Rev. Lett.*, 96:014801, Jan.

[15] M. Tabak, J. Hammer, M. E. Glinsky, W. L. Kruer, S. C. Wilks, J. Woodworth, E. M. Campbell, M. D. Perry, and R. J. Mason. Ignition and high gain with ultrapowerful lasers. *Physics of Plasmas*, 1:1626–1634, 1994.

[16] G. Shvets, N. J. Fisch, A. Pukhov, and J. Meyer-ter-Vehn. Superradiant amplification of an ultra-short laser pulse in a plasma by a counter-propagating pump. *Phys. Rev. Lett.*, 81:4879, 1998.

[17] M. Maier, W. Kaiser, and J. A. Giordmaine. Intense light bursts in the stimulated Raman effect. *Phys. Rev. Lett.*, 17(26):1275–1277, Dec 1966.

[18] W. H. Culver, J. T. A. Vanderslice, and V. W. T. Townsend. Controlled generation of intense light pulses in reverse-pumped Raman lasers. *Applied Physics Letters*, 12(5):189 –190, March 1968.

[19] R. W. Minck, E. E. Hagenlocker, and W. G. Rado. Simultaneous occurrence of and competition between stimulated optical-scattering processes in gases. *Journal of Applied Physics*, 38:2254–2260, April 1967.

[20] R. V. Johnson and J. H. Marburger. Relaxation oscillations in stimulated Raman and Brillouin scattering. *Phys. Rev. A*, 4(3):1175–1182, Sep 1971.

[21] G. I. Kachen and W. H. Lowdermilk. Relaxation oscillations in stimulated Raman scattering. *Phys. Rev. A*, 16(4):1657–1664, Oct 1977.

[22] A. Glass. 7.4–Design considerations for Raman lasers. *Quantum Electronics, IEEE Journal of*, 3(11):516 – 520, November 1967.

[23] G. I. Kachen, Jr. *Spatial and temporal characteristics of collimated and focused traveling wave Raman amplifiers.* PhD thesis, UNIVERSITY OF CALIFORNIA, DAVIS., 1975.

[24] R.D. Milroy, C.E. Capjack, and C.R. James. Plasma laser pulse amplifier using induced Raman or Brillouin processes. *Physics of Fluids*, 22:1922–1931, October 1979.

[25] D. W. Forslund, J. M. Kindel, and E. L. Lindman. Theory of stimulated scattering processes in laser-irradiated plasmas. *Physics of Fluids*, 18, Aug 1975.

[26] W. L. Kruer. *The Physics of Laser Plasma Interactions*. Addison-Wesley, 1988.

[27] G. Shvets, J. S. Wurtele, and B. A. Shadwick. Analysis and simulation of Raman backscatter in underdense plasmas. *Phys. Plasmas*, 4:1872, April 1997.

[28] C. Rousseaux, G. Malka, J. L. Miquel, F. Amiranoff, S. D. Baton, and Ph. Mounaix. Experimental validation of the linear theory of stimulated Raman

scattering driven by a 500-fs laser pulse in a preformed underdense plasma. *Phys. Rev. Lett.*, 74(23):4655–4658, Jun 1995.

[29] V. Malka, E. De Wispelaere, J. R. Marques, R. Bonadio, F. Amiranoff, F. Blasco, C. Stenz, Ph. Mounaix, G. Grillon, and E. Nibbering. Stimulated Raman backscattering instability in short pulse laser interaction with helium gas. *Physics of Plasmas*, 3(5):1682–1688, May 1996.

[30] V. M. Malkin, G. Shvets, and N. J. Fisch. Fast compression of laser beams to highly overcritical powers. *Phys. Rev. Lett.*, 82(22):4448 – 4451, 1999.

[31] B. Ersfeld and D. A. Jaroszynski. Superradiant linear Raman amplification in plasma using a chirped pump pulse. *Phys. Rev. Lett.*, 95:165002, 2005.

[32] Y. Ping, I. Geltner, A. Morozov, N. J. Fisch, and S. Suckewer. Raman amplification of ultrashort laser pulses in microcapillary plasmas. *Phys. Rev. E*, 66(4):046401–+, October 2002.

[33] A. A. Balakin, D. V. Kartashov, A. M. Kiselev, S. A. Skobelev, A. N. Stepanov, and G. M. Fraiman. Laser pulse amplification upon Raman backscattering in plasma produced in dielectric capillaries. *Soviet Journal of Experimental and Theoretical Physics Letters*, 80:12–16, July 2004.

[34] Y. Ping, W. Cheng, and S. Suckewer. Amplification of ultrashort laser pulses by a resonant Raman scheme in a gas-jet plasma. *Phys. Rev.Lett.*, 92(17), 2004.

[35] M. Dreher, E. Takahashi, J. Meyer-ter-Vehn, and K.-J. Witte. Observation of superradiant amplification of ultrashort laser pulses in a plasma. *Phys. Rev. Lett.*, 93(9):095001, Aug 2004.

[36] J. Ren, W. Cheng, S. Li, and S. Suckewer. A new method for generating ultraintense and ultrashort laser pulses. *Nature Physics*, 3:732–736, October 2007.

[37] G. Vieux, A. Lyachev, X. Yang, B. Ersfeld, J. P. Farmer, E. Brunetti, R. C. Issac, G. Raj, G. H. Welsh, S. M. Wiggins, and D. A. Jaroszynski. Chirped pulse Raman amplification in plasma. *New Journal of physics*, 13(6):063042, Jun 2011.

[38] J. A. Bittencourt. *Fundamentals of Plasma Physics*. Pergamon Press, 1986.

[39] L.V. Keldysh. Ionizations in the field of a strong electromagnetic wave. *Soviet Physics JETP*, 20:1307–1314, 1965.

[40] M. Protopapas, C. H. Keitel, and P. L. Knight. Atomic physics with super-high intensity lasers. *Reports on Progress in Physics*, 60:389–486, Apr 1997.

[41] R.J. Goldston and P.H. Rutherford. *Introduction to plasma physics*. Institute of Physics Publishing, 1995.

[42] F. F. Chen. *Introduction to plasma physics and controlled fusion*, volume 2nd edition. Plenum Press, New York, 1984.

[43] D. Bohm and E. P. Gross. Theory of plasma oscillations origin of medium-like behavior. *Phys. Rev.*, 75:1851, 1949.

[44] R. L. Berger, D. S. Clark, A. A. Solodov, E. J. Valeo, and N. J. Fisch. Inverse bremsstrahlung stabilization of noise in the generation of ultrashort intense pulses by backward raman amplification. *Physics of Plasmas*, 11:1931–1937, 2004.

[45] L Landau. On the thermodynamics of photoluminescence. *J. Phys.(Moscow)*, pages 503–506, 1946.

[46] John Dawson. On landau damping. *Physics of Fluids (1958-1988)*, 4(7):869–874, 2004.

[47] EAJ Marcatili and RA Schmeltzer. Hollow metallic and dielectric waveguides for long distance optical transmission and lasers. *Bell System Technical Journal*, 43(4):1783–1809, 1964.

[48] F. Dorchies, J. R. Marquès, B. Cros, G. Matthieussent, C. Courtois, T. Vélikoroussov, P. Audebert, J. P. Geindre, S. Rebibo, G. Hamoniaux, and F. Amiranoff. Monomode guiding of $10^{16} W/\mathrm{cm}^2$ laser pulses over 100 rayleigh lengths in hollow capillary dielectric tubes. *Phys. Rev. Lett.*, 82, Jun 1999.

[49] P. Sprangle, E. Esarey, J. Krall, and G. Joyce. Propagation and guiding of intense laser pulses in plasmas. *Physical Review Letters*, 69:2200–2203, Oct 1992.

[50] E. Esarey, P. Sprangle, J. Krall, and A. Ting. Self-focusing and guiding of short laser pulses in ionizing gases and plasmas. *IEEE Journal of Quantum Electronics*, 33:1879–1914, 1997.

[51] P. Monot, T. Auguste, P. Gibbon, F. Jakober, G. Mainfray, A. Dulieu, M. Louis-Jacquet, G. Malka, and J. L. Miquel. Experimental demonstration of relativistic self-channeling of a multiterawatt laser pulse in an underdense plasma. *Physical Review Letters*, 74:2953–2956, Apr 1995.

[52] K. Krushelnick, A. Ting, C. I. Moore, H. R. Burris, E. Esarey, P. Sprangle, and M. Baine. Plasma channel formation and guiding during high intensity short pulse laser plasma experiments. *Physical Review Letters*, 78:4047–4050, May 1997.

[53] P. Sprangle, E. Esarey, and A. Ting. Nonlinear theory of intense laser-plasma interactions. *Physical Review Letters*, 64:2011–2014, Apr 1990.

[54] J. Faure, V. Malka, J.-R. Marquès, P.-G. David, F. Amiranoff, K. Ta Phuoc, and A. Rousse. Effects of pulse duration on self-focusing of ultra-short lasers in underdense plasmas. *Physics of Plasmas*, 9:756–759, March 2002.

[55] G.-Z. Sun, E. Ott, Y. C. Lee, and P. Guzdar. Self-focusing of short intense pulses in plasmas. *Physics of Fluids*, 30:526–532, Feb 1987.

[56] D. C. Barnes, T. Kurki-Suonio, and T. Tajima. Laser self-trapping for the plasma fiber accelerator. *IEEE Transactions on Plasma Science*, 15:154–160, Apr 1987.

[57] A. Zigler, Y. Ehrlich, C. Cohen, J. Krall, and P. Sprangle. Optical guiding of high-intensity laser pulses in a long plasma channel formed by a slow capillary discharge. *Journal of the Optical Society of America B Optical Physics*, 13:68–71, January 1996.

[58] Y. Ehrlich, C. Cohen, A. Zigler, J. Krall, P. Sprangle, and E. Esarey. Guiding of high intensity laser pulses in straight and curved plasma channel experiments. *Physical Review Letters*, 77:4186–4189, Nov 1996.

[59] D. Kaganovich, A. Ting, C. I. Moore, A. Zigler, H. R. Burris, Y. Ehrlich, R. Hubbard, and P. Sprangle. High efficiency guiding of terawatt subpicosecond laser pulses in a capillary discharge plasma channel. *Physical Review E*, 59:4769, May 1999.

[60] D. J. Spence, A. Butler, and S. M. Hooker. First demonstration of guiding of high-intensity laser pulses in a hydrogen-filled capillary discharge waveguide. *Central Laser Facility Annual Report 2000/2001*, 2000.

[61] Y. R. Shen. *Principles Of Nonlinear Optics*. 2003.

[62] J. H. Milonni, P. W . Eberly. *Lasers*. New York: Wiley, 1988.

[63] P. Monot, T. Auguste, L. A. Lompré, G. Mainfray, and C. Manus. Focusing limits of a terawatt laser in an underdense plasma. *Journal of the Optical Society of America B Optical Physics*, 9:1579–1584, Sep 1992.

[64] A. Braun, G. Korn, X. Liu, D. Du, J. Squier, and G. Mourou. Self-channeling of high-peak-power femtosecond laser pulses in air. *Optics Letters*, 20:73–75, January 1995.

[65] P. B. Corkum, Claude Rolland, and T. Srinivasan-Rao. Supercontinuum generation in gases. *Phys. Rev. Lett.*, 57(18):2268–2271, Nov 1986.

[66] A. Couairon, J. Biegert, C. P. Hauri, W. Kornelis, F. W. Helbing, U. Keller, and A. Mysyrowicz. Self-compression of ultra-short laser pulses down to one optical cycle by filamentation. *Journal of Modern Optics*, 53:75–85, January 2006.

[67] J. Kasparian, R. Sauerbrey, and S. L. Chin. The critical laser intensity of self-guided light filaments in air. *Applied Physics B: Lasers and Optics*, 71:877–879, 2000.

[68] S. Tzortzakis, G. Méchain, G. Patalano, Y.-B. André, B. Prade, M. Franco, A. Mysyrowicz, J.-M. Munier, M. Gheudin, G. Beaudin, and P. Encrenaz. Coherent subterahertz radiation from femtosecond infrared filaments in air. *Opt. Lett.*, 27(21):1944–1946, Nov 2002.

[69] N. Aközbek, A. Iwasaki, A. Becker, M. Scalora, S. L. Chin, and C. M. Bowden. Third-harmonic generation and self-channeling in air using high-power femtosecond laser pulses. *Phys. Rev. Lett.*, 89(14):143901, Sep 2002.

[70] D. S. Montgomery, R. J. Focia, H. A. Rose, D. A. Russell, J. A. Cobble, J. C. Fernández, and R. P. Johnson. Observation of stimulated electron-acoustic-wave scattering. *Physical Review Letters*, 87(15):155001, Oct 2001.

[71] Chandrasekhara Venkata Raman. A new radiation. *Indian Journal of physics*, 2:387–398, 1928.

[72] C. S. Liu, M. N. Rosenbluth, and R. B. White. Raman and Brillouin scattering of electromagnetic waves in inhomogeneous plasmas. *Phys. of Fluids*, 17(6):1211, 1974.

[73] V. M. Malkin, G. Shvets, and N. J. Fisch. Ultra-powerful compact amplifiers for short laser pulses. *Phys. Plasmas*, 7(5):2232, 2000.

[74] D. S. Clark and N. J. Fisch. Particle-in-cell simulations of Raman laser amplification in preformed plasmas. *Physics of Plasmas*, 10:4848–4855, Dec 2003.

[75] David C. Burnham and Raymond Y. Chiao. Coherent resonance fluorescence excited by short light pulses. *Phys. Rev.*, 188:667–675, 1969.

[76] G. L. Lamb. Propagation of ultrashort optical pulses. *Physics Letters A*, 25:181182, August 1967.

[77] E. Esarey, R. F. Hubbard, W. P. Leemans, A. Ting, and P. Sprangle. Electron injection into plasma wakefields by colliding laser pulses. *Phys. Rev. Lett.*, 79(14), Oct 1997.

[78] M. J. Everett, A. Lal, D. Gordon, K. Wharton, C. E. Clayton, W. B. Mori, and C. Joshi. Evolution of stimulated Raman into stimulated Compton scattering of laser light via wave breaking of plasma waves. *Physical Review Letters*, 74:1355–1358, feb 1995.

[79] B. I. Cohen and A. N. Kaufman. Effects of beat-wave electron trapping on stimulated Raman and Thomson scattering. *Physics of Fluids*, 21:404–412, Mar 1978.

[80] R. H. Dicke. Coherence in spontaneous radiation processes. *Physical Review*, 93:99–110, January 1954.

[81] P. Luchini and H. Motz. *Undulators and Free-Electron Lasers*. International Series of Monographs on Physics. Clarendon Press, Oxford, 1990.

[82] T.C. Marshall. *Free Electron Lasers*. MacMillan, New York, NY, 1985.

[83] R. Bonifacio, C. Maroli, and N. Piovella. Slippage and superradiance in the high-gain FEL - Linear theory. *Optics Communications*, 68:369–374, Nov 1988.

[84] R. Bonifacio, C. Pellegrini, and L. M. Narducci. Collective instabilities and high-gain regime in a free electron laser. *Optics Communications*, 50:373–378, Jul 1984.

[85] R. Bonifacio, L. de Salvo Souza, P. Pierini, and N. Piovella. The superradiant regime of a FEL: Analytical and numerical results. *Nuclear Instruments and Methods in Physics Research A*, 296:358–367, October 1990.

[86] D. A. Jaroszynski, P. Chaix, N. Piovella, D. Oepts, G. M. H. Knippels, A. F. G. van der Meer, and H. H. Weits. Superradiance in a short-pulse free-electron-laser oscillator. *Physical Review Letters*, 78, Mar 1997.

[87] R. A. Cairns. Transition between Raman and Compton regimes in laser pulse amplification. *Journal of Plasma Physics*, 76:395–401, August 2010.

[88] *Some General Properties of Nonlinear Elements-Part I. General Energy Relations*, volume 44, 1956.

[89] K. Estabrook and W. L. Kruer. Theory and simulation of one-dimensional raman backward and forward scattering. *Physics of Fluids*, 26:18921903, July 1983.

[90] V. M. Malkin, G. Shvets, and N. J. Fisch. Detuned raman amplification of short laser pulses in plasma. *Physical Review Letters*, 84:1208–1211, feb 2000.

[91] A. L. Berkhoer and V. E. Zakharov. Self excitation of waves with different polarizations in nonlinear media. *Soviet Journal of Experimental and Theoretical Physics*, 31:486, 1970.

[92] Claire Ellen Max, Jonathan Arons, and A. Bruce Langdon. Self-modulation and self-focusing of electromagnetic waves in plasmas. *Phys. Rev. Lett.*, 33(4):209–212, Jul 1974.

[93] A. A. Balakin, N. J. Fisch, G. M. Fraiman, V. M. Malkin, and Z. Toroker. Numerical modeling of quasitransient backward Raman amplification of laser pulses in moderately undercritical plasmas with multicharged ions. *PHYSICS OF PLASMAS*, 18(10), Sep 2011.

[94] John M. Dawson. Nonlinear electron oscillations in a cold plasma. *Phys. Rev.*, 113:383–387, January 1959.

[95] T. P. Coffey. Breaking of large amplitude plasma oscillations. *Physics of Fluids*, 14:1402–1406, Jul 1971.

[96] B. M. Penetrante, J. N. Bardsley, W M. Wood, C. W Siders, and M. C. Downer. Ionization-induced frequency shifts in intense femtosecond laser pulses. *J. Opt. Soc. Am. B*, 9(11):2032–2040, Nov 1992.

[97] S. C. Rae and K. Burnett. Detailed simulations of plasma-induced spectral blueshifting. *Phys. Rev. A*, 46:1084–1090, July 1992.

[98] Rachel Nuter, Stefan Skupin, and Luc Bergé. Chirp-induced dynamics of femtosecond filaments in air. *Opt. Lett.*, 30(8):917–919, Apr 2005.

[99] S. M. Wiggins, M. P. Reijnders, S. Abuazoum, K. Hart, G. H. Welsh, R. C. Issac, D. R. Jones, and D. A. Jaroszynski. Note: Femtosecond laser micromachining of straight and linearly tapered capillary discharge waveguides. *Review of Scientific Instruments*, 82(9):096104, 2011.

[100] S. M. Wiggins, M. P. Reijnders, S. Abuazoum, K. Hart, G. Vieux, G. H. Welsh, R. C. Issac, X. Yang, D. R. Jones, and D. A. Jaroszynski. Straight and linearly

tapered capillaries produced by femtosecond laser micromachining. *Journal of Plasma Physics*, 78:355–361, Aug 2012.

[101] S. Abuazoum, S. M. Wiggins, R. C. Issac, G. H. Welsh, G. Vieux, M. Ganciu, and D. A. Jaroszynski. A high voltage pulsed power supply for capillary discharge waveguide applications. *Review of Scientific Instruments*, 82(6), Jun 2011.

[102] Y. Ishida, T. Yajima, and A. Watanabe. A simple monitoring system for single subpicosecond laser pulses using an SH spatial autocorrelation method and a CCD image sensor. *Optics Communications*, 56:57–60, 1985.

[103] C. Iaconis and I. A. Walmsley. Self-referencing spectral interferometry for measuring ultrashort optical pulses. *IEEE J.Quantum Electron.*, 83(4):511–519, 1999.

[104] Rick Trebino, Kenneth W. DeLong, David N. Fittinghoff, John N. Sweetser, Marco A. Krumbugel, Bruce A. Richman, and Daniel J. Kane. Measuring ultrashort laser pulses in the time-frequency domain using frequency-resolved optical gating. *Review of Scientific Instruments*, 68(9):3277 –3295, September 1997.

[105] Ian A. Walmsley and Victor Wong. Characterization of the electric field of ultrashort optical pulses. *J. Opt. Soc. Am. B*, 13(11):2453–2463, Nov 1996.

[106] Ian A. Walmsley and Christophe Dorrer. Characterization of ultrashort electromagnetic pulses. *Adv. Opt. Photon.*, 1(2):308–437, April 2009.

[107] Kenneth W. DeLong, David N. Fittinghoff, Rick Trebino, Bern Kohler, and Kent Wilson. Pulse retrieval in frequency-resolved optical gating based on the method of generalized projections. *Opt. Lett.*, 19(24):2152–2154, Dec 1994.

[108] S. Abuazoum, S. M. Wiggins, B. Ersfeld, K. Hart, G. Vieux, X. Yang, G. H. Welsh, R. C. Issac, M. P. Reijnders, D. R. Jones, and D. A. Jaroszynski. Linearly tapered discharge capillary waveguides as a medium for a laser plasma wakefield accelerator. *Applied Physics Letters*, 100(1):014106, January 2012.

[109] M. S. Hur, R. R. Lindberg, A. E. Charman, J. S. Wurtele, and H. Suk. Electron kinetic effects on Raman backscatter in plasmas. *Phys. Rev. Lett.*, 95:115003, Sep 2005.

[110] T.-L. Wang, D. S. Clark, D. J. Strozzi, S. C. Wilks, S. F. Martins, and R. K. Kirkwood. Particle-in-cell simulations of kinetic effects in plasma-based backward Raman amplification in underdense plasmas. *Physics of Plasmas*, 17(2):023109, feb 2010.

[111] J. Farmer. *Numerical models for the simulation of Raman amplification in plasma*. PhD thesis, University of Strathclyde, 2012.

[112] Z. Toroker, V. M. Malkin, and N. J. Fisch. Seed laser chirping for enhanced backward Raman amplification in plasmas. *Physical Review Letters*, 109(8):085003, 2012.

[113] M. Sup Hur, G. Penn, J. S. Wurtele, and R. Lindberg. Slowly varying envelope kinetic simulations of pulse amplification by Raman backscattering. *Physics of Plasmas*, 11:5204–5211, Nov 2004.

[114] H. X. Vu, B. Bezzerides, and D. F. Dubois. Aspen: A fully kinetic, reduced-description particle-in-cell model for simulating parametric instabilities. *Journal of Computational Physics*, 156:12–42, Nov 1999.

[115] C. Huang, V. Decyk, S. Wang, E. S. Dodd, W. B. Ren, C. Mori, T. Katsouleas, and T. Antonsen. Quickpic: a parallelized quasi-static pic code for modeling plasma wakefield acceleration. *Jr., Proceedings of the 2001 Particle Accelerator Conference*, 5:4005, 2001.

[116] D. F. Gordon, W. B. Mori, and T. M. Antonsen. A ponderomotive guiding center particle-in-cell code for efficient modeling of laser-plasma interactions. *IEEE Transactions on Plasma Science*, 28:1135–1143, Aug 2000.

[117] G. Vieux. *Broad-band linear Raman chirped pulse amplification in plasma*. PhD thesis, University of Strathclyde, 2004.

[118] R. M. G. M. Trines, F. Fiúza, R. Bingham, R. A. Fonseca, L. O. Silva, R. A. Cairns, and P. A. Norreys. Simulations of efficient Raman amplification into the multipetawatt regime. *Nature Physics*, 7:87–92, January 2011.